INFORMATION TO USERS

This manuscript has been reproduced from the microfilm master. UMI films the text directly from the original or copy submitted. Thus, some thesis and dissertation copies are in typewriter face, while others may be from any type of computer printer.

The quality of this reproduction is dependent upon the quality of the copy submitted. Broken or indistinct print, colored or poor quality illustrations and photographs, print bleedthrough, substandard margins, and improper alignment can adversely affect reproduction.

In the unlikely event that the author did not send UMI a complete manuscript and there are missing pages, these will be noted. Also, if unauthorized copyright material had to be removed, a note will indicate the deletion.

Oversize materials (e.g., maps, drawings, charts) are reproduced by sectioning the original, beginning at the upper left-hand corner and continuing from left to right in equal sections with small overlaps.

Photographs included in the original manuscript have been reproduced xerographically in this copy. Higher quality 6" x 9" black and white photographic prints are available for any photographs or illustrations appearing in this copy for an additional charge. Contact UMI directly to order.

Bell & Howell Information and Learning
300 North Zeeb Road, Ann Arbor, MI 48106-1346 USA
800-521-0600

UMI®

Three-Dimensional Thermal Analysis of Curved Concrete Box Girder Bridges

Ahmed M. M. Ibrahim

A Thesis

in

The Department

of

Civil Engineering

Presented in Partial Fulfilment of the Requirements

for the Degree of Master of Applied Science at

Concordia University

Montreal, Quebec, Canada

September 1995

ABSTRACT

Ahmed M. M. Ibrahim

Three-Dimensional Thermal Analysis of Curved Concrete Box Girder Bridges

Bridge structures are exposed to severe environmental conditions over their lifetime as they are continuously gaining and losing heat from solar radiation, irradiation to the sky and convection to or from the surrounding atmosphere. These conditions cause large temperature variations within the structure at any instant of time. In concrete bridges, such temperature variations can result in stresses which can be as large as those caused by dead and live loads. Prediction of such temperature variations is a complex problem since the temperature varies with time, within the bridge cross-section, as well as from section to section along the bridge length. In long straight bridges with constant cross-sections, the assumption that the temperature is constant along the bridge length is valid and a two-dimensional analysis is sufficient to determine the distribution of temperature within the cross-section. However, in curved bridges, a three-dimensional analysis is necessary to predict the temperature distribution within the cross-section and along the axis of the bridge.

In the present research, a method of analysis and a computer program based on three-dimensional finite elements are presented to determine the time-dependent temperature variations and the corresponding stresses in box girder bridges of arbitrary plan and cross-section geometry for a given geographic location and meteorological conditions. A comparison is made between the results obtained from the analytical solution and temperature measurements obtained by other researchers on a straight bridge in Quebec to demonstrate the validity of the method of analysis. The program is then applied for a case study to illustrate the three-dimensional temperature distribution in curved concrete box girder bridges. Furthermore, a parametric study is performed to assess the influence of some chosen parameters on the temperature variation along the axis of such bridges.

ACKNOWLEDGMENTS

The author is indebted to Dr. M. M. El-Badry for his supervision, guidance, encouragement and constructive criticism throughout all stages of the research program. His willingness to help in every possible way is greatly appreciated.

The author is grateful to Dr. K. H. Ha whose wisdom and encouragement have motivated me to sustain the research interest.

Thanks are due to Dr. B. Massicotte of École Polytechnique for providing the temperature field measurements of the Grand-Mère bridge.

Thanks are also due to Mr. Bilal El-Ariss for his useful and supportive help throughout the current investigation.

I am also grateful for the encouragement and inspiration given by my former and present colleges: Safwat, Mohamed, Vinod, Raafat, Nader, Luciano, Khedr, and Marco.

The financial assistance provided by Concordia University Faculty Research Development Program, FRDP, by the Natural Science and Engineering Council of Canada, NSERC, and by the Department of Civil Engineering, Concordia University are gratefully acknowledged.

To

Mahmoud, Fayza, Hossam,

Fatma, and Rania

Table of Contents

List of Figures

List of Tables

List of Symbols

a	=	absorption coefficient representing the fraction of I, infiltrated inside the body
A	=	one half of the daily range of ambient air temprature
A_b	=	area of the inner surface of the box
A_b^e	=	area of the boundary surface element e inside the box
A_i	=	coefficient representing the ratio of the directional diffuse to the total diffuse radiation
B	=	daily average of air temperature
$[\overline{B}]$	=	strain displacement matrix
c	=	specific heat of the material, J/(kg.°C)
c_a	=	specific heat of the air, (716 J/kg °C)
$[C]$	=	heat capacity matrix of the system
$[C]^e$	=	element heat capacity matrix
d	=	deviation angle between the North direction and the global Y-axis
D	=	day of the year
$[D]$	=	matrix consisting of the thermal conductivity values, for isotropic material
E	=	Young's modulus of the material
$[E]$	=	matrix of material stiffness
ET	=	equation of time which is function of day of the year, D
$\{F(t)\}$	=	thermal load vector of the system
$\{F(t)\}^e$	=	element thermal load vector
$h^e(t)$	=	average value of the over-all heat transfer coefficient for a boundary surface element e inside the box at time t

I	=	total solar radiation incident upon the surface at time t, W/m^2
I_1, I_2, I_3	=	stress invarients
I_{sc}	=	solar constant, W/m^2
$[k]$	=	heat conduction matrix of the system
$[\bar{k}]$	=	system stiffness matrix
$[k]^e$	=	element conduction matrix
$[\bar{k}]^e$	=	element stiffness matrix
K_{tb}	=	beam transmittance coefficient accounting for attenuation of solar radiation by the atmosphere
K_{td}	=	diffuse transmittance coefficient
k_x, k_y, and, k_z	=	anisotropic thermal conductivities in the x, y, and z directions, respectively W/ (m.°C)
L_{loc}	=	the longitude of the location
L_{st}	=	the standard meridian for the local time zone; for example, the eastern time zone in North America has standard meridian of 75°
n_b	=	number of boundary fictitious elements
n_s	=	number of supported nodes in the system
n_i	=	number of interior conduction elements
n_x, n_y, and, n_z	=	direction cosines of the unit outward normal to the boundary surface
$[N]$	=	interpolation shape functions, chosen so that $T(x, y, z, t)^e$ is contnous between the elements
OWR	=	overhang length - web depth ratio
q	=	boundary heat input or loss per unit area, W/m^2
$\{\bar{q}\}^e$	=	vector of nodal displacement of the element
Q	=	rate of heat generated within the body per unit volume, W/m^3
$\{\bar{R}\}$	=	vector of thermal nodal forces of the system
$\{\bar{R}\}^e$	=	vector of thermal nodal forces

t_{sr}	=	solar time at sunrise
t_{ss}	=	solar time at sunset
T	=	temperature of the body, at any point in the space (x,y,z) at any time t, °C
$\{T\}^e$	=	vector of nodal temperatures for element e
$T_a(t)$	=	air temperature at time t
T_b	=	air temperature inside the box
T_s	=	temperature of the inside surface of the box at time t
$T_s^e(t)$	=	average value of the surface temperature for a boundary surface element e inside the box at time t
$\{T(t)\}$	=	nodal temperature vector of the system
$\{U\}$	=	vector of nodal displacements of the system
V_b	=	volume of the air inside the box
α	=	the coefficient of thermal expansion
β	=	slope of the surface to the horizontal, i.e., the angle between the plane of the surface in question and the horizontal; $0 \le \beta \le 180°$, with $\beta > 90°$ for surfaces which has a downward facing component
γ	=	surface azimuth angle, that is, the angle between the projection of the normal to the surface on a horizontal plane and the local meridian, with zero due south, east negative and west positive $(-180° \le \gamma \le 180°)$
δ	=	solar declination, that is, the angular position of the sun with respect to the plane of equator ($-23.45° \le \delta \le 23.45°$)
$\{\varepsilon\}$	=	vector of mechanical strains exhibited by the body
$\{\varepsilon_o\}$	=	vector of initial strains
θ	=	incidence angle of sun rays
ν	=	Poisson's ratio

ρ	=	density of the material, kg/m^3
ρ_a	=	density of the air (1.228 kg/m^3)
$\{\sigma\}$	=	vector of total stresses induced in the body
$\{\sigma_\circ\}$	=	vector of initial stresses
$\sigma_1,\sigma_2,\sigma_3$	=	principal stresses
φ	=	latitude of the location, north positive ($-90° \le \varphi \le 90°$).
ψ	=	angle of rotation along the bridge length
ω	=	hour angle, which is the angular displacement of the sun east or west of the local meridian due to the rotation of the earth on its axis at 15° per hour, with solar noon being zero, morning negative, afternoon positive

CHAPTER 1
INTRODUCTION

1.1 General

Any structure exposed to the atmosphere is subjected to an exchange of heat energy between the surfaces of the structure and the surrounding environment. The interaction between the surface of the structure and the climatological environment results in temperature differences between the elements of the structure. These temperature differences, in turn, produce strains and deformations in the structure. These deformations, if restrained, can result in pronounced stresses. The resulting stresses, if not considered in the design, may lead to cracking of concrete and further degradation of the structure.

In bridge structures, stresses due to temperature are of particular importance since bridges are continuously gaining or losing heat from the surrounding environment. Notable cracks have occurred in bridge structures and have seriously affected the serviceability and integrity of the structure. Leonardt et al. (1965), Zichner (1981), and Massicotte et al. (1994), reported such cracks in some major bridges and attributed these cracks to the fact that environmental thermal loading was inaccurately modelled or completely ignored in the design of these bridges. Figures 1.1 and 1.2 show two examples of these cracks.

Codes and specifications, nowadays, recognize the importance of this type of thermal loading. Most codes mandate the designer to include this type of loading in the analysis of bridge structures.

During the past three decades, many investigators have attempted to provide a comprehensive understanding of thermal loading and its effects on the behavior of bridge

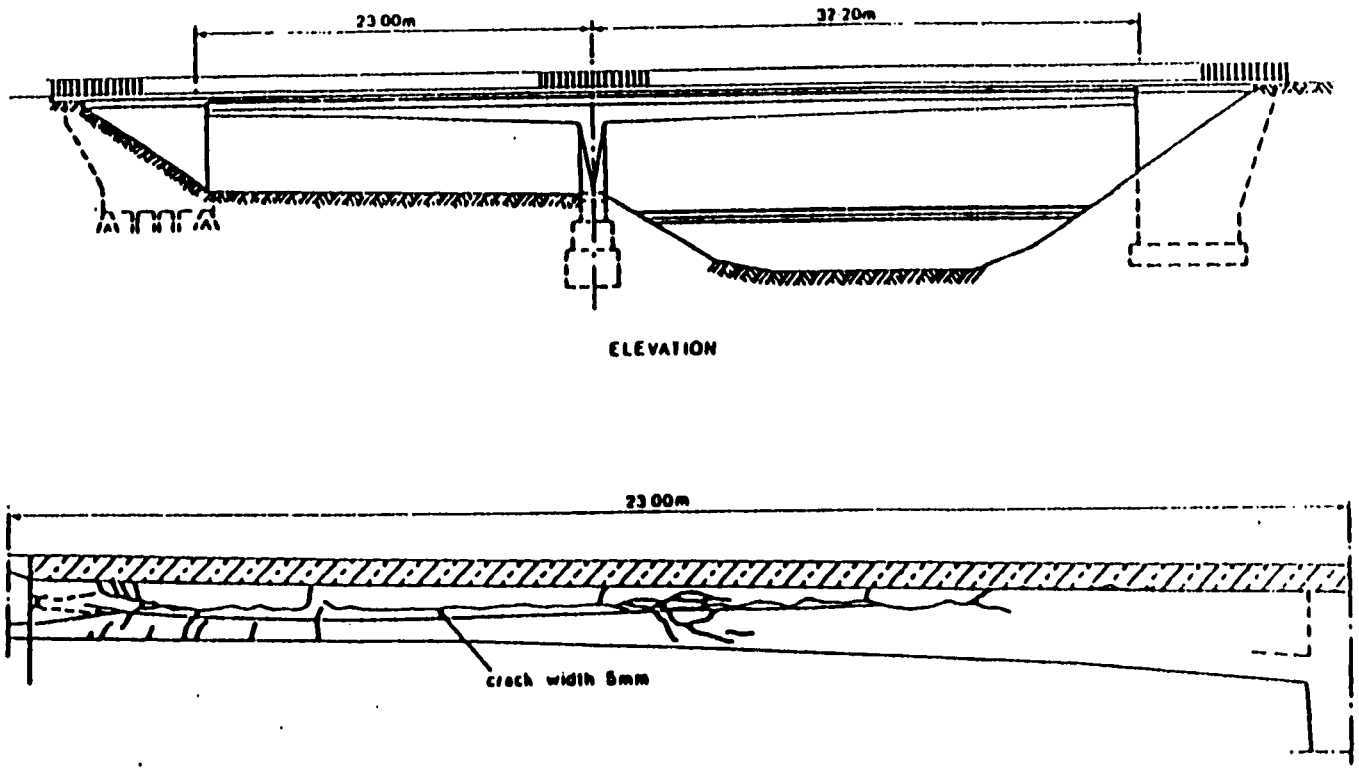

Figure 1.1 Cracks reported in The Jagst Bridge by Leonhardt et al. (1965)

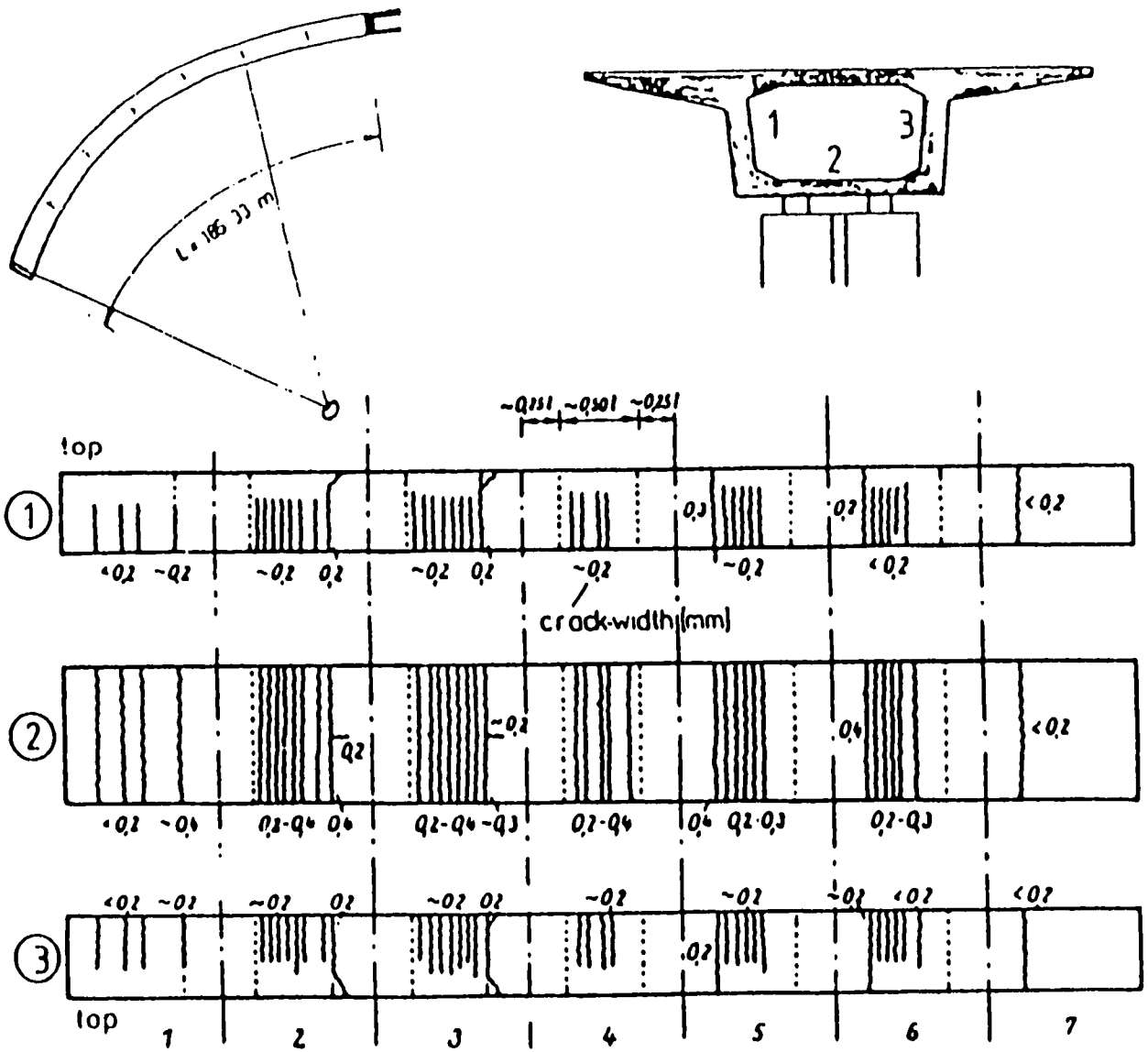

Figure 1.2 Cracks reported in a multispan box girder bridge by Zichner (1981)

structures. They either proposed simplified methods of analysis or developed numerical techniques to predict the temporal effect of thermal loading conditions on such structures.

Several attempts have been made to address the problem in a simplified form. Many researchers have studied the effects of temperature variations at the cross-section level of the bridge, and some have even considered only the temperature variation along the depth of the cross-section. These simplifications can be true in the case of straight bridges with constant cross-sections and material properties since there can be no temperature difference between one section and another along the length of the bridge as the solar radiation intensity, which is the prime source of heat energy to the bridge, does not change along the bridge length. However, in curved bridges, the temperature varies within the cross-section and may also vary along the longitudinal axis of the bridge due to the variation of the incidence angle of the sun rays on the bridge side as the bridge changes direction along its length (see Figure 1.3). Therefore, for this latter case, full modelling of the bridge geometry is deemed necessary in order to predict the thermal response.

1.2 Objectives and Scope

In the present research, a four span, curved concrete box girder bridge is analyzed under environmental thermal conditions in order to examine the importance of temperature variations along the bridge length. The main objectives of this research are to:

1. Present a numerical technique that can fully model bridge structures of arbitrary geometry in order to predict the thermal response (temperature and induced stresses) due to surrounding meteorological conditions.
2. Illustrate the three-dimensional temperature variations that may develop in curved concrete bridges and to assess the influence of certain parameters on these variations.

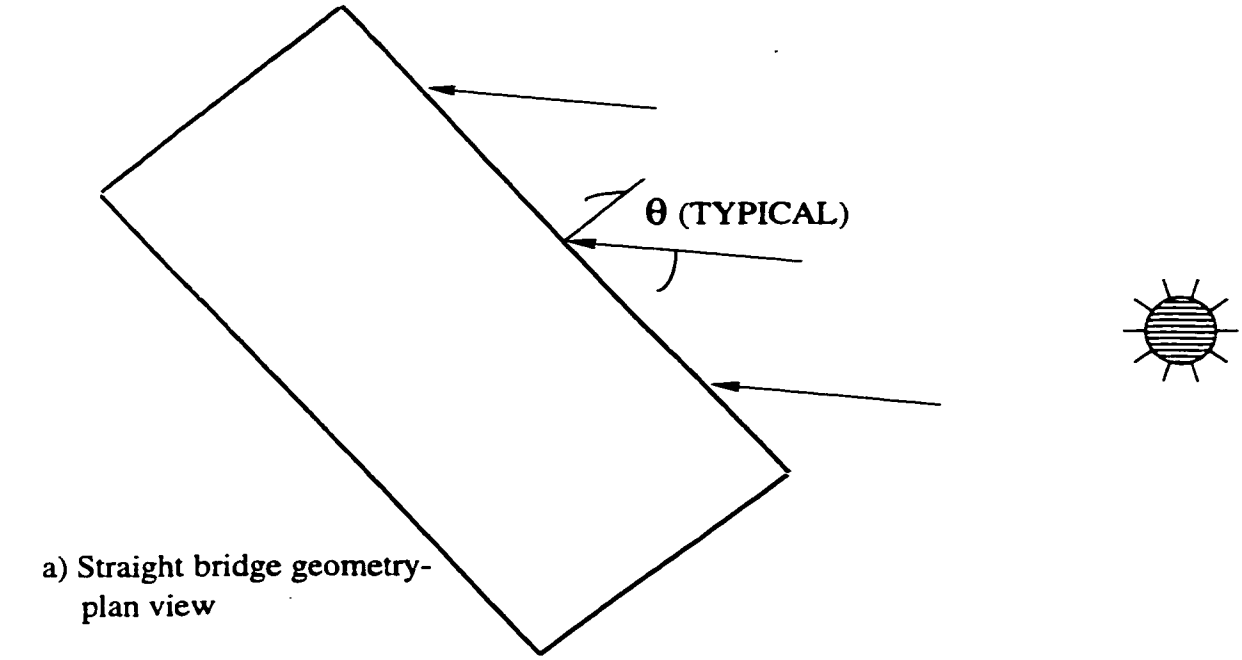

a) Straight bridge geometry-
plan view

θ : Incidence angle; the angle between the sun rays and the normal to the surface.
(see Chapter 4 for more details)

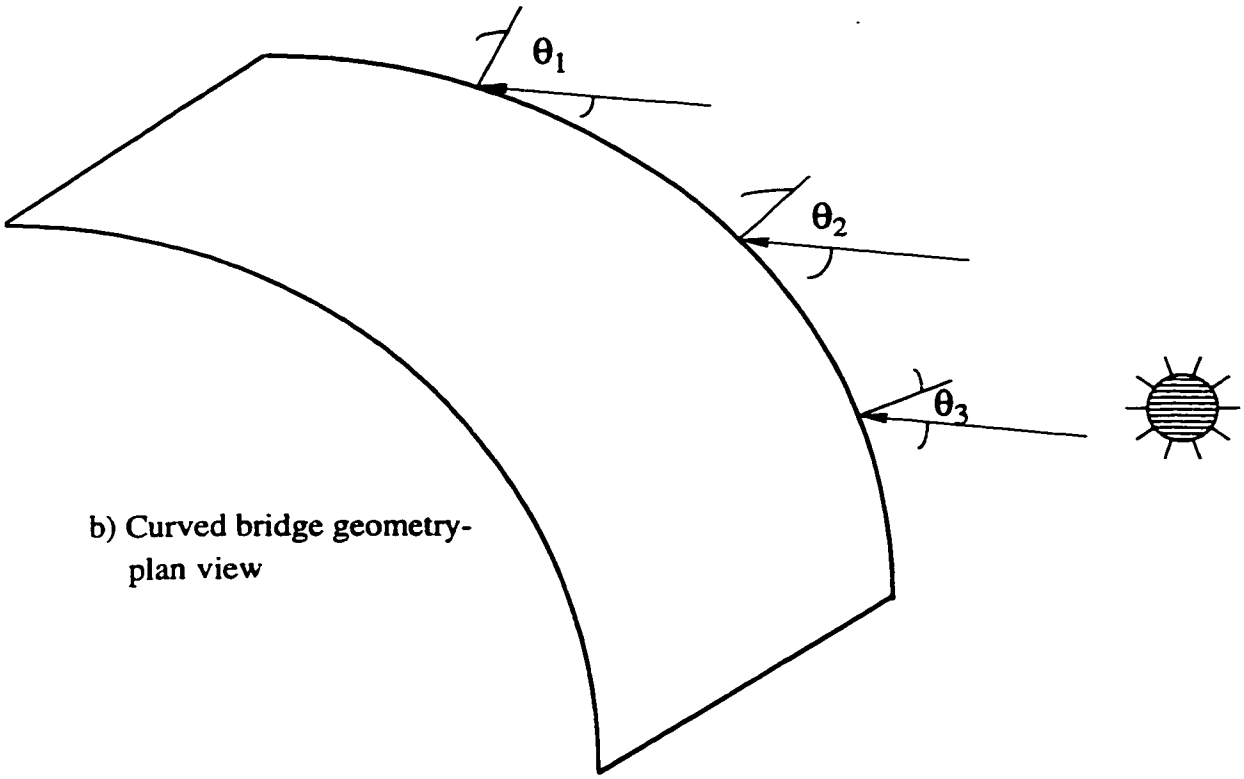

b) Curved bridge geometry-
plan view

Figure 1.3 Comparison between solar radiation intensity recieved by the surfaces of both curved and straight bridges.

In the following chapter, the physical phenomenon of heat exchange is discussed, and a brief review of the previous analytical work on the subject is presented. The method of analysis to calculate the temperature and stress distributions within a bridge structure is described in Chapter Three. The computer implementation of this method as well as verification problems are presented in Chapter Four. Application of the developed numerical technique is performed on a curved concrete box girder bridge. A case study is conducted to demonstrate the three-dimensional temperature variations that can develop in this type of bridge. A parametric study is also conducted to examine the effects of certain parameters on this variation. The analysis and the results of these studies are presented in Chapter Five. Finally, a summary of the investigations, the conclusions reached, and recommendations for future research are given in Chapter Six.

The effect of heat of hydration of cement and long-term phenomena of creep and shrinkage are not considered in this research. Only short-term effects caused by daily heating and cooling cycles are investigated.

CHAPTER 2
LITERATURE REVIEW

2.1 General

The interest in studying the behavior of bridge structures under thermal environmental loading has increased significantly in recent years. Prediction of temperature and stress distributions within a bridge structure for design considerations has been the focus of many investigators.

Early investigations in this field attempted to correlate the temperature range within the structure to the surrounding weather data. Prediction of the temperature field from the actual environmental conditions was a later step. Different approaches were used to predict this temperature field. For structures with simple geometry, classical methods of analysis were utilized. However, for structures with complex geometry, numerical techniques based on either finite element or finite difference were adopted.

In the following, a brief discussion of the heat transfer mechanism that occurs between the structure and the atmosphere is presented along with a review of the theoretical and experimental research previously done. The types of thermally induced stresses in the structure are also discussed.

2.2 Heat Transfer Mechanism and Bridge Temperature

2.2.1 Sources of Heat

Exposed concrete bridge structures continuously lose and gain heat through three principal mechanisms of heat transfer: radiation from the sun, convection of heat between the surface and the ambient air, and re-radiation of the surface to, or from, the surrounding environment.

The intensity of solar radiation reaching the surface of a bridge superstructure varies during the day, and from one day to another during the year. This diurnal and seasonal variation of solar radiation is dependant on several factors as will be discussed later in Chapter 4. The solar radiation reaches the surface of the bridge primarily through direct beam radiation, diffusive radiation from the sky, and reflected radiation from the surrounding objects. The incoming radiation reaching the surface may be reflected back or may penetrate the surface, be absorbed, and converted to heat. The amount of absorbed energy depends upon the nature and color of the receiving surface. A dark and rough surface has a higher absorptivity than does a light and smooth surface. Some of this absorbed energy is lost to the air by convection and re-radiation. Convective heat transfer is a function of wind speed and the temperature difference between the surface and the surrounding air. Figure 2.1 shows, schematically, the heat flow process described above.

2.2.2 Temperature Gradient and Previous Research

In daytime, especially in summer, a net gain of energy occurs, resulting in a rise of temperature throughout the structure such that the top surface becomes warmer than the soffit. Because of the poor thermal conductivity of concrete, this rise in temperature results in temperature gradients within the bridge superstructure. These gradients are denoted as positive gradients. Conversely, net loss of heat, which occurs typically during winter nights, results in a reduction of temperature in the structure, thereby creating negative gradients of temperature with warmer soffit than the top.

When temperature gradients develop, they result in rotational distortions which, when restrained, produce stresses in the structure. These gradients must be determined if the stresses need to be calculated. The temperature gradients are governed by the heat flow through the body and are functions of the density, specific heat, and thermal conductivity

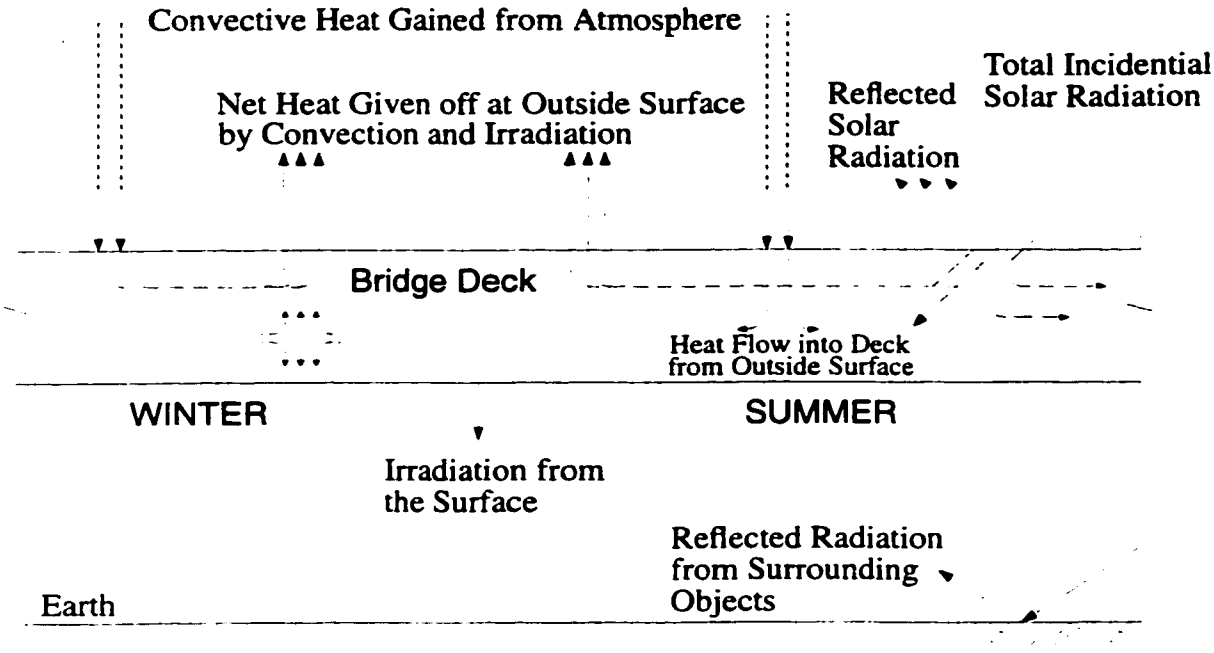

Figure 2.1 Mechanism of heat transfer for a typical bridge deck.

of the material. The differential equation that governs the transient heat flow within a body is given as [Incropera and DeWitt (1985)]:

$$\frac{\partial}{\partial x}(k_x\frac{\partial T}{\partial x}) + \frac{\partial}{\partial y}(k_y\frac{\partial T}{\partial y}) + \frac{\partial}{\partial z}(k_z\frac{\partial T}{\partial z}) + Q = \rho c\frac{\partial T}{\partial t} \tag{2.1}$$

where

T = temperature of the body, at any point in the space (x,y,z) at any time t, °C,

k_x, k_y, and k_z = anisotropic thermal conductivities in the x, y, and z directions, respectively, W/(m.°C),

Q = rate of heat generated within the body per unit volume, W/m^3,

ρ = density of the material, kg/m^3,

c = specific heat of the material, J/(kg.°C).

The boundary conditions associated with the heat flow equation, can be expressed in the following form:

$$k_x\frac{\partial T}{\partial x}n_x + k_y\frac{\partial T}{\partial y}n_y + k_z\frac{\partial T}{\partial z}n_z + q = 0 \tag{2.2}$$

where n_x, n_y, and n_z = direction cosines of the unit outward normal to the boundary surface,

and q = boundary heat input or loss per unit area, W/m^2.

The boundary heat input or loss for structures exposed to environmental conditions is the sum of the three basic components of heat transfer mechanism described earlier: solar radiation $q_s(s,t)$, convection $q_c(s,t)$, and irradiation $q_r(s,t)$. This sum varies with time t and the position considered on the boundary surface s, and is given by:

$$q = q_s(s,t) + q_c(s,t) + q_r(s,t) \tag{2.3}$$

Various researchers have used Equation (2.1) to investigate the temperature distribution within bridge structures. In general, they have reduced the differential equation from its general three dimensional form to either one-or two-dimensional heat flow equations. One-dimensional heat flow leads to a vertical temperature distribution in the cross-section of the bridge superstructure, while two-dimensional heat flow includes also the transverse temperature distribution in the cross-section of the bridge.

Extensive literature review was carried out by Imbesn et al. (1985) and El-Alam and Massicotte (1994) on the thermal effect on bridge superstructures; following is a brief summery of their review in addition to the up-to-date research conducted on the subject.

Tests conducted in 1955 by Narouka, Hirai, and Yamaguti on a composite steel bridge resulted in the determination of a nonlinear distribution of temperature through the depth of the bridge cross-section. The maximum measured temperature gradient was found to be 16 ^{o}F.

Barber, in 1957, presented a formula capable of estimating the maximum temperature of the pavement surface of the bridge. This formula incorporated the air temperature, wind speed, surface temperature, intensity of solar radiation, and the pavement thermal properties.

Zuk (1965) attempted to estimate the maximum surface temperature of a bridge located in Virginia area using a modified version of the equation developed by Barber (1957). He also presented an equation to determine the maximum differential temperature between the top and bottom surfaces of a composite steel bridge. Field tests showed good correlation between measured values and the proposed equation.

Priestley, in 1972, analyzed the effect of different available suggested thermal gradients and compared the results with available measured data. One of these suggested gradients is the one proposed by Maher (1970). Maher suggested a linear temperature distribution through the top slab of the bridge deck. This assumption was based on different measurements taken from three bridges in Britain. Another suggested thermal gradient studied by Priestley is the one proposed by the Ministry of Works of New Zealand in which the temperature varies with depth as second, fourth, and sixth-degree parabolas. Based on this study, Priestley found the sixth degree parabola to be the most accurate distribution in agreement with the measured data, and thus was recommended for superstructure depths between 1200 and 1500 mm (see Figure 2.2).

Emerson (1973) used the finite difference method to analyze one-dimensional heat flow within a concrete bridge deck from data related to solar radiation, ambient air temperature, and wind speed. The temperature predicted by this method correlated well with measured prototype temperature distributions.

Lanigan (1973) developed a two-dimensional finite element program to find temperature distribution through bridge-type structures. The results obtained from the program showed good agreement with measurements done on laboratory models.

Reynolds and Emanuel (1974) reported their study of the different parameters that influence the estimation of differential temperature between the outer and inner surfaces of the bridge structure. They also reported the results of different theoretical studies and measurements carried out on the thermal response of bridges.

Radolli and Green (1975) used one-dimensional finite difference method to predict temperature distribution in concrete slab bridges and "I" girders. Predicted temperature

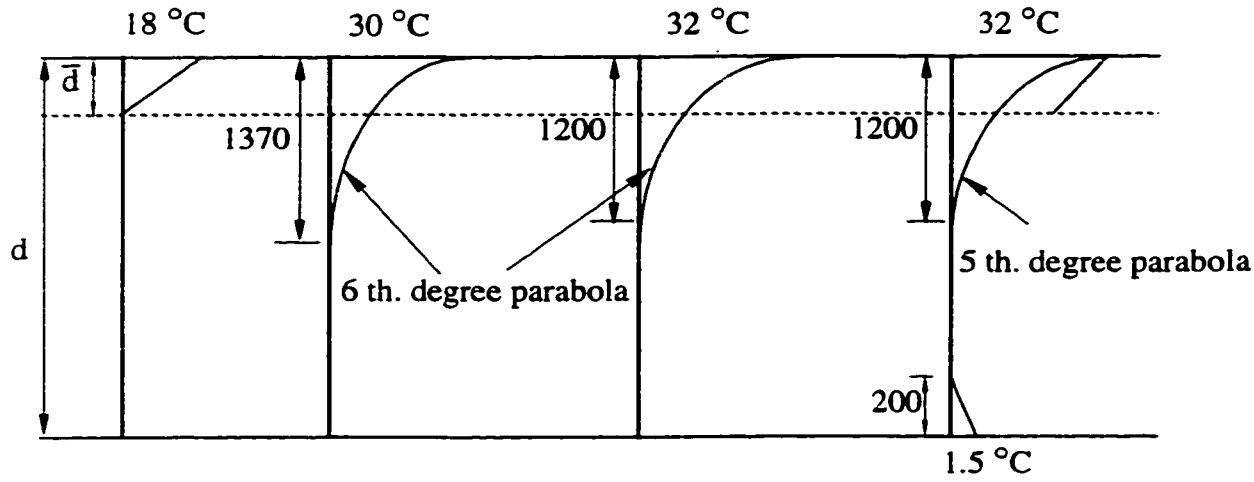

Figure 2.2 Box girder temperature gradients studied or suggested by Priestley.

gradient and observed measurements were in good agreement. They proposed simplified formulas to predict temperature gradients for use in design.

Hunt and Cooke (1975) developed a semi-analytical method to predict the temperature distributions in bridge decks. They assumed that the horizontal temperature distribution can be ignored in such type of structures. Comparison of the developed method with experimental measurements done by Priestly (1972) on prestressed concrete box girder bridge showed good agreement.

In 1976, Priestley studied the problem of the form of the thermal gradients and the induced stresses in the structure. Based on his observation and an investigation in New Zealand, he proposed a revised temperature gradient to that suggested in 1972. It consisted of three individual parts. In the first part, temperatures were assumed to decrease nonlinearly from a maximum at the top surface of the deck slab to a minimum at a depth of 1200 mm, with the nonlinear variation represented by a fifth-degree parabola. The second part applied only to a top slab of a box girder, in which temperatures were assumed to decrease linearly. The third part assumed a linear variation of temperatures over the bottom 200 mm of the cross-section (see Figure 2.2).

Emerson (1979) reported the results of a study developed in the "British Transport and Road Research Laboratory" using a one-dimensional heat flow to investigate the influence of different parameters on the temperature distributions within bridge structures. She concluded that the resulting temperature within the body depends on the absorptivity and the emissivity of the surface receiving the heat flux. The wind speed is another important parameter that can affect the convection mode of heat exchange. Large wind speed reduces temperature of the bridge surface.

Dilger, et al. (1983) examined the thermal effects on a composite box girder bridge structure using the one-dimensional finite difference method. They discussed the different environmental parameters that affect the temperature distribution, including the shade length caused by the overhanging top slab and the air enclosed in the box girder. Extreme temperature gradients were found to exist under winter and spring conditions.

Elbadry and Ghali (1983a) utilized the two dimensional finite element method to predict the thermal distribution over the cross-section of a box girder bridge structure due to environmental conditions including solar radiation, wind speed, ambient air temperature, and geographic locations. They developed a computer program *FETAB*: Finite Element Thermal Analysis of Bridges [Elbadry and Ghali (1982)]. *FETAB* can model any cross-section of arbitrary shape or arrangement of material. The program simulates the cross-section as an assembly of constant heat flow triangular and/or bilinear quadrilateral heat conduction elements. One-dimensional fictitious linear boundary elements are used to simulate the environmental boundary conditions. They employed the program in a parametric study to examine the effect of orientation of bridge axis, air temperature extremes, wind speed, surface cover and cross-section shape and depth. They concluded that the most critical temperature field develops under summer conditions, when the daily range of ambient air temperature is large, wind speed is minimum, and the deck is covered with asphalt wearing surface.

Imbsen, et al. (1985) investigated the effect of different temperature gradients on a variety of actual bridge cross-sections. Their research included a summary of the different available thermal gradients in present bridge design codes, and they also recommended four different temperature distributions for different zones in the United States.

Hirst and Dilger (1989) modified the program *FETAB* [Elbadry and Ghali (1982)] to include meteorological data measured at weather stations, namely, the hourly variation of solar radiation incident upon a horizontal surface. Temperature distributions obtained from the modified program are compared to field measurements taken for three bridges located in Canada and Australia. The comparison showed good correlation between the program and the measurements.

Clark (1989) examined the frequency occurrence of thermal gradients in a box girder bridge during a period of 50 years. He showed that the critical temperature distribution was related to the minimum and maximum values of the ambient air temperature.

Mirambell and Aguado (1990) have analyzed the influence of several geometrical parameters on the thermal response of a concrete box girder bridges, using two dimensional finite difference method. The parameters considered included the top slab thickness - web thickness ratio, the overhanging length - web depth ratio, the variation of the cross-section depth over the bridge length, and the presence of haunched top and bottom slabs. Thermal response of multicellular concrete box girder bridges was also investigated. They found that the depth of the superstructure as well as the ratio between the deck's upper and bottom slab width are the parameters which have the greatest influence on the thermal response and stress distribution.

Waldron, Ramezankhani, and Woodman (1990) modified the computer program, developed by Elbadry and Ghali (1982), to account for the climatic parameters observed from field measurement or recorded at local metrological station to establish the time-varying boundary conditions. Comparison of the temperature distribution calculated from the program with field data collected over a one year period for the Cogan Spur Viaduct located in South Wales, England showed good agreement.

Fu, Ng, and Cheung (1990) presented analytical results obtained from a parametric study conducted on three types of composite bridge structures subjected to environmental conditions. The computer program ADINA-T was used for the purpose of the study. The effects of convection coefficient, slab overhang-to-slab depth ratio, and diurnal ambient air temperature were considered. They found the slab overhang-to-depth ratio to be the most influential variable on the temperature distribution within the bridge deck.

Branco and Mendes (1993) adopted a numerical technique based on the two-dimensional finite element method to accurately predict the nonlinear temperature distribution for different types of concrete bridges. They compared the predicted temperature distribution with the different design-code provisions for the thermal loading available in Southwest Europe.

Molesini and Massicotte (1993) studied the thermal behavior of the Grand-Mere bridge located in Quebec, Canada, which experienced severe deflection combined with localized cracking. They modified the program *FETAB*, [FETAB-2], to include in the input file the measured maximum and minimum environmental air temperature, average wind speed, average sky opacity, and snow presence for every day of the analysis over a three-year period. They concluded that four different thermal gradients can occur in the bridge cross-section, two of them result in thermal stresses that can cause cracks and further degradation of the structure. El-Alam and Massicotte (1994) used FETAB-2 to estimate the frequency occurrence of the critical thermal gradient that may develop over a period of 50 year for the aforementioned bridge.

Saetta, Scatta, and Vitaliani (1995) presented a numerical procedure based on the finite element method to perform thermal analysis of concrete structures. They modeled the environmental boundary conditions as an equivalent convective exchange between the

surface of the body and the surrounding. A suitable fictitious temperature is added to the ambient air temperature to consider the effect of heat from the sun. Comparison of temperature gradients obtained using this boundary modelling with experimental measurement for a box girder bridge showed good agreement.

To the author's knowledge, no study has been conducted on curved bridges to investigate the temperature distribution developed in such bridges. Moreover, all previous research, either experimental or analytical, was limited to prediction of temperature distributions within the cross-section level. No full modelling has been yet considered to investigate the temperature variations that may develop along the length of bridge structures.

2.3 Thermally Induced Stresses

As stated by Leonhardt (1977), "Temperature plays a much more important role in causing stresses than most engineers are aware of". Several researchers have shown that these stresses can be of the same order of magnitude as those produced by dead and live loads. Many investigations have indicated thermal stresses in concrete bridges of magnitude higher than the concrete modulus of rupture and, hence, occurrence of cracking. Such cracking can seriously affect the serviceability and durability of these structures.

In the following section, a brief discussion of the types of thermal stresses in bridge structures is presented, and a reference is made to the available methods of analysis.

2.3.1 Types of Thermal Stresses:

A statically determinate structure subjected to uniform or linear temperature variation over the cross-section undergoes free longitudinal movement without developing

any stresses. However, if the temperature variation is nonlinear, thermal stresses will be induced in the cross-section of the structure. These stresses are referred to as "self-equilibrating stresses" or "eigenstresses". In statically indeterminate structures, the deformations due to temperature are restrained at the support. This restraint causes a change in reactions, in internal forces, and, hence, in stresses. Such stresses are known as "continuity stresses" and are produced whether the temperature distribution over the cross-section is linear or nonlinear. Both the self-equilibrating and continuity stresses are produced in the longitudinal direction and are therefore referred to as longitudinal stresses.

In structures with closed cross-sections such as box girder bridges, stresses due to temperature can also be induced in the transverse direction. Such stresses can be as important as those produced in the longitudinal directions.

2.3.1.1 Longitudinal Stresses:

a) Self-equilibrating Stresses:

When temperature varies over the cross-section of a bridge superstructure, the fibers of the cross-section attempt to undergo free strain equal to αT. If the temperature variation is linear, the free strain will be linear and no stresses will be produced in the cross-section. However, in case of nonlinear variation, the strained fibers of the cross-section will no longer lie in one plane. This contradicts the Navier-Bernoulli hypothesis that plane sections will remain plane after deformation, and thus, longitudinal stresses have to develop in the cross-section to restore the deformed shape to its planery position (see Figure 2.3).

It is clear that the existence of this type of stress depends on the shape of the temperature distribution over the cross-section, regardless of the support conditions. In statically

determinate structures, these self-equilibrating stresses produce no internal forces since the stress resultant will be equal to zero.

Self-equilibrating stresses can be calculated by conventional techniques based, for example, on the displacement method of analysis. Such techniques have been used by several researchers including Priestly (1972), Elbadry and Ghali (1983a), Clark (1989), Mirambell and Aguado (1990), and Branco and Mendes (1993). Details of the displacement method for thermal stress analysis can be found in Ghali and Neville (1989).

b) Continuity Stresses:

When a bridge has more than one span, the temperature change over the cross-section results in statically indeterminate reactions and internal forces. These forces, in turn, produce continuity stresses as the deformations resulting from the temperature change are restrained by the intermediate supports (see Figure 2.4). These continuity stresses must be added to the self-equilibrating stresses to give the total longitudinal stresses at any cross-section.

The elastic analysis needed to determine the continuity stresses can be performed using any of the classical methods of structural analysis. The force method, for example, showed great simplicity of implementation on bridge structures of low indeterminacy in finding the continuity stresses at any section. It has been widely used by many researchers, e.g. Maher (1970), Priestley (1972), Radolli and Green (1975), Elbadry and Ghali (1983a), Molesini and Massicotte (1993) and many others.

Another classical method used to find these stresses is the stiffness method, which is more suitable for structures having a high degree of indeterminacy such as multi-span bridges. Details of this method can be found in several texts [e.g. Ghali and Neville (1989)].

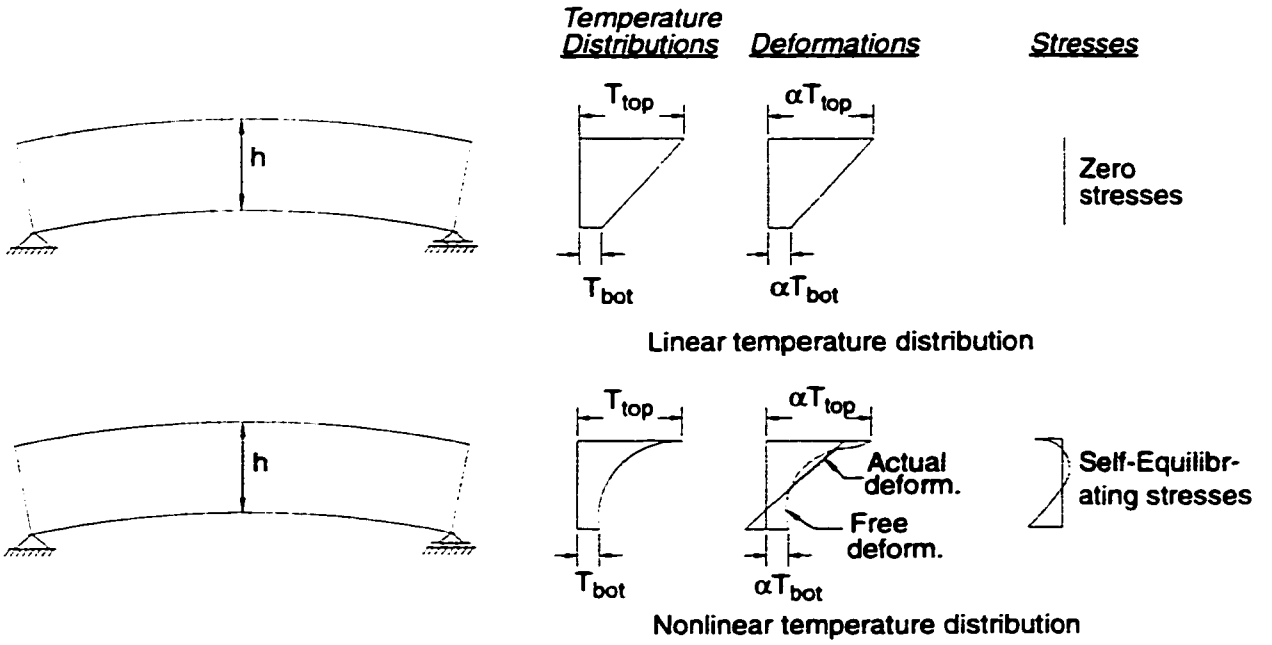

Figure 2.3 Self-Equilibrating Stresses induced in a simply supported beam due to nonlinear temperature distribution.

a) Moments and reactions in a released structure due to temperature gradient.

b) Induced continuity moments.

Figure 2.4 Continuity moments due to temperature gradients in a statically indeterminate beam.

2.3.1.2 Transverse Stresses

In box girder bridges, the expansion or contraction of the top slab in the transverse direction due to vertical temperature variation over the cross-section is different from that of the bottom slab. This variation in the transverse deformation induces transverse stresses in the cross-section. These transversal stresses can be of significant magnitude. Priestley (1976) reported that transverse tensile stresses of 3.5 MPa may occur at the bottom of the top slab of the bridge cross-section. The horizontal variation of temperature across the web of the cross-section produces similar effects to the one described above. Figure 2.5 shows the deflected shape of the bridge cross-section due to these temperature variations.

Transverse stresses due to temperature can be analyzed simply by considering a closed plane frame made up of a strip of unit width between two cross-sections. Performing the analysis of indeterminate frame subjected to thermal loading by any conventional method (e.g. the displacement method), yields the internal forces developed in the frame, and, hence, the stresses induced. The detailed procedure of the simplified method mentioned above can be found in Elbadry and Ghali (1983b).

The method described above deals with temperatures which vary only over the cross-section while remaining constant along the axis of the bridge. However, to consider the effect of temperature change along the axis of the bridge (as in the case of a curved bridge) each individual cross-section needs to be analyzed to give the induced transverse stresses.

Applying the previous method to determine the transverse effect implies that both the stresses in the transverse and longitudinal directions are independent of each other (uncoupled). This assumption leads to computed thermal stresses somewhat less than the actual stresses.

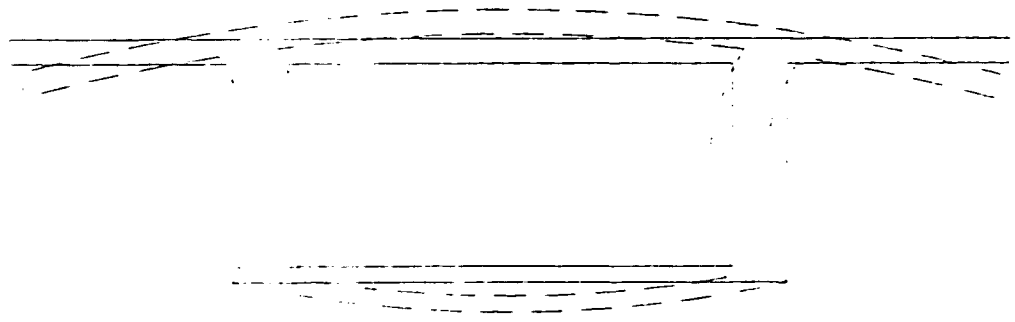

Figure 2.5 Deflected shape of the bridge cross-section due to temperature gradients in the vertical and horizontal directions.

In curved box girder bridges, the analysis for stresses due to temperature can be more complex than in the case of straight bridges. This is because the temperature may vary from one cross-section to another as well as within each cross-section in both the vertical and horizontal directions. The induced self-equilibrating stresses may be different from section to section and the continuity stresses in both the longitudinal and transverse directions may be coupled. Therefore, a three-dimensional analysis may be required. In the present research, a three-dimensional finite element stress analysis will be adopted for this purpose and will be described in the following chapter.

CHAPTER 3

PREDICTION OF TEMPERATURE AND STRESS VARIATION USING THE FINITE ELEMENT METHOD

3.1 General

A general body of arbitrary geometry exposed to the meteorological conditions is subjected to temperature variation at various points within the body itself and also from time to time. The temperature variation should be accurately predicted if the resulting stresses induced in the body are required for the purpose of design. A closed form solution to this problem is not easy to obtain. It depends on the complexity of the configuration of the body as well as the variation with time of the boundary conditions along the surface of the body. For a box girder bridge, the closed form solution cannot be formulated due to the aforementioned reasons. Thus, employing a numerical technique to predict the thermal behavior of this type of structure would provide the best approach. Among the different available numerical techniques, two methods, namely, the finite difference and the finite element methods, have given accurate prediction of thermal response of bridge structures as compared to experimental results. The finite difference method has been used successfully by many researchers [Dilger et al. (1983), Mirambell and Aguado (1990)]. However, the method is "rather cumbersome when it deals with regions having curved or irregular boundaries" [Segerlind (1984)]. In the present research, the finite element method is preferred as it can handle most structures with relative ease, regardless of the boundary configuration.

In this chapter, the formulation of the finite element method used to solve the heat flow equation with time is presented. The calculation of thermal stresses developed in the body due to boundary restraints and nonlinear temperature distributions is also shown.

3.2 Finite Element Formulation for Prediction of Temperature Distribution

The governing differential equation for heat flow presented in Chapter 2, Equation (2.1), can be reduced for the special case of isotropic, homogeneous, and temperature-independent material to the following form:

$$k\left(\frac{\partial^2 T}{\partial x^2}+\frac{\partial^2 T}{\partial y^2}+\frac{\partial^2 T}{\partial z^2}\right)+Q = \rho c\frac{\partial T}{\partial t} \tag{3.1}$$

with the associated boundary conditions of:

$$k\left(\frac{\partial T}{\partial x}n_x+\frac{\partial T}{\partial y}n_y+\frac{\partial T}{\partial z}n_z\right)+q = 0 \tag{3.2}$$

with the same notation as described in Subsection 2.2.2.

3.2.1 Boundary Conditions

As discussed in Subsection 2.2.2, the boundary heat input or loss, q, is the sum of three components: solar radiation, convection and irradiation.

a) Solar Radiation: The heat gain due to solar radiation received by an exposed surface can be expressed as:

$$q_s = aI \tag{3.3}$$

where I = total solar radiation incident normal to the surface at time t. Its value can be obtained from meteorological data, taken from published tables, or calculated from mathematical expressions as will be discussed later in Subsection 4.3.1

a = absorption coefficient representing the fraction of I that infiltrates into the body.

b) Convection: The heat lost to, or gained from, the surrounding air due to convection as a result of difference between the surface and air temperatures is given by Newton's law of cooling as:

$$q_c = h_c (T_s - T_a) \tag{3.4}$$

in which T_s and T_a are the surface and air temperatures, respectively, at any time t, °C; h_c is a convection heat transfer coefficient, W/(m^2 °C), which is a function of wind speed, surface roughness, and the geometric configuration of the structure. Its values can be determined experimentally or from empirical equations.

c) Thermal Irradiation: The amount of irradiation lost from the bridge surface to the surrounding air is given by Zichner (1981) as:

$$q_r = \sigma_s e \left[(T + T^*)^4 - e_{at} (T_a + T^*)^4 \right] \tag{3.5}$$

in which σ_s is the Stefan-Boltzman constant = 5.677 x 10^{-8} W/(m^2 °K^4); e is the emissivity coefficient relating the radiation of the bridge surface to that of an ideal black body; T^* is a constant = 273.15 used to convert the temperature from degrees Celsius (°C), to degree Kelvin (°K); and e_{at} is the emission factor of the atmosphere which can be estimated in terms of air temperature as [Sherwood and Ray (1969)]:

$$e_{at} = 1 - 0.261 exp\,(-7.77 \times 10^{-4})\, T_a^2 \tag{3.6}$$

Equation (3.6) can be rewritten in a form similar to equation (3.4) in order to obtain a quasi-linear relation in terms of temperature T; thus:

$$q_r = h_r (T_s - T_a) \tag{3.7}$$

where h_r is defined as an irradiation heat transfer coefficient.

Molesini and Massicotte (1993) have shown that h_r can be approximated by:

$$h_r = \sigma_s e \left[(T+T^*)^2 + \sqrt{e_{at}} (T_a+T^*)^2 \right] (T+2T^*+T_a) \tag{3.8}$$

Thus, the effects of convection and irradiation between the surface and the air can be combined by using an overall heat transfer coefficient, h, defined as the sum of the convection coefficient, h_c, and the irradiation coefficient, h_r. It should be noted that h_r and, hence, h, are functions of both the time t and the position s considered on the boundary surfaces. Thus:

$$h(s,t) = h_c + h_r(s,t) \tag{3.9}$$

3.2.2 Finite Elements Discretization

In order to solve the previous differential equations to obtain the temperature values, the general body shown in Figure 3.1 can be subdivided (discretized) into a finite number of elements. In the formulation developed herein, two types of elements are used to idealize the structure: a 20-node isoparametric solid element and an 8-node fictitious surface element. The 20-node solid element is used to model the interior conduction within the body. It has been preferred to the 8-node brick element because it provides more accuracy due to its quadratic shape functions, as well as its ability to simulate complex and curved boundaries with less number of elements and nodes for the same accuracy. The 8-node fictitious surface element is used to model the boundary conditions affecting the surface of the body. For a structure exposed to environmental conditions, these boundary conditions arise from solar radiation, convection to or from surrounding air, and irradiation to the sky.

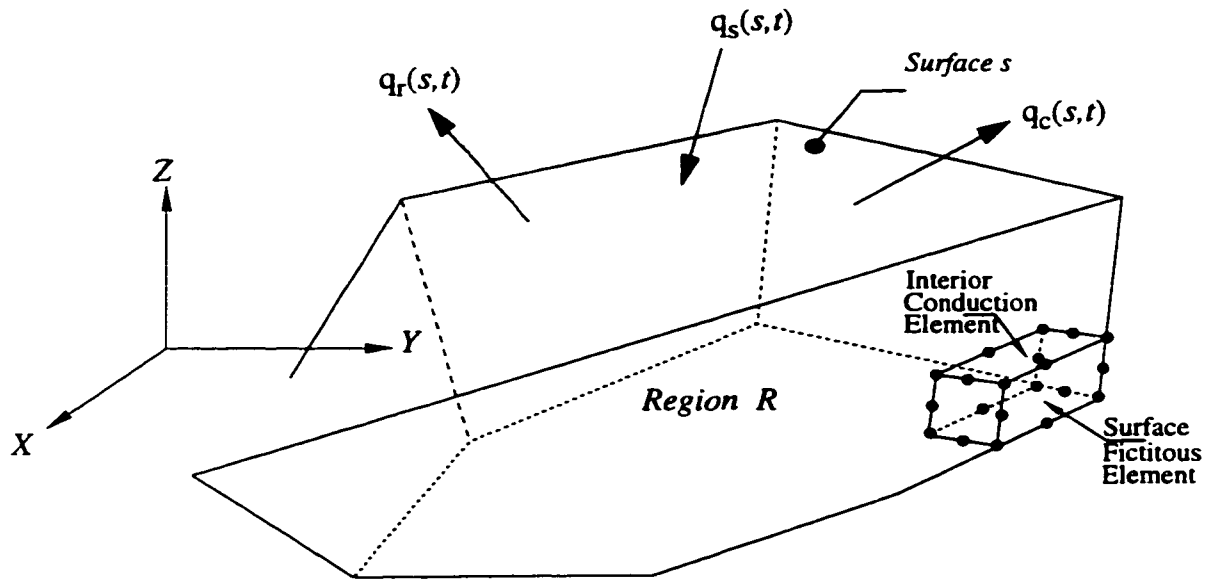

Figure 3.1 General discretized body using finite elements

The heat flow differential equation is a function of the space variables, x,y,z, and time t. In the formulation of a finite element solution of this equation, the variational principle is employed on the space variables to obtain a first-order differential equation in time; then, the Galerkin's principle is used to solve the resulting equation in the time domain.

In the variational formulation, a functional Π is defined in an integral form to represent a scaler quantity. Thus, the heat flow differential equations (3.1) and (3.2) may be expressed as: [Bathe (1982)]

$$\Pi = \int_V \frac{1}{2} k \left[\left(\frac{\partial T}{\partial x}\right)^2 + \left(\frac{\partial T}{\partial y}\right)^2 + \left(\frac{\partial T}{\partial z}\right)^2 \right] dV + \int_V \rho c T \frac{\partial T}{\partial t} dV - \int_V TQ dV - \int_A T_s q dA \qquad (3.10)$$

in which T_s is the temperature of the surface at time t; dA and dV are elemental surface area and volume, respectively. The rest of the notations are the same as for Equations (2.1) and (2.2).

In order to minimize this functional, it is required to find a function T which makes Π stationary with respect to small changes of δT (i.e. T must satisfy $\delta\Pi = 0$) [Zienkiewicz and Taylor (1991)].

$$\delta\Pi = \int_V k \left[\left(\frac{\partial T}{\partial x}\right) \left(\frac{\partial}{\partial x}\delta T\right) + \left(\frac{\partial T}{\partial y}\right) \left(\frac{\partial}{\partial y}\delta T\right) + \left(\frac{\partial T}{\partial z}\right) \left(\frac{\partial}{\partial x}\delta T\right) \right] dV + \int_V \rho c \delta T \frac{\partial T}{\partial t} dV$$
$$- \int_V \delta TQ dV - \int_A \delta T_s q dA = 0 \qquad (3.11)$$

The function T can be approximated using the smoothing piecewise interpolation equation for each element in the discretized body of Figure 3.1. Therefore, for any point within an

element e at any time t:

$$T(x, y, z, t)^e = [N]\ \{T\}^e \tag{3.12}$$

in which $[N]$ = interpolation shape functions, chosen so that $T(x, y, z, t)^e$ is continuous within element e,

and $\{T\}^e$ = vector of nodal temperatures for element e.

Substituting Equation (3.12) into Equation (3.11) for one element and summing up over the elements of region R in Figure 3.1 gives the following equation:

$$\begin{aligned}\delta\Pi = \sum_e \int_{V^e} k\Big[\Big(\frac{\partial [N]}{\partial x}\{T\}^e \frac{\partial [N]}{\partial x}\{\delta T\}^e\Big) + \Big(\frac{\partial [N]}{\partial y}\{T\}^e \frac{\partial [N]}{\partial y}\{\delta T\}^e\Big) + \\ \Big(\frac{\partial [N]}{\partial z}\{T\}^e \frac{\partial [N]}{\partial z}\{\delta T\}^e\Big)\Big] dV + \sum_e \int_{V^e} \rho c\,[N]\,\{\delta T\}^e [N]\,\{\frac{\partial T}{\partial t}\}^e dV \\ - \sum_e \int_{V^e} [N]\,\{\delta T\}^e Q dV - \sum_e \int_{A^e} [N]\,\{\delta T_s\}^e q dA = 0\end{aligned} \tag{3.13}$$

Rearranging the terms in the previous equation yields:

$$\begin{aligned}\delta\Pi = \sum_e \{\delta T\}^e \Big\{ \int_{V^e} k\Big[\Big(\frac{\partial [N]}{\partial x}\{T\}^e \frac{\partial [N]}{\partial x}\Big) + \Big(\frac{\partial [N]}{\partial y}\{T\}^e \frac{\partial [N]}{\partial y}\Big) + \\ \Big(\frac{\partial [N]}{\partial z}\{T\}^e \frac{\partial [N]}{\partial z}\Big)\Big] dV + \int_{V^e} \rho c\,[N]^T [N]\,\{\frac{\partial T}{\partial t}\}^e dV \\ - \int_{V^e} [N]^T Q dV - \int_{A^e} [N]^T q dA\ \Big\} = 0\end{aligned} \tag{3.14}$$

As $\{\delta T\}^e$ equal zero is always true, the terms inside the curly brackets also equal zero, thus:

$$\sum_e \{ \int_{V^e} k \Big[(\frac{\partial [N]}{\partial x} \{T\}^e \frac{\partial [N]}{\partial x}) + (\frac{\partial [N]}{\partial y} \{T\}^e \frac{\partial [N]}{\partial y}) + (\frac{\partial [N]}{\partial z} \{T\}^e \frac{\partial [N]}{\partial z}) \Big] dV + \int_{V^e} \rho c [N]^T [N] \{\frac{\partial T}{\partial t}\}^e dV - \int_{V^e} [N]^T Q dV - \int_{A^e} [N]^T q dA \} = 0 \tag{3.15}$$

Grouping the terms yields:

$$\sum_e [k]^e \{T(t)\}^e + \sum_e [C]^e \frac{\partial \{T(t)\}^e}{\partial t} - \sum_e \{F(t)\}^e = 0 \tag{3.16}$$

in which $[k]^e$ = element conduction matrix,

$[C]^e$ = element heat capacity matrix,

and $\{F(t)\}^e$ = element thermal load vector.

The element conduction matrix $[k]^e$ contributes to the global conduction matrix of the whole discretized body of Figure 3.1. This contribution is different for the interior element (20-node element) than that obtained from the surface boundary element (8-node element). For the interior element, the element conduction matrix is due to conduction and denoted as the element conductivity matrix $[k]_c^e$. This matrix is represented by the following expression:

$$[k]_c^e = \int_{V^e} [B]^T [D] [B] dV \tag{3.17}$$

in which $[D]$ = matrix consisting of the thermal conductivity values. For isotropic material, $[D]$ is defined as:

$$[D] = \begin{bmatrix} k & 0 & 0 \\ 0 & k & 0 \\ 0 & 0 & k \end{bmatrix} \tag{3.18}$$

and $[B]$ = matrix consisting of the first derivatives of the element shape functions with respect to the space variables x,y,z.

$$[B] = \begin{bmatrix} \dfrac{\partial [N]}{\partial x} \\ \dfrac{\partial [N]}{\partial y} \\ \dfrac{\partial [N]}{\partial z} \end{bmatrix} \tag{3.19}$$

For the surface boundary element, the element matrix that contributes to the system conduction matrix is due to convection and irradiation and is denoted as $[k]^e_{cr}$. This element matrix is given by:

$$[k]^e_{cr} = \int_{A^e} h(s,t)\,[N]^T [N]\, dA \tag{3.20}$$

where A^e is the area of the surface boundary element and $h(s,t)$ is the overall heat transfer coefficient [equation (3.9)].

It should be noted that $[k]^e$ varies with time since $[k]^e_{cr}$ is a function of time.

The element heat capacity matrix, $[C]^e$, can be determined from the following expression:

$$[C]^e = \int_{V^e} \rho c\,[N]^T [N]\, dV \tag{3.21}$$

For the element thermal load vector, $\{F(t)\}^e$, the contribution from the interior element to the global load vector is different from that obtained from the surface boundary element. For the interior element, the thermal load vector, $\{F(t)\}_i^e$, is due to heat generated within the element (e.g., heat of hydration), and is given by:

$$\{F(t)\}_i^e = \int_{V^e} Q\,[N]^T dV \tag{3.22}$$

For the surface boundary element, the thermal load vector, $\{F(t)\}_b^e$, is the sum of two components: solar radiation, $\{Q_s(t)\}^e$, and convection and irradiation, $\{Q_{cr}(t)\}^e$. Thus:

$$\{F(t)\}_b^e = \int_{A^e} q\,[N]^T dA = \{Q_s(t)\}^e + \{Q_{cr}(t)\}^e \tag{3.23}$$

where

$$\{Q_s(t)\}^e = \int_{A^e} q_s(t)\,[N]^T dA \tag{3.24}$$

and

$$\{Q_{cr}(t)\}^e = \int_{A^e} h(s,t)T_a(t)\,[N]^T dA \tag{3.25}$$

Derivation of the element matrices, the element thermal load vectors, and other properties of the elements employed in the formulation can be found in many references [e.g. Cook (1981)].

The integrals involved in generating the element matrices and thermal load vectors [Equations (3.17) and (3.20) to (3.25)] are usually evaluated numerically employing Gauss

quadrature technique. In the present study, 3x3x3 and 3x3 Gauss points are used for 20-node and 8-node elements, respectively.

Assembling the element contributions over the region R of Figure 3.1, and rewriting Equation (3.16), yield the following system of first order linear differential equations in time:

$$[C]\frac{d}{dt}\{T(t)\} + [k]\{T(t)\} - \{F(t)\} = 0 \tag{3.26}$$

in which: $[C]$ = heat capacity matrix of the system,

$$[C] = \sum^{n_i} [C]^e \tag{3.27}$$

$[k]$ = heat conduction matrix of the system,

$$[k] = \sum^{n_i} [k]_c^e + \sum^{n_b} [k]_{cr}^e \tag{3.28}$$

$\{F(t)\}$ = thermal load vector of the system,

$$\{F(t)\} = \sum^{n_i} \{F(t)\}_i^e + \sum^{n_b} \{F(t)\}_b^e \tag{3.29}$$

$\{T(t)\}$ = nodal temperature vector of the system,

n_i = number of interior conduction elements,

and n_b = number of boundary fictitious elements.

3.2.3 Numerical Solution of First Order Differential Equations

The resulting system of linear differential equations as a function of time, Equation (3.26), must be solved to find the temperature values at all nodes for a given time t. Several techniques are available to find this solution at different points in the time domain. Two techniques are most popular: the Crank-Nicholson time-stepping technique, and the Galerkin's weighted residual technique. Elbadry (1982), compared the two techniques in terms of accuracy of results and oscillation of solution when solving a heat transfer problem. He concluded that Galerkin's method provides more accurate results with less oscillation, even when large time increments are used.

In the following section, a brief summary of the formulation of Galerkin's method to solve Equation (3.26) is presented, in order to obtain the nodal temperature values at different points in the time domain.

Assume that the time domain is divided into a number of equal increments Δt, and that the temperature and thermal loads at a typical node are varying linearly within each time increment.

The temperature and thermal loads can be approximated using linear shape functions N_i, and N_j as follows (see Figure 3.2):

$$\{T\} = N_i \{T\}_i + N_j \{T\}_j \tag{3.30}$$

$$\{F\} = N_i \{F\}_i + N_j \{F\}_j \tag{3.31}$$

$$[k]\{T\} = N_i([k]\{T\})_i + N_j([k]\{T\})_j \tag{3.32}$$

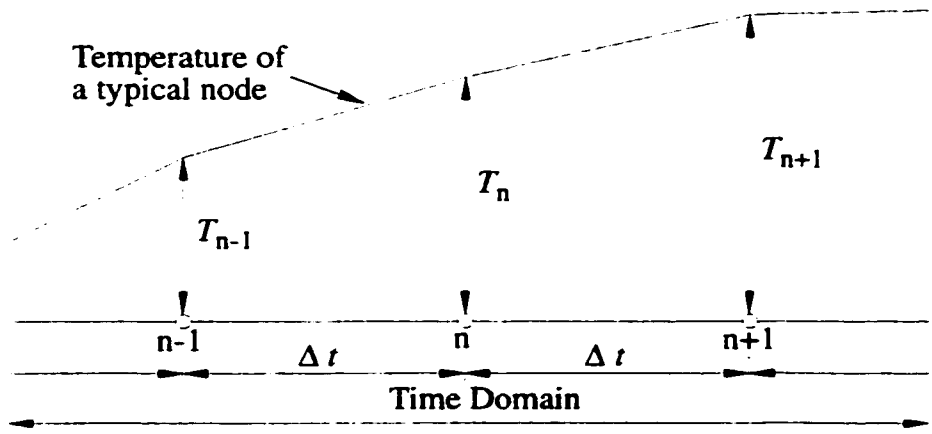

a) Time span divided into finite increments.

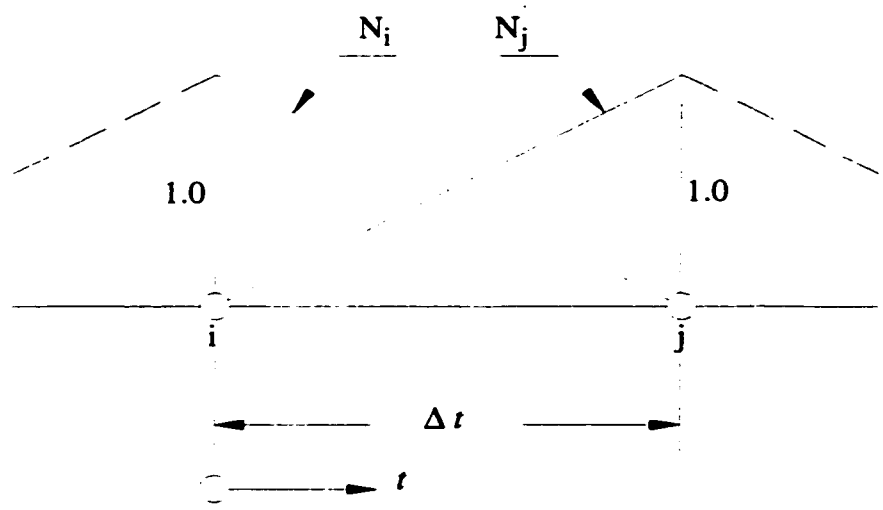

b) Linear shape functions for a finite time element Δt.

Figure 3.2 Variation of temperature with time.

where

$$N_i = 1 - \frac{t}{\Delta t} \tag{3.33}$$

$$N_j = \frac{t}{\Delta t} \tag{3.34}$$

Application of Galerkin's weighted residual method involves introduction of a residual error term $\{L\}$. The error term results from the substitution of the approximate solution, Equations (3.30-3.32), into the system of first order differential equations, Equation (3.26).

$$\{L\} = [C]\frac{d}{dt}\{T\} + [k]\{T\} - \{F\} \tag{3.35}$$

This residual error term is then multiplied by a weighting function W_i and the integral of the product is set to zero.

$$\int_0^{\Delta t} W_i L(t)\, dt = 0 \tag{3.36}$$

Substituting from Equation (3.35) into Equation (3.36) and choosing N_j as the weighting function [Elbadry (1982)] yield the following integral:

$$\int_0^{\Delta t} N_j \left([C]\frac{d}{dt}\{T\} + [k]\{T\} - \{F\} \right) = 0 \tag{3.37}$$

Performing the integral over a time period of Δt gives the following recurrence equation:

$$\left(\frac{1}{\Delta t}[C] + \frac{2}{3}[k]_{n+1}\right)\{T\}_{n+1} = \left(\frac{1}{\Delta t}[C] + \frac{1}{3}[k]_n\right)\{T\}_n + \frac{2}{3}\{F\}_{n+1} + \frac{1}{3}\{F\}_n \tag{3.38}$$

This recurrence equation has been proved to be unconditionally stable [Zienkiewicz and Taylor (1991)] and can be used to find $\{T\}_{n+1}$ provided that $\{T\}_n$ is known. In the incremental transient analysis, the initial temperature (temperature at time $t = 0$) must be assumed in order to compute the temperatures at subsequent time steps (see Chapter 5).

It should be noted that solution of Equation (3.38) to find $\{T\}_{n+1}$ requires that the irradiation heat transfer coefficient, $h_{r,n+1}$, and, hence, the overall heat transfer coefficient, h_{n+1}, be known for the generation of $[k]^e_{cr}$ and $\{Q_{cr}(t)\}^e$; see Equations (3.20) and (3.25). However, $h_{r,n+1}$, can not be determined unless the values of $\{T\}_{n+1}$ are known; see Equation (3.8). Therefore, an approximate value of h_r can be estimated by extrapolation from values of h_r at time steps n and n-1 [Maes (1980)]; thus:

$$h_{r,n+1} = 2h_{r,n} - h_{r,n-1} \tag{3.39}$$

Such approximation was also adopted by Elbadry and Ghali (1983a) and implemented in program FETAB [Elbadry and Ghali (1982)].

3.3 Thermal Stresses and Displacements

3.3.1 Finite Element Formulation

Once the nodal temperatures are determined, [solution of Equation (3.26)], the resulting displacements and stresses induced in the structure can be calculated.

The stresses induced in a body of arbitrary geometry can be defined from Hooke's law [Ugural and Fenster (1981)]:

$$\{\sigma\} = [E]\,(\{\varepsilon\} - \{\varepsilon_o\}) + \{\sigma_o\} \tag{3.40}$$

where $\{\sigma\}$ = vector of total stresses induced in the body,

$$\{\sigma\} = \begin{Bmatrix} \sigma_x \\ \sigma_y \\ \sigma_z \\ \tau_{xy} \\ \tau_{yz} \\ \tau_{zx} \end{Bmatrix} \tag{3.41}$$

$\{\varepsilon\}$ = vector of mechanical strains exhibited by the body,

$$\{\varepsilon\} = \begin{Bmatrix} \varepsilon_x \\ \varepsilon_y \\ \varepsilon_z \\ \gamma_{xy} \\ \gamma_{yz} \\ \gamma_{zx} \end{Bmatrix} \tag{3.42}$$

$[E]$ = matrix of material stiffness,

$$[E] = \frac{E}{(1+\nu)(1-2\nu)} \begin{bmatrix} 1-\nu & \nu & \nu & 0 & 0 & 0 \\ \nu & 1-\nu & \nu & 0 & 0 & 0 \\ \nu & \nu & 1-\nu & 0 & 0 & 0 \\ 0 & 0 & 0 & \frac{(1-2\nu)}{2} & 0 & 0 \\ 0 & 0 & 0 & 0 & \frac{(1-2\nu)}{2} & 0 \\ 0 & 0 & 0 & 0 & 0 & \frac{(1-2\nu)}{2} \end{bmatrix} \tag{3.43}$$

for which E = Young's modulus of the material,

ν = Poisson's ratio.

$\{\varepsilon_o\}$ = vector of initial strains,

and, $\{\sigma_o\}$ = vector of initial stresses.

Temperature effects on a body can be viewed as a case of initial strain $\{\varepsilon_o\}$. For example, the free expansion of an isotropic body subjected to a rise of temperature T above an arbitrary reference temperature produces the following strains:

$$\{\varepsilon_o\} = \{\alpha T \quad \alpha T \quad \alpha T \quad 0 \quad 0 \quad 0\}^T \tag{3.44}$$

where α = the coefficient of thermal expansion.

Thus, to calculate the thermally induced stresses in a body, Equation (3.40) may be reduced to the following:

$$\{\sigma\} = [E](\{\varepsilon\} - \{\varepsilon_o\}) \tag{3.45}$$

It should be noted that when mechanical strains are prevented (i.e. total fixation of the boundaries), the stresses induced in the body are: $\{\sigma\} = -[E]\{\varepsilon_o\}$. Also, when the boundary restraints permits unrestricted expansion or contraction, the material is homogeneous, and the temperature field $T(x,y,z)$ is planer, all stresses are equal to zero.

Therefore, to find the total thermal stresses induced in a body, Equation (3.45), knowing the material properties $[E]$ and the initial strains $\{\varepsilon_o\}$, the mechanical strains are to be calculated. The mechanical strains $\{\varepsilon\}$ at any point on the discretized body of Figure 3.3 are related to the displacement functions (Degrees of Freedom) $U = \{u \quad v \quad w\}^T$ (i.e. the displacement of any point on the body measured from its original position corresponding to the global axes) by the following relation:

$$\begin{Bmatrix} \varepsilon_x \\ \varepsilon_y \\ \varepsilon_z \\ \gamma_{xy} \\ \gamma_{yz} \\ \gamma_{zx} \end{Bmatrix} = \begin{bmatrix} \frac{\partial}{\partial x} & 0 & 0 \\ 0 & \frac{\partial}{\partial y} & 0 \\ 0 & 0 & \frac{\partial}{\partial z} \\ \frac{\partial}{\partial y} & \frac{\partial}{\partial x} & 0 \\ 0 & \frac{\partial}{\partial z} & \frac{\partial}{\partial y} \\ \frac{\partial}{\partial z} & 0 & \frac{\partial}{\partial x} \end{bmatrix} \begin{Bmatrix} u \\ v \\ w \end{Bmatrix} \tag{3.46}$$

At the element level, the displacements at the nodes of the element $\{\bar{q}\}$ affect the strain distribution within the element e as per the relation:

$$\{\varepsilon\}^e = [\bar{B}]\,\{\bar{q}\}^e \tag{3.47}$$

where $\{\bar{q}\}^e$ = vector of nodal displacements of the element,

$[\bar{B}]$ = strain displacement matrix, given as:

$$[\bar{B}] = \begin{bmatrix} \frac{\partial [N]}{\partial x} & 0 & 0 \\ 0 & \frac{\partial [N]}{\partial y} & 0 \\ 0 & 0 & \frac{\partial [N]}{\partial z} \\ \frac{\partial [N]}{\partial y} & \frac{\partial [N]}{\partial x} & 0 \\ 0 & \frac{\partial [N]}{\partial z} & \frac{\partial [N]}{\partial y} \\ \frac{\partial [N]}{\partial z} & 0 & \frac{\partial [N]}{\partial x} \end{bmatrix} \tag{3.48}$$

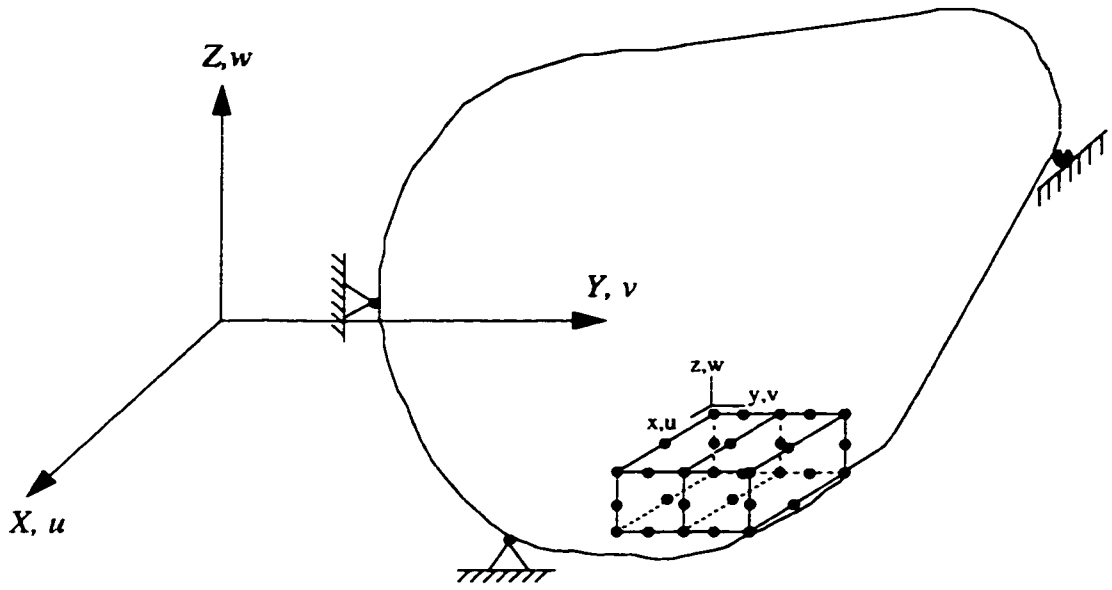

Figure 3.3 General three-dimensional body

Employing the variational principle of the finite element method to obtain the governing equilibrium equations of the discretized body of Figure 3.3, the functional Π may be defined in terms of the strain energy stored in the body as:

$$\Pi = \int_V \frac{1}{2} \{\sigma\}^T \{\varepsilon\} \, dV \tag{3.49}$$

Substituting Equation (3.45) into Equation (3.49) gives:

$$\Pi = \frac{1}{2} \int_V \{\varepsilon\}^T [E] \left(\{\varepsilon\} - \{\varepsilon_\circ\} \right) dV \tag{3.50}$$

Substituting Equation (3.47) into Equation (3.50) and rewriting the functional Π for all elements, Equation (3.50) becomes:

$$\Pi = \sum_e \frac{1}{2} \int_V \left([\bar{B}] \{\bar{q}\}^e \right)^T [E] \left([\bar{B}] \{\bar{q}\}^e - \{\varepsilon_\circ\} \right) dV \tag{3.51}$$

Rearranging the terms in the previous equation, it can be shown that:

$$\begin{aligned} \Pi = & \sum_e \frac{1}{2} \left(\{\bar{q}\}^e \right)^T \int_{V^e} [\bar{B}]^T [E] \, [\bar{B}] \, dV \, \{\bar{q}\}^e \\ & - \sum_e \frac{1}{2} \left(\{\bar{q}\}^e \right)^T \int_{V^e} [\bar{B}]^T [E] \, \{\varepsilon_\circ\} \, dV \end{aligned} \tag{3.52}$$

Invoking the stationary of Π such that $\delta\Pi = 0$ for small changes of $\delta\{\bar{q}\}^e$;

$$\begin{aligned} \delta\Pi = & \sum_e \frac{1}{2} \left(\delta \{\bar{q}\}^e \right)^T \left(\int_{V^e} [\bar{B}]^T [E] \, [\bar{B}] \, dV \right) \{\bar{q}\}^e \\ & - \sum_e \frac{1}{2} \left(\delta \{\bar{q}\}^e \right)^T \left(\int_{V^e} [\bar{B}]^T [E] \, \{\varepsilon_\circ\} \, dV \right) = 0 \end{aligned} \tag{3.53}$$

As $\delta\{\bar{q}\}^e$ equal zero is always true, the adjoint terms must also be equal to zero. This yields:

$$\sum_e \left(\int_{V^e} [\bar{B}]^T [E]\ [\bar{B}]\, dV \right) \{\bar{q}\}^e = \sum_e \int_{V^e} [\bar{B}]^T [E]\ \{\varepsilon_o\}\, dV \tag{3.54}$$

Grouping the terms yields:

$$\sum_e [\bar{k}]^e \{\bar{q}\}^e = \sum_e \{\bar{R}\}^e \tag{3.55}$$

where $[\bar{k}]^e$ = element stiffness matrix,

$$= \int_{V^e} [\bar{B}]^T [E]\ [\bar{B}]\, dV$$

and $\{\bar{R}\}^e$ = vector of thermal nodal forces, to which the element must be subjected in order that there are no nodal displacements.

$$= \int_{V^e} [\bar{B}]^T [E]\ \{\varepsilon_o\}\, dV$$

The element stiffness matrix $[\bar{k}]^e$ and element load vector $\{\bar{R}\}^e$ for the 20-node solid element are normally generated using Gauss quadrature technique [Zienkiewicz, and Taylor (1991)]. In the present work, 27 Gauss sampling points were found sufficient.

Assemblage of the element contribution over the discretized body of Figure 3.3 gives the governing equilibrium equations of the system. Each equation represents one degree of freedom at each of the different nodal points in the discretized body:

$$[\bar{k}]\ \{U\} = \{\bar{R}\} \tag{3.56}$$

where $[\bar{k}]$ = system stiffness matrix,

$\{U\}$ = vector of nodal displacements of the system,

and $\{\bar{R}\}$ = vector of thermal nodal forces of the system.

The above system of equations can not be solved to obtain nodal displacements or stresses at a particular time t, unless the boundary restraints are defined.

3.3.2 Imposition of Boundary Restraints

The effect of specified displacements and/or essential boundary conditions can be incorporated into the system stiffness matrix $[\bar{k}]$ by using either the elimination approach or the penalty approach. The penalty approach is adopted to introduce the effect of boundary restraints into the singular matrix $[\bar{k}]$, since it is easy enough to implement in a computer program and it retains its simplicity even when considering general restraint conditions [Chandrupatla and Belegundu (1991)].

In the penalty approach, a spring with large stiffness H is used to model the support condition (see Figure 3.4b). For a spring (support) where the specified displacement equals a along degree of freedom i ($U_i = a$), it can be shown that the strain energy stored in the spring equals:

$$\Pi_s = \frac{1}{2} H (U_i - a)^2 \tag{3.57}$$

This strain energy produced by the spring (support) contributes to the total strain energy of the system; thus, rewriting the functional Π of Equation (3.56) considering this contribution yields:

$$\Pi = \frac{1}{2} \{U\}^T [\bar{k}] \{U\} + \frac{1}{2} H (U_i - a)^2 - \{U\}^T \{\bar{R}\} \tag{3.58}$$

The same procedure to obtain the stationary of Π is used (as discussed in the previous section), and the resulting finite element equations can be written in the form:

$$[\bar{k} + \bar{k}_c]\,\{U\} = \{\bar{R} + \bar{R}_c\} \tag{3.59}$$

where $[\bar{k}_c]$ = constraint stiffness matrix of the system, with values only at places of restrained DOF's and zeros elsewhere.

$\{\bar{R}_c\}$ = constraint force vector of the system, with values only at places of restrained DOF's and zeros elsewhere.

The system constraint stiffness matrix and force vector are assembled from the individual constraint stiffness matrices and force vectors which are derived for each supported node:

$$[\bar{k}_c] = \sum^{n_s} [\bar{k}_c]^s \tag{3.60}$$

$$\{\bar{R}_c\} = \sum^{n_s} \{\bar{R}_c\}^s \tag{3.61}$$

where $[\bar{k}_c]^s$ = constraint stiffness matrix of a supported node, of size 3x3,

$\{\bar{R}_c\}^s$ = constraint force vector of the supported node, of size 3x1,

n_s = number of supported nodes in the system.

When the prescribed displacement is in a direction parallel to the global axes, the constraint stiffness matrix has diagonal terms only, each of value equals H. These terms, after being assembled into $[\bar{k}_c]$, are added to certain diagonal terms in $[\bar{k}]$, as specified by the constrained DOF's in the system. The constraint force vector has terms equal to the prod-

uct (Ha). These values are added to specific terms in $\{\bar{R}\}$ according to the constrained DOF's [see Equation (3.52)]. The magnitude of H is chosen as the value of the largest element in $[\bar{k}]$ multiplied by 10^4. The choice of 10^4 "has been found satisfactory on most computers" [Chandrupatla and Belegundu (1991)].

The constraint stiffness matrix and the constraint force vector derived above are applicable only when the prescribed displacement is directed along the same direction of DOF. However, for implementation on a curved bridge geometry, the support restraints are not necessarily acting in a direction parallel to the global DOF's. These types of restraints are often known as "skew supports". A special treatment to deal with this type of skew supports is required and is presented hereafter.

When a supported node is not free to move along a certain inclined line in space whose direction cosines are l, m, n (e.g. as in the case of ball bearing support), the restraint along this line can be represented by a spring with large stiffness. The constraint stiffness matrix of this type of restraint is given by [Chandrupatla and Belegundu (1991)]:

$$[\bar{k}_c]^s = H\begin{bmatrix} l^2 & lm & ln \\ lm & m^2 & mn \\ ln & mn & n^2 \end{bmatrix} \tag{3.62}$$

When the node is forced to lie in a given plane while being free to move along the normal direction (l, m, n) to this plane (e.g. roller support, see Figure 3.4 a), the constraint stiffness matrix is given by [Chandrupatla, and Belegundu (1991)]:

$$[\bar{k}_c]^s = H\begin{bmatrix} (1-l^2) & -lm & -ln \\ -lm & (1-m^2) & -mn \\ -ln & -mn & (1-n^2) \end{bmatrix} \tag{3.63}$$

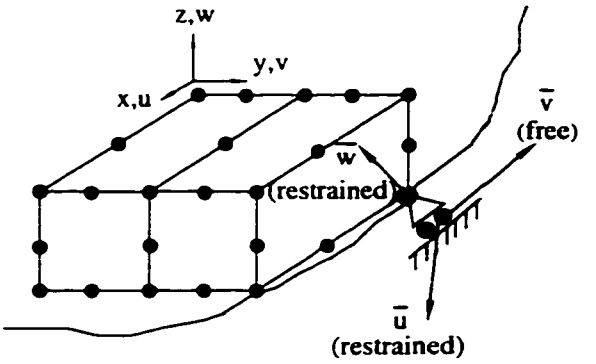

a) skew support in space.

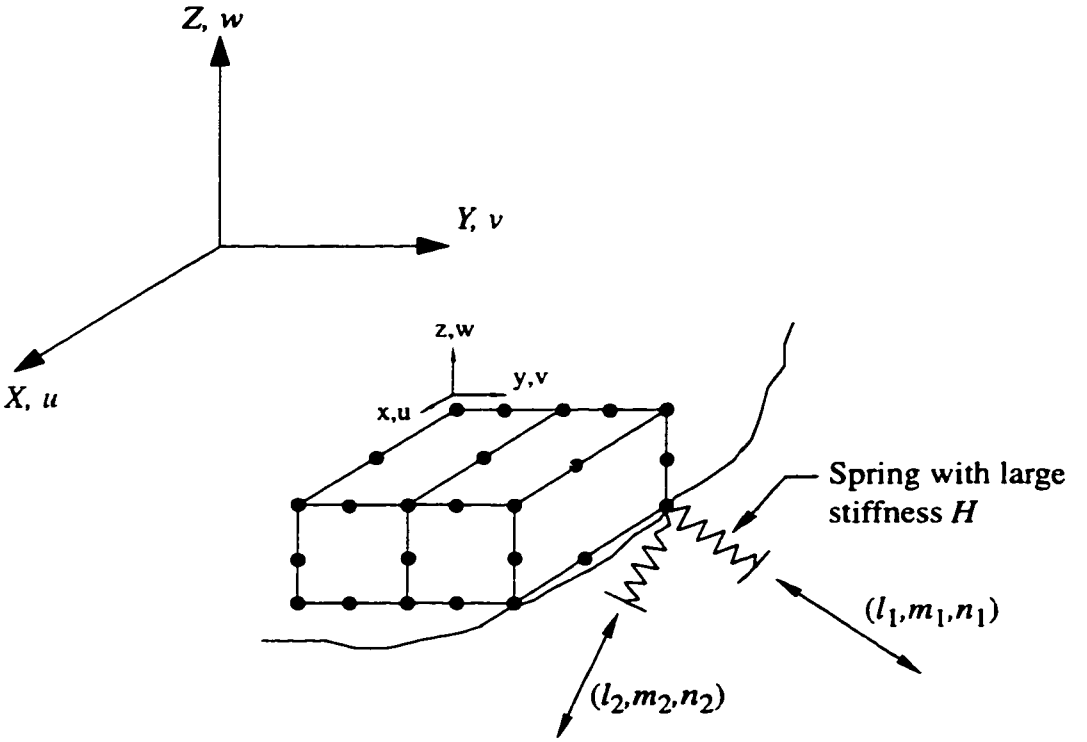

b) springs with large stiffness H modelling the restraints.

Figure 3.4 Skew boundary restraints imposed using spring elements.

For the support conditions described above, the prescribed displacement a is equal to zero; and thus, the constraint force vector will be equal to zero.

Assemblage of the constraint stiffness matrices and the constraint force vectors at the supported nodes gives the system constraint stiffness matrix and the system constraint force vector, respectively. Equation (3.59) can then be solved to obtain the nodal displacements $\{U\}$. Substituting these displacements for each element into Equation (3.47) gives the element mechanical strain $\{\varepsilon\}$. The total stresses $\{\sigma\}$ for each element can then be obtained from Equation (3.45). The stress values are calculated at Gauss sampling points (27 points were found sufficient).

The previous element stresses are calculated in the directions of global axes. However, since maximum values of stresses are of interest, it is more convenient to compute the principal stresses. Three principal stresses can be calculated using the following relationships [Ugural and Fenster (1981)]:

For the three invariants of the stress matrix:

$$
\begin{aligned}
I_1 &= \sigma_x + \sigma_y + \sigma_z \\
I_2 &= \sigma_x\sigma_y + \sigma_y\sigma_z + \sigma_x\sigma_z - \tau_{xy}^2 - \tau_{yz}^2 - \tau_{zx}^2 \\
I_3 &= \sigma_x\sigma_y\sigma_z + 2\tau_{xy}\tau_{yz}\tau_{zx} - \sigma_x\tau_{yz}^2 - \sigma_y\tau_{zx}^2 - \sigma_z\tau_{xy}^2
\end{aligned}
\tag{3.64}
$$

we can define:

$$
\begin{aligned}
C1 &= \frac{I_1^2}{3} - I_2 \\
C2 &= -2\left(\frac{I_1}{3}\right)^3 + \frac{I_1 I_2}{3} - I_3 \\
C3 &= 2\sqrt{\frac{C1}{3}} \\
\chi &= \frac{1}{3}\cos^{-1}\left(-\frac{3C2}{C1C3}\right)
\end{aligned}
\tag{3.65}
$$

The principal stresses are given by:

$$
\begin{aligned}
\sigma_1 &= \frac{I_1}{3} + C3\cos\chi \\
\sigma_2 &= \frac{I_1}{3} + C3\cos\left(\chi + \frac{2\pi}{3}\right) \\
\sigma_3 &= \frac{I_1}{3} + C3\cos\left(\chi + \frac{4\pi}{3}\right)
\end{aligned}
\tag{3.66}
$$

CHAPTER 4
PROGRAM *FETAB3D*

4.1 General

A computer program, ***FETAB3D***, is developed employing the formulation described in the previous chapter. ***FETAB3D:*** ***Three-Dimensional Finite Element Thermal Analysis of Bridges***, predicts the temperature distribution and the thermally induced stresses in box girder bridge structures. The developed program is an extension of the computer program ***FETAB*** developed by Elbadry and Ghali (1982) at the University of Calgary, to include three-dimensional finite elements to fully model box girder bridges for temperature and stress analysis. ***FETAB*** uses two-dimensional finite elements to calculate the temperature distribution within the cross-section of a box girder bridge, while it uses the displacement method of analysis to compute the self-equilibrating stresses induced in the bridge cross-section. In the following sections, the main features and capabilities of *FETAB3D* are described. Limitations of the program and memory requirement are also discussed. In addition, modelling of the environmental boundary conditions associated with box girder bridges are presented. Finally, verification problems are conducted to examine the validity of the developed program against both closed-form solutions and other available well-known finite element programs.

4.2 *FETAB3D* Main Features

4.2.1 Description of the program

FETAB3D is a three-dimensional finite element program which performs thermal analysis of bridges. The program predicts the temperature distribution within a box girder bridge of arbitrary plan and cross-section geometry for a given geographic location and meteorological conditions. The program also computes the total stresses developed in the bridge structure due to the predicted temperature distribution. The data required for the

analysis pertains to the thermal properties of the bridge material, the meteorological conditions at the location of the bridge, and the geometry of the bridge structure.

FETAB3D uses two types of elements: a 20-node isoparametric solid element to model the interior body of the structure; and an 8-node planar fictitious element to include the heat transfer boundary conditions affecting the surface of the structure. Different types of environmental boundary conditions are available in the program as illustrated in Figure 4.1. The program, coded in FORTRAN 77, has been used successfully on the Sun Sparc Stations at Concordia University.

4.2.2 Capability of the program

FETAB3D is capable of modelling any arbitrary geometry and support conditions of a box girder bridge. The material is assumed to be elastic, homogeneous, isotropic and independent of the temperature field. Nevertheless, variation in material properties from one element to another in the idealized finite element mesh is permitted, and thus composite bridges can be modelled.

Environmental boundary conditions acting on the bridge surfaces are functions of time and the location on the surface. In *FETAB3D*, this time-varying boundary effects are modelled using simple expressions and trigonometric functions. The environmental effects considered by the program are:

- Solar radiation intensity received by the surfaces of the bridge, based on the geographic location, day of the year, and time of the day.
- Convection between the surface of the bridge and the surrounding air (related to wind speed).
- Thermal irradiation between the surfaces and the surrounding, based on tempera-

ture- dependant values of the irradiation coefficient h_r.

- Diurnal variation of ambient air temperature as a function of the time of the day.
- Temperature variation of the still air inside the box section at any time of the analysis period.

When considering the effects of solar radiation on the outer surface of the web in box girder bridges, the program takes into account the length of shade provided by the overhanging cantilevers of the top slab.

The program in its current modular format allows the user to modify the solar radiation expressions as well as the ambient air temperature function. This feature makes the program usable for any climatological conditions, once the appropriate functions are derived, or calibrated against available meteorological data, and then incorporated into the program.

The program performs transient incremental analysis to determine the temperature values at all nodes in the structure. At the start of the analysis, initial nodal temperatures are required for the solution of the recurrence equation of Subsection 3.2.2 (Equation 3.38). *FETAB3D* assumes a uniform initial temperature throughout the structure equal to the ambient air temperature at the hour of the start of the analysis. The time period of the transient analysis is divided into finite time steps which can be of varying duration. At each time step, the program updates the values of the applied boundary conditions. A detailed description of modelling the boundary conditions is given in section 4.3.

The thermal stresses induced in the bridge can be obtained once the support conditions have been defined. The stresses are computed at the Gauss points in each element and are given as global and/or principal stresses.

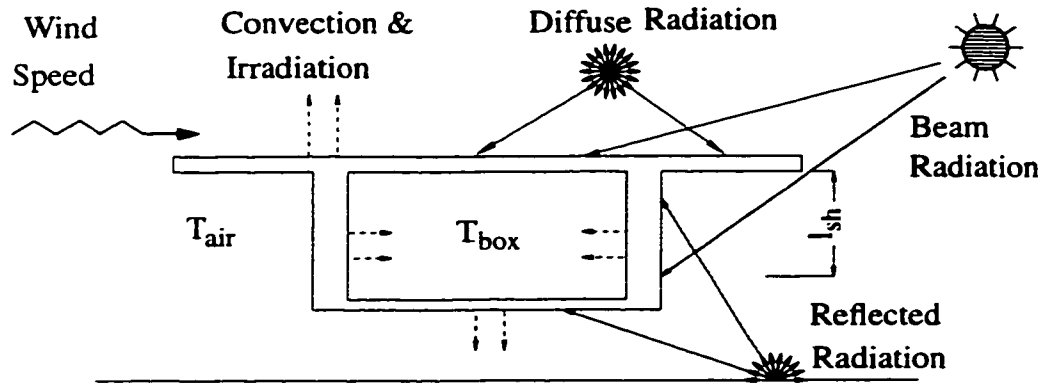

Figure 4.1 Environmental boundary conditions modeled by the program.

4.2.3 Memory Requirement

FETAB3D has been primarily developed to fully model bridge structures. Modelling of these structures may require a large number of nodes and elements. In order for the program to be capable of dealing with large systems, some advanced techniques have been employed to reduce the memory requirement of the system and enlarge the capacity of the program. These techniques are presented hereafter.

a) Dynamic Storage Allocation

All the arrays employed in the program to store the input or generated data, have variable dimensions. The dimensions of these arrays are set in the program at the time of execution and vary depending on the size of the problem. Nevertheless, as in the original program *FETAB*, all these variable sized arrays are stored in a one-dimensional common array which has a fixed preset dimension. The size of this one dimensional common array, however, can be changed by the user to suit the size of the problem at hand and the Random Access Memory (RAM) of the particular computer used for the analysis. This feature allows the program more flexibility to match the different computer platforms available (IBM, CDC, SUN,VAX, etc.).

b) Compacted Column Storage Scheme

During the execution of the program, the most exhausting operation to the memory of the computer is the storage of the coefficient matrices (the conduction, $[k]$, and capacitance, $[C]$, matrices when calculating temperature, and the stiffness matrix, $[\bar{k}]$, when calculating stresses). In large systems, these matrices require very large storage space. In *FETAB3D*, a compacted column storage scheme (sometimes referred to as "sky line" or "active column" storage) is adopted to store these coefficient matrices. In this storage scheme, only non-zero elements of the symmetric coefficient matrix are stored in a one dimensional variable-size array. This scheme is preferred to the traditional skew banded

storage scheme since it maintains the storage requirement to a minimum. Figure 4.2 shows the memory requirement savings for the active column storage over that of skew banded scheme.

c) Auxiliary Storage

In the analysis of very large problems, the compacted column storage scheme is, sometimes, unable to accommodate all the storage of the coefficient matrices in the central memory of the computer ("core"). Thus, auxiliary storage on tapes or discs ("out of core") must be used in order to fully store these coefficient matrices. *FETAB3D* uses auxiliary storage to facilitate the solution of such large scale problems. In the analysis technique using the auxiliary storage, each coefficient matrix is segmented into blocks. Each block contains a different number of active columns of the coefficient matrix (See Figure 4.3). The coefficient matrix is then assembled block by block and stored sequentially on tape or disc.

For the solution of the equations of the problem, each coefficient matrix is stored in block form, out of core, as indicated above. Each block is then retrieved to the core, and the solution is obtained by performing the standard procedure (triangular decomposition, and backward substitution) on each block, as well as the load vector (the load vector is rather left to be fully stored in core since it requires small storage as compared to the coefficient matrices). A detailed description of this technique (referred to as "Block Partitioning") is given by Wilson, Bathe, and Dohrty (1974), and Mondkar and Powell (1974).

Implementation of this technique implies that it would be only necessary to accommodate two blocks of the coefficient matrix in the computer core at the same time, instead of the whole coefficient matrix. Furthermore, the block size is pre-determined so that it can fit into the available core storage of the computer used in the analysis.

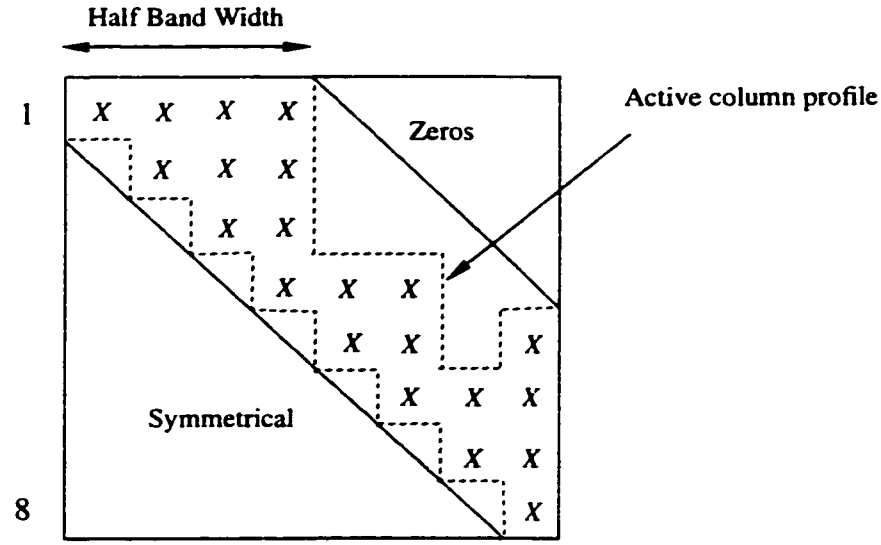

a) Coefficient matrix

X : Non Zero element

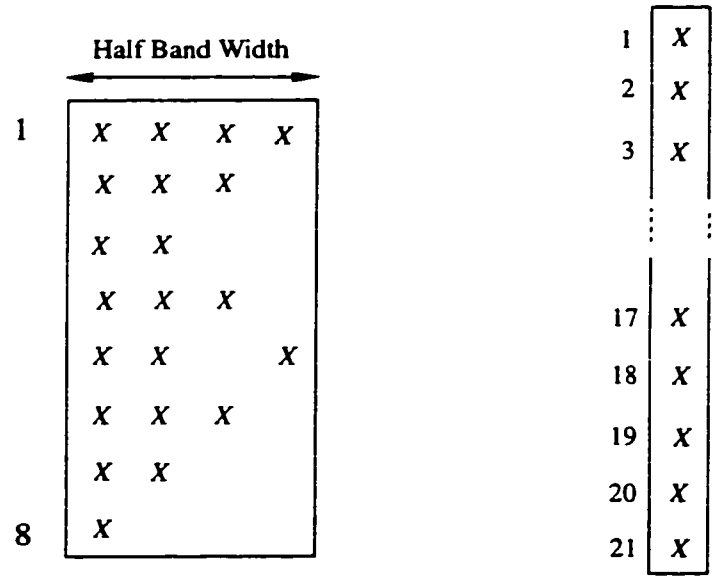

b) Skew Banded storage

c) Active column storage

Figure 4.2 Comparison between Banded and Active column storage schemes

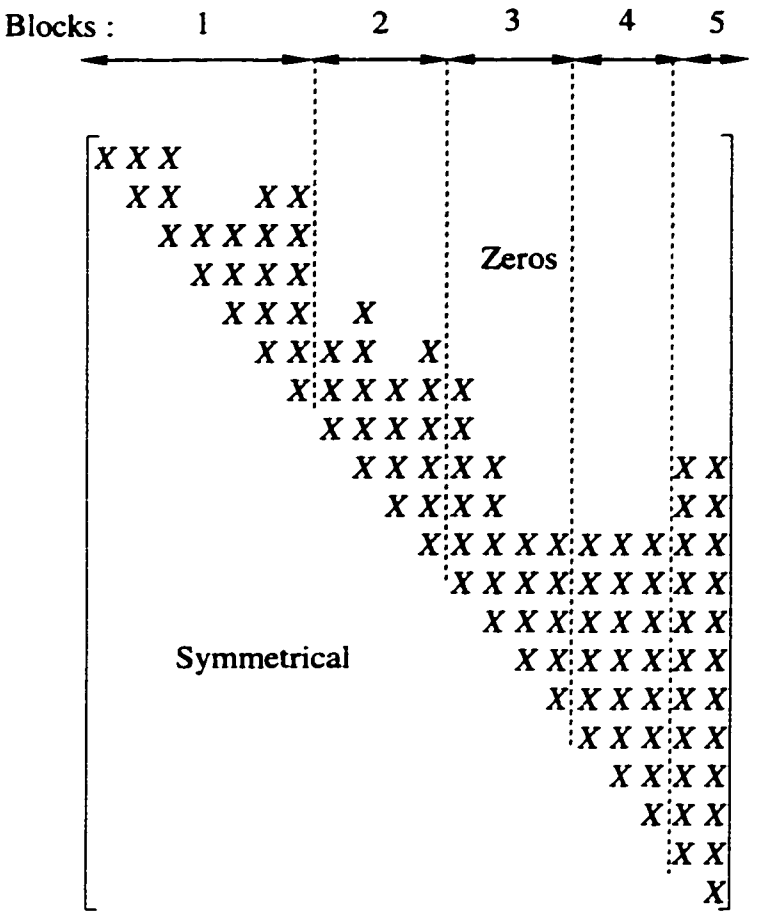

Figure 4.3 Example of Block Partitioning of a coefficient matrix

Applying this technique in *FETAB3D* extends the capacity of the program to solve problems of unlimited size, based on the core storage of the computer used in the analysis. However, it should be mentioned that this technique results in an increase in execution time of the problem due to lengthy I/O operations, plus some complexity in assemblage of the coefficient matrices.

4.2.4 Limitations of the Program

a) Size of the Problem

Although the procedure described above can, virtually, solve problems of any size, the ability to effectively use this technique is largely dependant on the available core storage. The core storage of the computer used in the analysis should be large enough to:

- Exceed twice the height of the tallest active column in the coefficient matrix.
- Accommodate two blocks of the coefficient matrix used in the solution of equations at the same time (this step occurs during the decomposition phase of the solution process).

In *FETAB3D*, an error message is given on the screen in the event that the aforementioned limits are exceeded. The user is then asked to increase the size of the one-dimensional common array (see Dynamic Storage Allocation above).

In addition to the previous conditions, *FETAB3D* sets up a limit of 1000 blocks as a practical maximum limit of the size of the problem. However, this limit can be increased by the user to any desired value. A message is displayed to indicate that the maximum number of blocks is exceeded if this occurs.

A detailed description of how to increase the size of the one-dimensional common array and/or the number of blocks limit is given in the reference manual of the computer program [Ibrahim, Elbadry and El-Ariss (1995)] . It is understood that the FORTRAN source code must be recompiled, whenever the program is modified.

b) Geometry and Boundary Conditions

FETAB3D is not capable of handling a box girder bridge of more than one cell. The thermal effect due to heat of hydration at the early ages of the bridge is not considered among the different boundary conditions available in the program. *FETAB3D*, however, with its modular structured format, is readable and extendable to any other routine that fits the user's application.

c) Preprocessing and Postprocessing

FETAB3D has a simple routine to perform nodal generation in one and two dimensions (line and surface). Volume nodal generation is not yet included in the program. Simple element generation capability is also available; more advanced element generation is yet to be included.

Automatic node renumbering to reduce the bandwidth of the problem is not available, hence the user is asked to maintain the best possible node numbering scheme manually, prior to mesh data input. The results of the analysis are printed into an output file. Neither graphic display nor contour plotting is available in the program.

4.3 Modelling of Environmental Boundary Conditions

The environmental conditions of solar radiation, convection and irradiation that affect the surfaces of a bridge structure should be accurately modeled, if the temperature distribution within the structure and the resulting stresses are required. These boundary conditions have been considered successfully by several researchers, among them: Lanigan (1973), Priestly (1976), Dilger et al. (1983), Elbadry and Ghali (1983a), and Clark (1989).

In the previous chapter, the equations governing the quantities of these boundary conditions were briefly discussed (see Subsection 3.2.1). Solar radiation is the main source of heat in bridge structures. Convection and thermal irradiation are affected by the ambient air temperature , T_a; see Equations (3.4) to (3.8). In box girder bridges, the ambient temperature inside the box is different from the outside air temperature. Convection is influenced also by wind speed. This influence is included, among other factors, in the value of convection heat transfer coefficient, h_c. Kehlbeck (1975) suggested empirical formulas to determine the values of h_c in terms of wind speed for different surfaces of box girders (see Table 4.1). In the following, the expressions used in the present program to model the variation with time of solar radiation intensity and ambient air temperature are presented.

4.3.1 Solar Radiation

The total solar radiation, I, [see Equation (3.3)] consists mainly of three components: direct (or beam) radiation I_b, diffuse radiation I_d, and reflected radiation I_r (see Figure 4.1). The direct radiation is the solar energy reaching the earth without being scattered or absorbed by the atmosphere. Its value incident upon a horizontal surface I_{bh}, is given as [Duffie and Beckman (1991)]:

$$I_{bh} = I_{sc}\left(1 + 0.033\cos\frac{360D}{365}\right) K_{tb}\sin\alpha \tag{4.1}$$

in which, I_{sc} = average value of the amount of solar energy received by a surface of unit area placed normal to the sun rays at the outer limit of the atmosphere (known as solar constant). This value is estimated as 1367 W/m^2 (Iqbal, 1983),

D = day of the year,

K_{tb} = beam transmittance coefficient accounting for attenuation of solar radiation by the atmosphere and can be determined by [Dilger and Ghali (1980)]:

$$K_{tb} = 0.9^{\frac{K_a t_u}{\sin(\alpha+5)}} \tag{4.2}$$

where k_a is the relative atmospheric pressure; t_u is a turbidity factor used to account for the haze condition of the atmosphere; and α is the solar altitude. Typical values of relative atmospheric pressure and turbidity factor are given in Table 4.2 and Figure 4.4, respectively.

The diffusive component is composed of directional diffuse resulting from forward scattering of direct solar radiation, plus non-directional diffuse which is uniformly distributed across the sky. Similar to direct radiation [Equation (4.1)], the diffuse radiation incident upon a horizontal surface I_{dh}, is given by:

$$I_{dh} = I_{sc}\left(1 + 0.033\cos\frac{360D}{365}\right) K_{td}\sin\alpha \tag{4.3}$$

where K_{td} = diffuse transmittance coefficient which can be determined from

the empirical formula suggested by Liu and Jordan (1960) as follows:

$$K_{td} = 0.271 - 0.294K_{tb} \tag{4.4}$$

The reflected radiation is the sum of the parts of the direct and diffuse radiation reflected by objects surrounding the bridge structure. The ratio of the reflected radiation to the original radiation incident on the surroundings is known as the albedo ρ_d. Table 4.3 shows typical values of the albedo for different surrounding objects.

The total solar radiation incident on any surface with a slope β to the horizontal is the sum of the three components described above:

$$I = (I_{bh} + A_i I_{dh}) \frac{\cos\theta}{\sin\alpha} + I_{dh}(1 - A_i)\left(\frac{1 + \cos\beta}{2}\right) + (I_{bh} + I_{dh})\rho_d\left(\frac{1 - \cos\beta}{2}\right) \tag{4.5}$$

where, A_i = coefficient representing the ratio of the directional diffuse to the total diffuse radiation, calculated as the ratio between the direct beam radiation and the solar constant, both incident upon a horizontal surface [Duffie and Beckman (1991)].

θ = incidence angle, the angle between the incoming sun rays and the normal to the surface, described in terms of angles defining the position of the sun relative to an observer on the earth and the orientation of the surface relative to the surface of the earth (see Figure 4.5).

$$\begin{aligned}\cos\theta = {} & \sin\delta\sin\varphi\cos\beta - \sin\delta\cos\varphi\sin\beta\cos\gamma + \cos\delta\cos\varphi\cos\beta\cos\omega + \\ & \cos\delta\sin\varphi\sin\beta\cos\gamma\cos\omega + \cos\delta\sin\beta\sin\gamma\sin\omega\end{aligned} \tag{4.6}$$

Table 4.1: Expression for Convection Coefficient, h_c, Kehlbeck (1975)

Geometry of the cross-section	Convection Coefficient h_c
Top surface of the bridge deck	$3.83w + 4.67$
Soffit and underside of cantilevers	$3.83w + 2.17$
Outer surface of webs	$3.83w + 3.67$
Inside surface of box	3.5

Table 4.2: Relative Atmospheric Pressure, k_a, at different Altitudes, Kehlbeck (1975)

Altitude Above Sea Level (m.)	Relative Atmospheric Pressure, k_a
0	1.0
500	0.94
1000	0.89
1500	0.84
2000	0.79
2500	0.74
3000	0.69

Table 4.3: Albedo for Different Surrounding Surface, Afedes (1974)

Surrounding Surface	Albedo, ρ_a
Fresh snow	0.8 - 0.9
Old snow	0.6 - 0.7
Calm water surface	0.05 - 0.18
Concrete	0.17 - 0.27
Sand	0.15 - 0.45
Sea and Ocean	0.05 - 0.12

in which, δ = solar declination, that is, the angular position of the sun with respect to the plane of the equator ($-23.45° \le \delta \le 23.45°$).

$$\delta = 23.45 \sin\left(360\frac{284+D}{365}\right) \tag{4.7}$$

φ = latitude of the location north or south of the equator, north positive ($-90° \le \varphi \le 90°$).

β = slope of the surface (i.e. the angle between the plane of the surface considered and the horizontal); $0 \le \beta \le 180°$, with $\beta > 90°$ for surfaces which have a downward facing component.

γ = surface azimuth angle, that is, the angle between the projection of the normal to the surface on a horizontal plane and the local meridian, with the zero point being due south, east negative and west positive ($-180° \le \gamma \le 180°$).

ω = hour angle, which is the angular displacement of the sun east or west of the local meridian, due to the rotation of the earth on its axis at 15° per hour. Solar noon being zero, morning negative, and afternoon positive; $\omega = 15\ (ST - 12)$, where ST is the solar time at any instant of the observer location.

In *FETAB3D*, Equation (4.5) is applied to all outer surfaces of the bridge structure except that the first term of the equation is equal to zero on the areas not exposed to direct sunlight (e.g. the bottom surface of the box girder). Furthermore, Equations (3.3) and hence (4.1) to (4.7), are applicable only during the daylight hours, that is, the hours between sunrise and sunset. The solar time t_{sr} at sunrise is given by:

$$t_{sr} = 12 - \frac{1}{15}\cos^{-1}(-\tan\delta\tan\varphi) \tag{4.8}$$

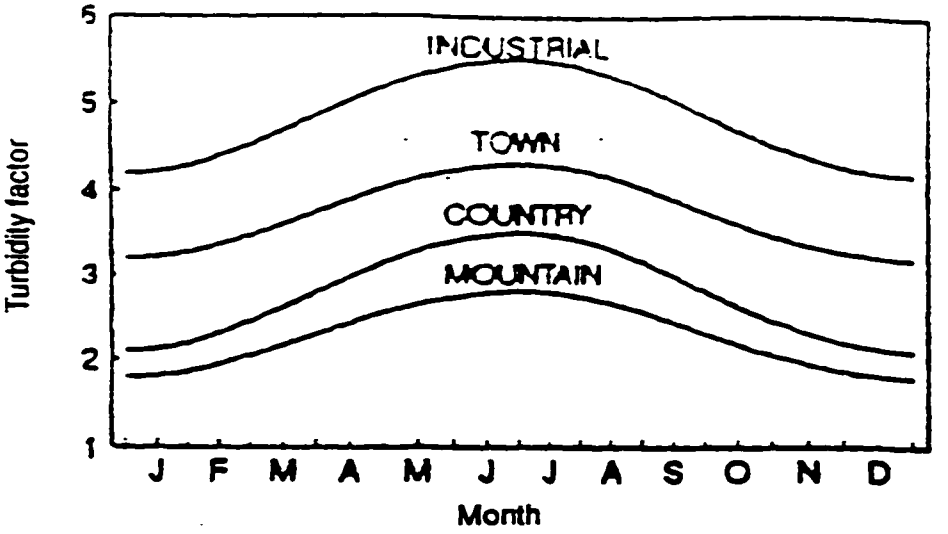

Figure 4.4 Values of turbidity factor for different locations throughout the year Moelsini and Massicotte (1993)

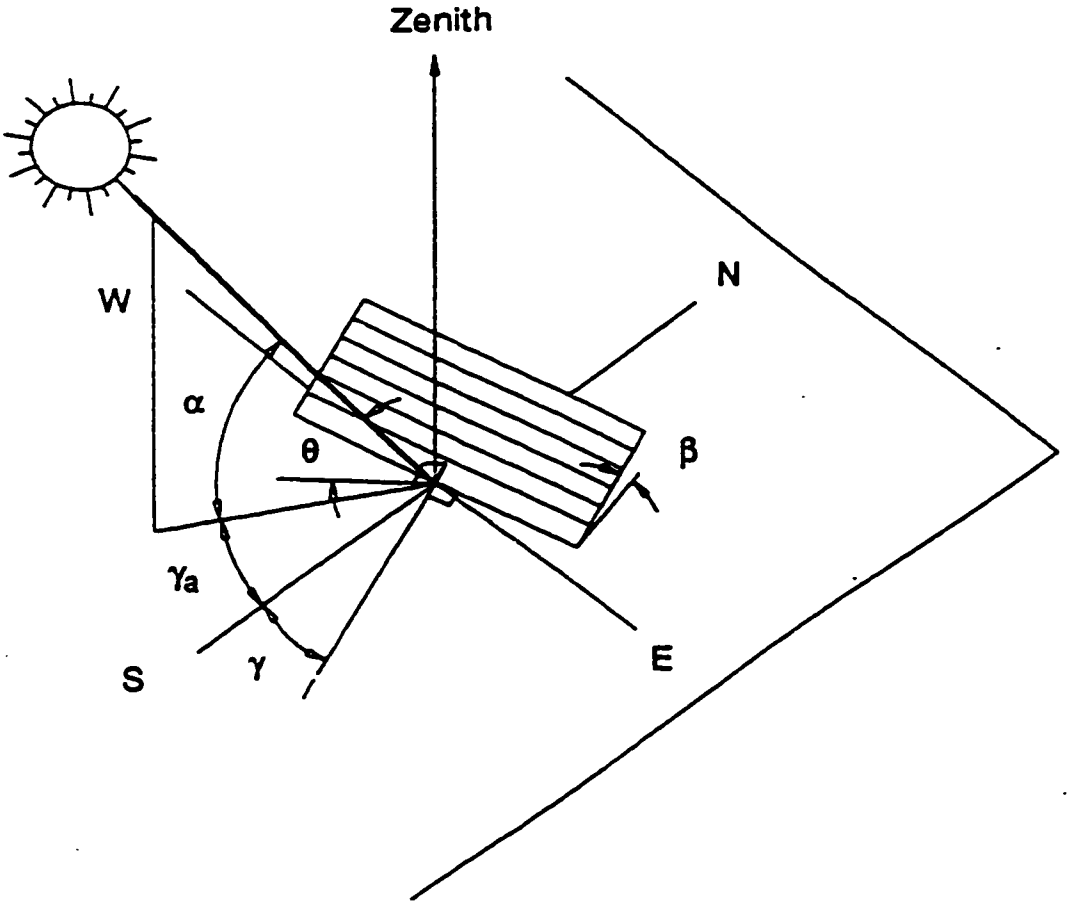

Figure 4.5 Geometry defining incidence angle of solar radiation

Similarly, the solar time t_{ss} at sunset is given as:

$$t_{ss} = 12 + \frac{1}{15}\cos^{-1}(-\tan\delta\tan\varphi) \tag{4.9}$$

It should be noted that the solar time *ST* doesn't necessarily coincide with the standard local time *SLT* of the location of the structure considered. Therefore, it is necessary to convert the standard local time to its corresponding solar time in order to apply the sun - angle Equations (4.6-7). The difference between solar and standard local time can be computed as [Duffie and Beckman (1991)]:

$$ST - SLT = 4(L_{st} - L_{loc}) + ET \tag{4.10}$$

in which, L_{st} = the standard meridian for the local time zone, (e.g. the eastern time zone in North America has standard meridian of 75°),

L_{loc} = the longitude of the location of the structure,

ET = equation of time which is a function of the day of the year D, and can be given in minutes as:

$$ET = 229.2\Big[(0.000075 + 0.001868\cos(\frac{360(D-1)}{365}) - 0.032077\sin(\frac{360(D-1)}{365}) - 0.014615\cos(\frac{720(D-1)}{365}) - 0.04089\sin(\frac{720(D-1)}{365})\Big] \tag{4.11}$$

FETAB3D assumes that the time at the start of the analysis is a standard local time; thus, it calculates the equivalent solar time to apply in the above equations. The output of analysis is also printed at standard local time. This feature is important when comparing the output

of the program with field measurements since the difference between the solar time and local standard time can be up to 1 hour [Duffie and Beckman (1991)].

For box girder bridges with overhangs, the first term in Equation (4.5) does not apply on the part of the web shaded by the cantilever slab. The height of this shaded part, l_{sh}, (see Figure 4.1) is given by Dilger et al. (1983) and Elbadry and Ghali (1983a) as: :

$$l_{sh} = l_c \frac{\tan\alpha}{\sin(90+\gamma-\gamma_a)\sin\beta - \cos\beta\tan\alpha} \tag{4.12}$$

where, l_c is the length of the cantilever slab, and γ_a is the azimuth angle of the sun given by [Krieth and Kreider (1978)]:

$$\gamma_a = \sin^{-1}\left(\frac{\cos\delta\sin\omega}{\cos\alpha}\right) \tag{4.13}$$

It should be mentioned here that some researchers, such as Dilger et al. (1983), Elbadry and Ghali (1983a), Mirambell and Aguado (1989) and Fu, Ng and Cheung (1990), in their analysis for prediction of temperature variations in bridge structures due to environmental conditions, considered only the effects of direct solar radiation [Equations (4.1) and (4.2)]. Others, such as Hirst and Dilger (1989) and Molesini and Massicotte (1993) considered the three components of solar radiation and modified the original program *FETAB* [Elbadry and Ghali (1982)] with solar model similar to that described above.

4.3.2 Diurnal Variation of Ambient Air Temperature

The diurnal variation of ambient air temperature can be simply assumed to follow a sinusoidal cycle between the minimum air temperature $T_{a,\,min}$, and the maximum air temperature $T_{a,\,max}$. This simplification was introduced by Hulsey (1976) with the assumption that the minimum air temperature occurs at 3:00 a.m., and the maximum air temperature occurs at 3:00 p.m. The ambient air temperature at time t is given as:

$$T_a(t) = A \sin \frac{2\pi (t-9)}{24} + B \tag{4.14}$$

where $T_a(t)$ = air temperature at time t,

A = one-half the daily range of air temperature,

$$= \frac{1}{2}(T_{a,\,max} - T_{a,\,min}) \tag{4.15}$$

B = average daily temperature.

$$= \frac{1}{2}(T_{a,\,max} + T_{a,\,min}) \tag{4.16}$$

Many researchers have used this simplification to obtain the air temperature at any time of the day. The above equations were adopted by Dilger et al. (1983) and Elbadry and Ghali (1983a) and were implemented in program FETAB. Molesini and Massicotte (1993) also compared the air temperature calculated from Equation (4.14) with meteorological data obtained for the Montréal area and found good agreement.

4.3.3 Air Temperature Inside a Box Girder

For the still air inside the box section, the air temperature is dependant on the temperature field of the interior surface of the box at any particular time. Dilger et al. (1983) considered the energy balance between the interior surface of the box and the air enclosed inside the box to obtain the following equation:

$$\int_0^{A_b} (h_c + h_r)\,[T_s - T_b]\,dA_b = \rho_a c_a V_b \frac{dT_b}{dt} \tag{4.17}$$

in which T_s = temperature of the inside surface of the box at time t,

T_b = air temperature inside the box,

A_b = area of the inner surface of the box,

ρ_a = density of the air (1.228 kg/m^3),

c_a = specific heat of the air (716 J/kg °C),

and, V_b = volume of the air inside the box.

Elbadry (1982) rewrote the previous equation in a finite element form and made it suitable for computer implementation as follows:

$$\rho_a c_a V_b \frac{dT_b(t)}{dt} + T_b(t) \sum_e^{n_b} h^e(t)\, A_b^e = \sum_e^{n_b} h^e(t)\, T_s^e(t)\, A_b^e \tag{4.18}$$

in which $h^e(t)$ = average value of the over-all heat transfer coefficient for a boundary surface element e inside the box at time t,

$T_s^e(t)$ = average value of the surface temperature for a boundary surface element e inside the box at time t,

A_b^e = area of the boundary surface element e inside the box,

n_b = number of boundary surface elements inside the box.

Grouping the terms and rewriting the previous equation yields the following:

$$C \frac{dT_b(t)}{dt} + H(t)\, T_b(t) = F(t) \tag{4.19}$$

in which

$$C = \rho_a c_a V_b \quad , \tag{4.20}$$

$$H(t) = \sum_{e}^{n_b} h^e(t) A_b^e \quad , \tag{4.21}$$

and

$$F(t) = \sum_{e}^{n_b} h^e(t) T_s^e(t) A_b^e \quad . \tag{4.22}$$

Equation (4.19) is of the same form as Equation (3.26); thus, Galerkin's weighted residual method can be applied to give the following recurrence equation:

$$(\frac{1}{\Delta t} C + \frac{2}{3} H_{n+1}) T_{b,n+1} = (\frac{1}{\Delta t} C + \frac{1}{3} H_n) T_{b,n} + \frac{2}{3} F(t)_{n+1} + \frac{1}{3} F(t)_n \tag{4.23}$$

Equation (4.23) is implemented in *FETAB3D* to find the unknown air temperature inside the box at the end of the n^{th} time increment (i.e. $T_{b,n+1}$).

Figure 4.6 depicts a flow chart of the computer program *FETAB3D* and describes the sequence in which the analysis is performed to determine the temperature and stress distributions at each timestep. The program listing, input data instructions, and description of the computer output are provided in the reference manual [Ibrahim et al. (1995)].

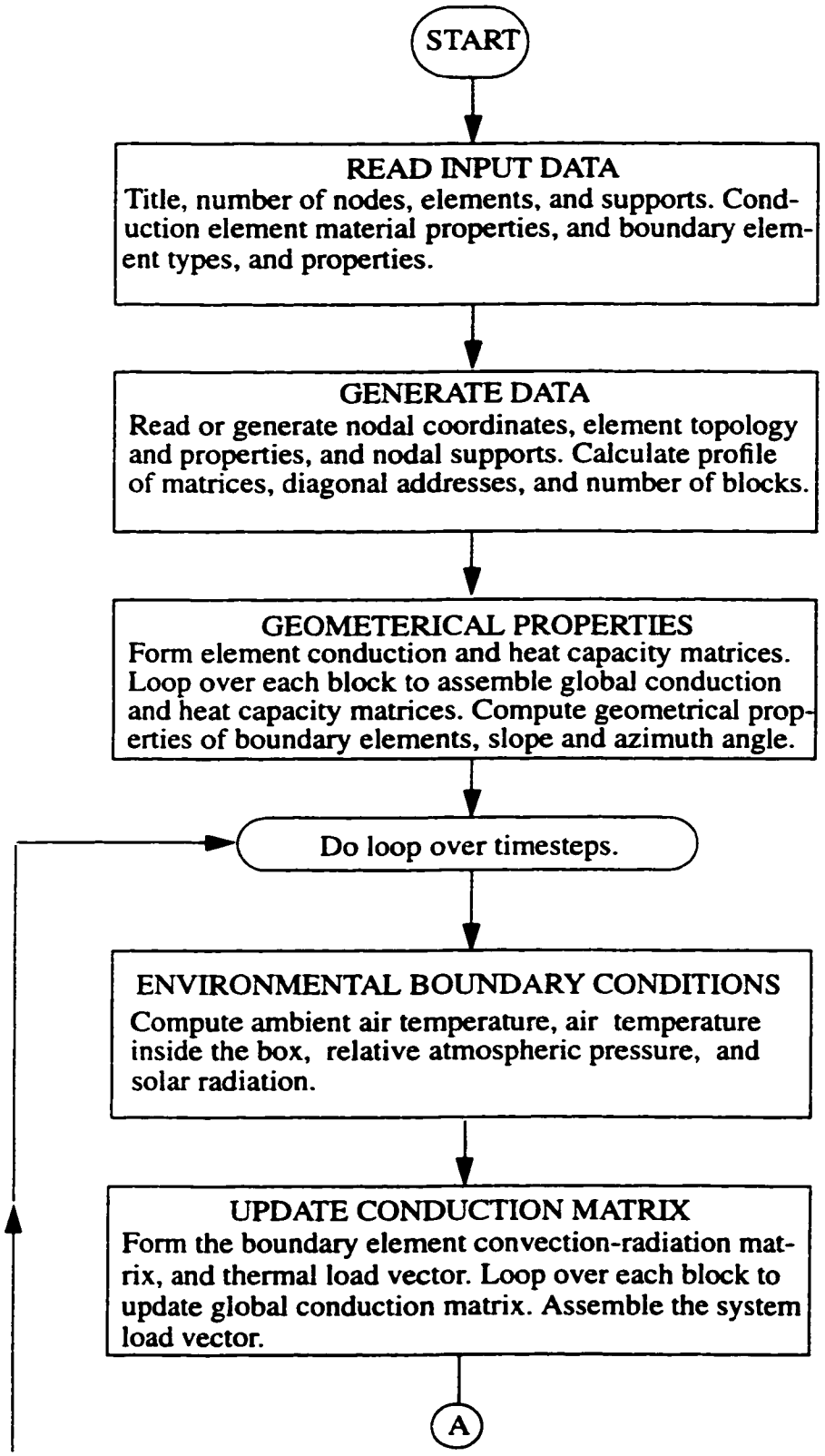
START
READ INPUT DATA
Title, number of nodes, elements, and supports. Conduction element material properties, and boundary element types, and properties.
GENERATE DATA
Read or generate nodal coordinates, element topology and properties, and nodal supports. Calculate profile of matrices, diagonal addresses, and number of blocks.
GEOMETERICAL PROPERTIES
Form element conduction and heat capacity matrices. Loop over each block to assemble global conduction and heat capacity matrices. Compute geometrical properties of boundary elements, slope and azimuth angle.
Do loop over timesteps.
ENVIRONMENTAL BOUNDARY CONDITIONS
Compute ambient air temperature, air temperature inside the box, relative atmospheric pressure, and solar radiation.
UPDATE CONDUCTION MATRIX
Form the boundary element convection-radiation matrix, and thermal load vector. Loop over each block to update global conduction matrix. Assemble the system load vector.
A

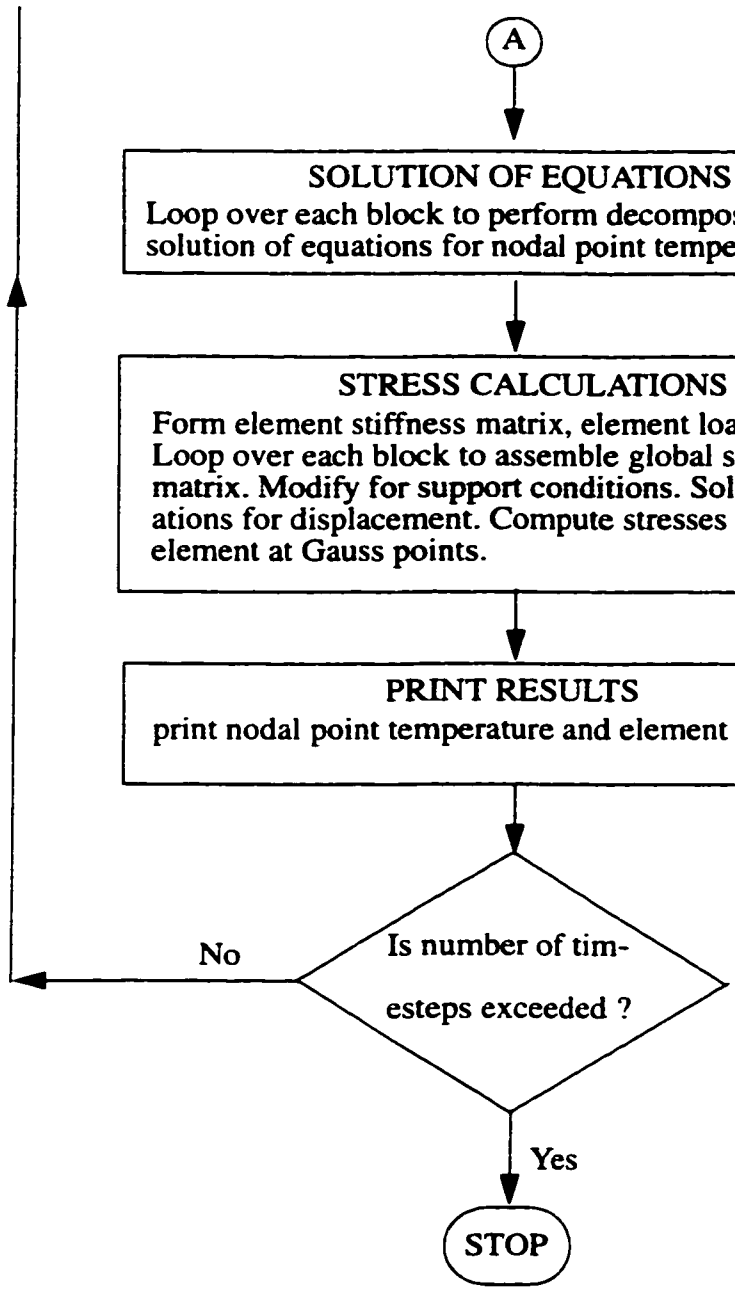

Figure 4. 6 Flow chart for computer program *FETAB3D* for temperature and stress analysis of box girder bridges

4.4 Verification Problems

In order to demonstrate the validity of the numerical model adopted and to verify the computer program developed herein, a number of verification problems are analyzed and the results are compared to either exact solutions or to those obtained from other well known finite element computer programs. The verification problems are chosen to reflect the ability of the program to:

- model heat flow for various types of ambient boundary conditions, such as heat flux and convection conditions, and to accurately compute the resulting temperature variations with time.
- predict thermal stresses induced in curved structures due to nonuniform temperature distributions and restraint conditions.

Further verification of the ability of the program to predict temperature variations produced in actual bridge structures by climatological conditions will be discussed later in Section 5.4 where a comparison with field measurement is presented.

In the heat flow verification problems presented below, the material is chosen to be homogeneous with constant thermal conductivity k of unit value, the specific heat c, and the density ρ are also equal to unity, unless otherwise noted. Also, all problems are dimensionless unless otherwise noted.

4.4.1 Problem 1: A Semi-Infinite Solid Subjected to Constant Heat Flux q.

A semi-infinite solid (Figure 4.7) is subjected to an essentially one dimensional heat flux of unit value per unit area of the surface. It has an initial temperature of zero degrees. The temperature of the solid at depth z from the surface at time t [i.e. $T(z,t)$], is given by Carslaw and Jaeger (1959) as:

$$T(z,t) = 2\left(\sqrt{\frac{t}{\pi}}exp\,(-\frac{z^2}{4t}) - \frac{z}{2}\left[1 - erf(\frac{z}{2\sqrt{t}})\right]\right) \tag{4.24}$$

where $erf(\frac{z}{2\sqrt{t}})$ is a probability function called "error function" and is defined as:

$$erf(z) = \frac{2}{\sqrt{\pi}}\int_0^z exp\,(-t^2)\,dt \tag{4.25}$$

In *FETAB3D*, a finite element mesh composed of 20 conduction elements and one boundary surface element with total depth equal to 4 units of length is used to perform a transient analysis for a period of 1 unit of time. The time interval Δt is chosen to be 0.1 time unit to insure stable and non-oscillatory solution [Elbadry (1982)].

Comparison between the exact temperature distribution along the depth z up to 2 units of length and the distribution obtained from *FETAB3D* at time $t = 1.0$ is shown in Figure 4.7. The agreement between the results reflects the ability of the program to model a three-dimensional body subjected to a simple type of boundary condition.

4.4.2 Problem 2: A Semi-Infinite Solid Subjected to Periodic Surface Convection

Carslaw and Jaeger (1959) gave a closed form solution to predict the temperature variations within a semi-infinite solid subjected to a periodic convection boundary, $T_a(t) = A\sin(\omega t - \zeta)$, at the surface with zero initial temperature of the solid [i.e. $T(z,t) = 0°$].

The temperature variation is composed of a transient and a quasi-steady term. Since the transient term dies out after a certain time from the start of the analysis, we consider here

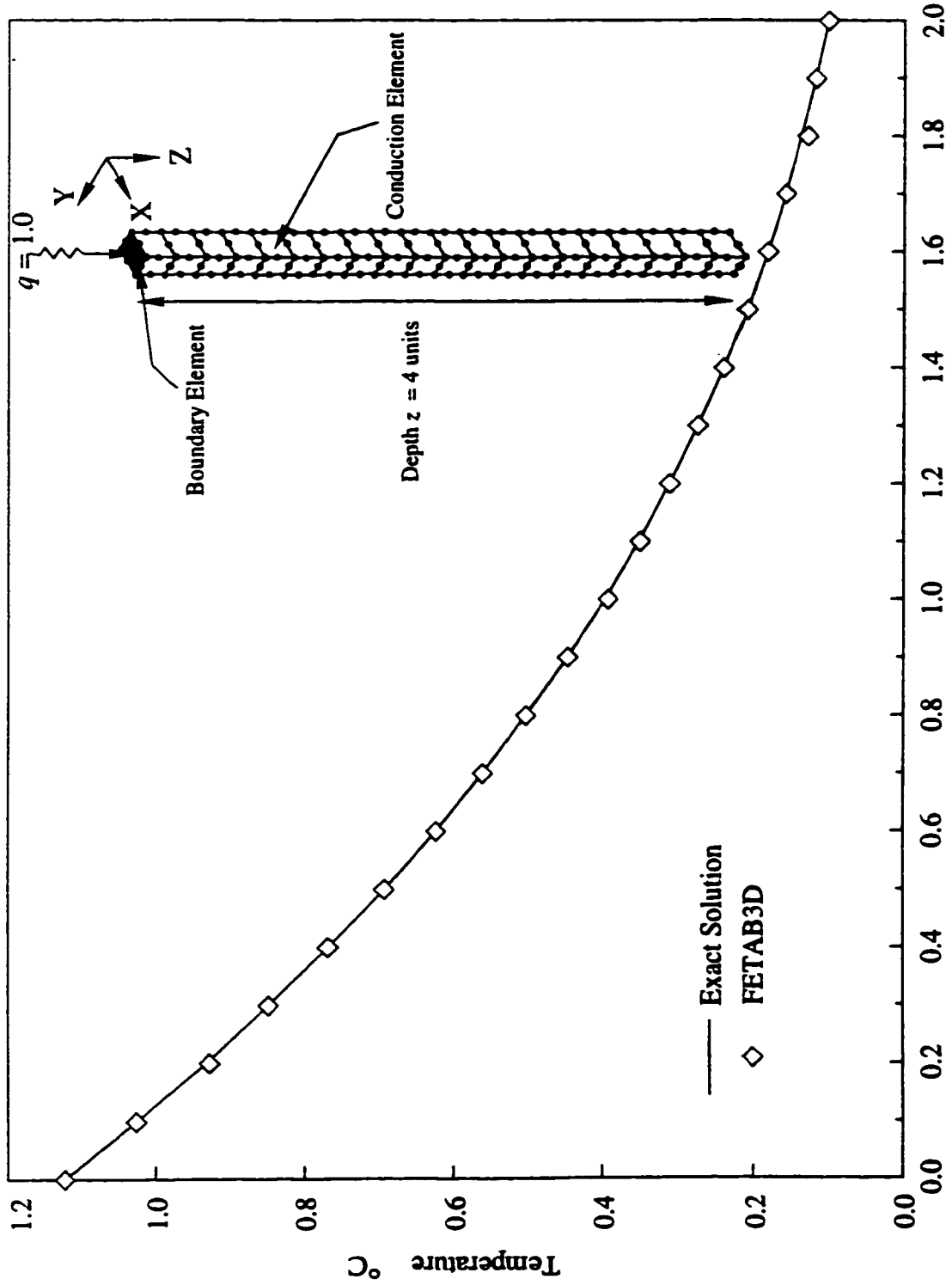

Figure 4.7 Semi-infinite solid subjected to a unit flux at the surface; temperature distribution along the depth at time $t = 1.0$.

only the quasi-steady term which is given as:

$$T(z,t) = \frac{A\exp\left(-z\sqrt{\frac{\omega\rho c}{2k}}\right)}{\sqrt{1+\frac{2k}{h_c}\sqrt{\frac{\omega\rho c}{2k}}+\frac{k}{h_c^2}(\omega\rho c)}}\sin\left(\omega t - z\sqrt{\frac{\omega\rho c}{2k}} - \tan\frac{1}{1+\sqrt{\frac{2h_c^2}{k\omega\rho c}}}\right) \qquad (4.26)$$

For $\omega = \frac{2\pi}{24}$, $\zeta = 0$, $A = 100°$, $k = \rho = c = h_c = 1$, the exact solution becomes:

$$T(z,t) = \frac{100\exp\left(-z\sqrt{\frac{\pi}{24}}\right)}{\sqrt{1+2\sqrt{\frac{\pi}{24}}+\frac{\pi}{12}}}\sin\left(\frac{\pi t}{12} - z\sqrt{\frac{\pi}{24}} - \tan\frac{1}{1+\sqrt{\frac{24}{\pi}}}\right) \qquad (4.27)$$

The finite element mesh used to solve this problem is the same as that shown in Figure 4.7 of the first problem. A transient analysis is performed for 72 time units to ensure that the steady state is reached [Elbadry (1982)], with a time interval Δt equals to 0.1 time unit. A comparison is made between the closed form solution and the solution obtained by *FETAB3D* for $48 \le t \le 72$ in Figure 4.8.

This example shows the capability of the program to predict the effects of time-varying convection boundary conditions acting at the surface of a structure.

4.4.3 Problem 3: A Finite Solid Subjected to Periodic Surface Heat Flux

For a finite solid of thickness L (Figure 4.9) subjected to periodic heat flux at the surface , $q(0, t) = A\sin\omega t$, and zero initial temperature , $T(z,0) = 0°$, the exact solution was derived by Hulsey (1976) as:

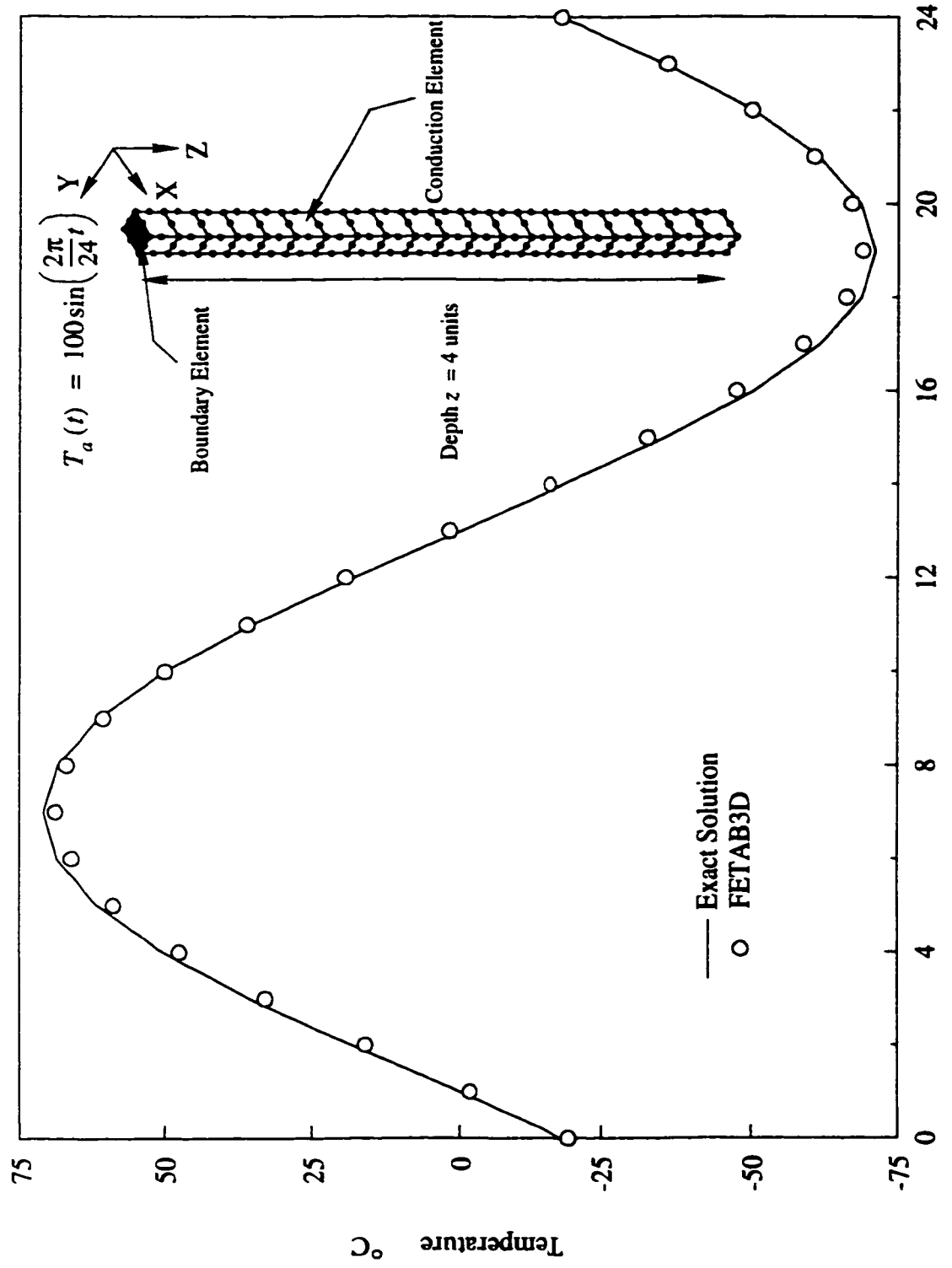

Figure 4.8 Semi-infinite solid subjected to periodic surface convection; variation of surface temperature with time.

$$T(z,t) = A\left(\frac{z^2}{2kL} - \frac{z}{k} + \frac{L}{3k} + \frac{t}{\rho cL}\right)\sin\omega t + \frac{A}{\rho cL}\left(-t\sin\omega t - \frac{1}{\omega}\cos\omega t + \frac{1}{\omega}\right)$$
$$+ \sum_{n=1}^{\infty}\left(\frac{2A\omega}{kL\lambda_n^2}\cos\lambda_n z\right)\frac{\frac{\lambda_n^2 k}{\rho c}\cos\omega t + \omega\sin\omega t - \frac{\lambda_n^2 k}{\rho c}exp\left(-\frac{\lambda_n^2 k}{\rho c}t\right)}{(\lambda_n^4 + \omega^2)} \qquad (4.28)$$

where $\lambda_n = \frac{n\pi}{L}$

For $\omega = \frac{2\pi}{24}$, $L = 2$, $A = 1$, $k = \rho = c = 1$, the exact solution becomes:

$$T(z,t) = \left(\frac{z^2}{4} - z + \frac{2}{3} + \frac{t}{2}\right)\sin\frac{\pi t}{12} + \frac{1}{2}\left(-t\sin\frac{\pi t}{12} - \frac{12}{\pi}\cos\frac{\pi t}{12} + \frac{12}{\pi}\right)$$
$$+ \sum_{n=1}^{\infty}\left(\frac{\pi}{12\lambda_n^2}\cos\lambda_n z\right)\frac{\lambda_n^2\cos\frac{\pi t}{12} + \frac{\pi}{12}\sin\frac{\pi t}{12} - \lambda_n^2 exp(-\lambda_n^2 t)}{\left(\lambda_n^4 + \left(\frac{\pi}{12}\right)^2\right)} \qquad (4.29)$$

A finite element mesh composed of 5 conduction elements and one boundary element at the surface (Figure 4.9) is used to compute the temperature distribution. A comparison between the analytical solution and the solution obtained using *FETAB3D* for $48 \le t \le 72$ and $\Delta t = 0.1$ time unit, is shown in Figure 4.9

This problem simulates the heat gained by the surface of a bridge due to the incident sun rays which have variable intensity with time.

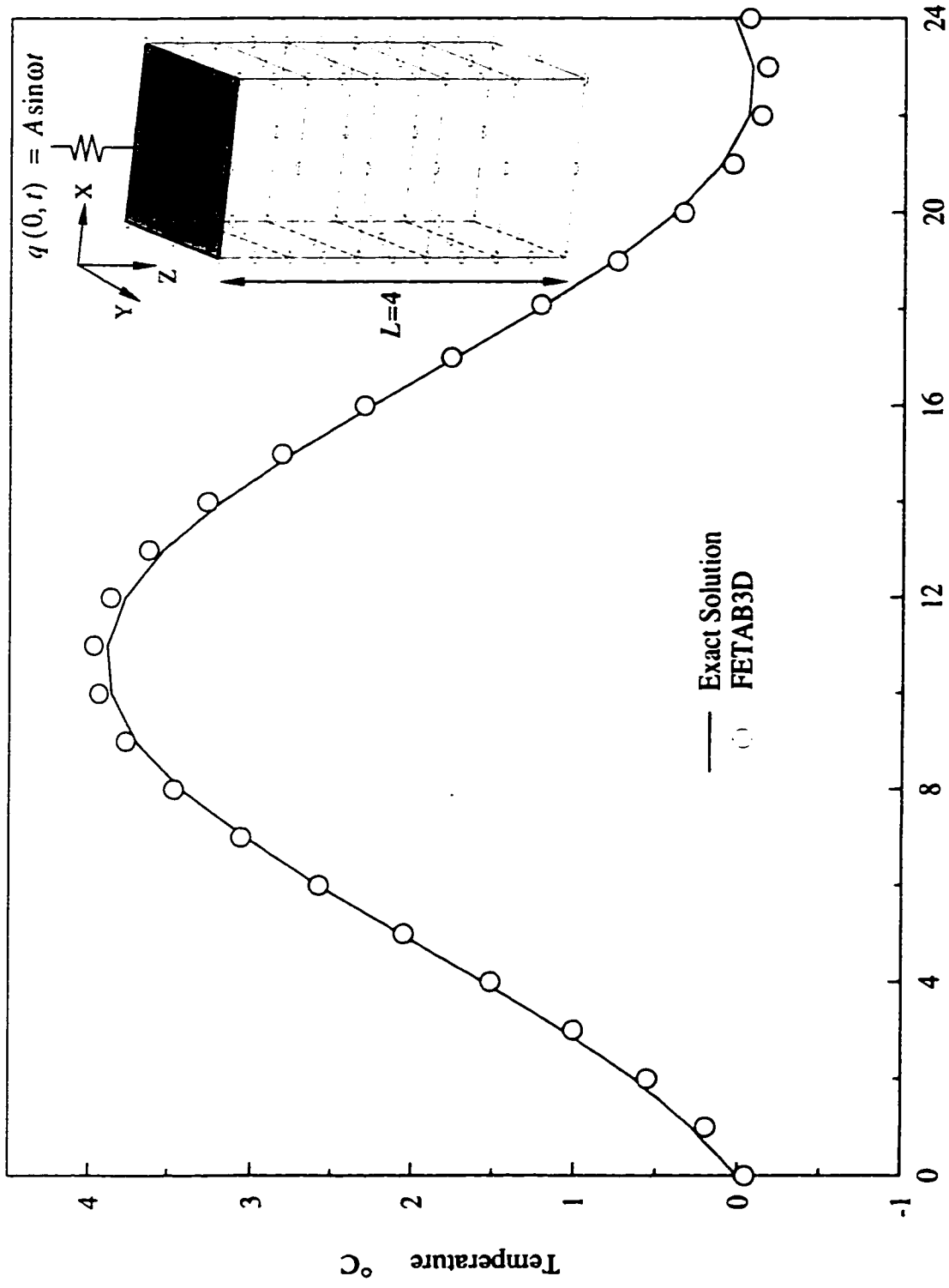

Figure 4.9 Finite solid subjected to periodic surface heat flux; variation of surface temperature with time.

4.4.4 Problem 4: A Curved Finite Solid Subjected to Constant Heat Flux q

A finite solid of curved geometry (shown in Figure 4.10) is subjected to constant heat flux q = 100 W/m^2 at the top surface. A finite element mesh composed of 4 conduction elements and 2 boundary elements is used to predict the temperature distribution within the body. A comparison is made with the well known heat transfer program ADINA-T (1992). This program is capable of modelling constant values of boundary heat flux to calculate the temperature values at different time steps in the incremental transient analysis. Furthermore, to the author's knowledge, the university version of ADINA-T has an upper limit of 2000 nodes in the mesh, which may not be sufficient to fully model a complete structure.

The comparison shown in Figure 4.10 demonstrates that a good correlation exists between the two programs.

4.4.5 Problem 5: Stresses in a Curved beam due to a Nonuniform Temperature Distribution.

To insure that stresses calculated from *FETAB3D* are correct, a two-span continuous curved beam (Figure 4.11 a) is analyzed for the effects of a nonlinear temperature variation over the depth and the results are compared to those obtained from an analysis performed using the well established finite element program NISA (1991). The analysis is performed using E = 27.386x10^6 kN/m^2, α = 8x10^{-6}, and ν = 0.2. The total thermal stresses induced in the beam are computed in the global directions at the Gauss points (at the center of each element) and compared for both programs in Figure 4.11b.

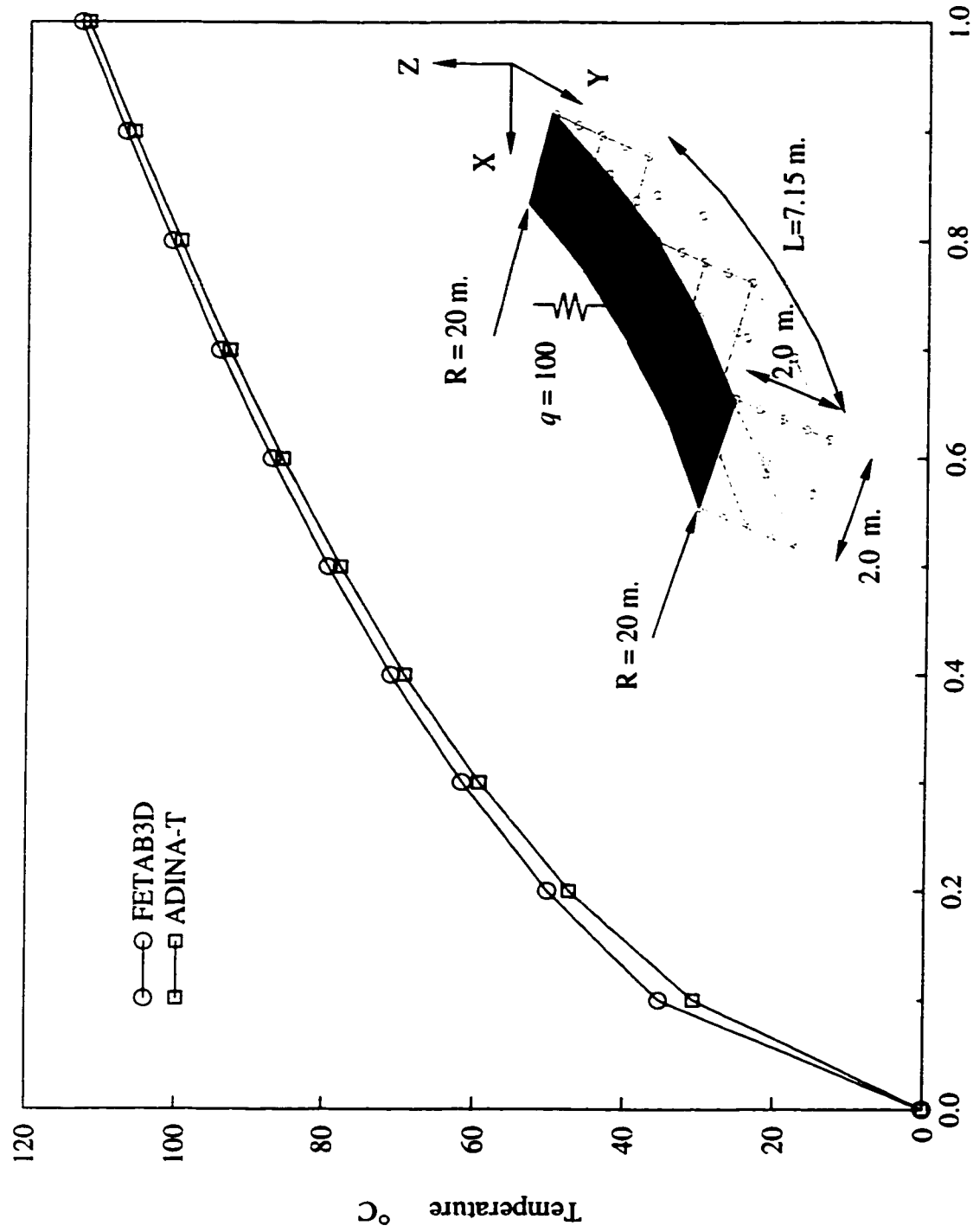

Figure 4.10 Curved finite solid subjected to constant heat flux variation of surface temperature with time

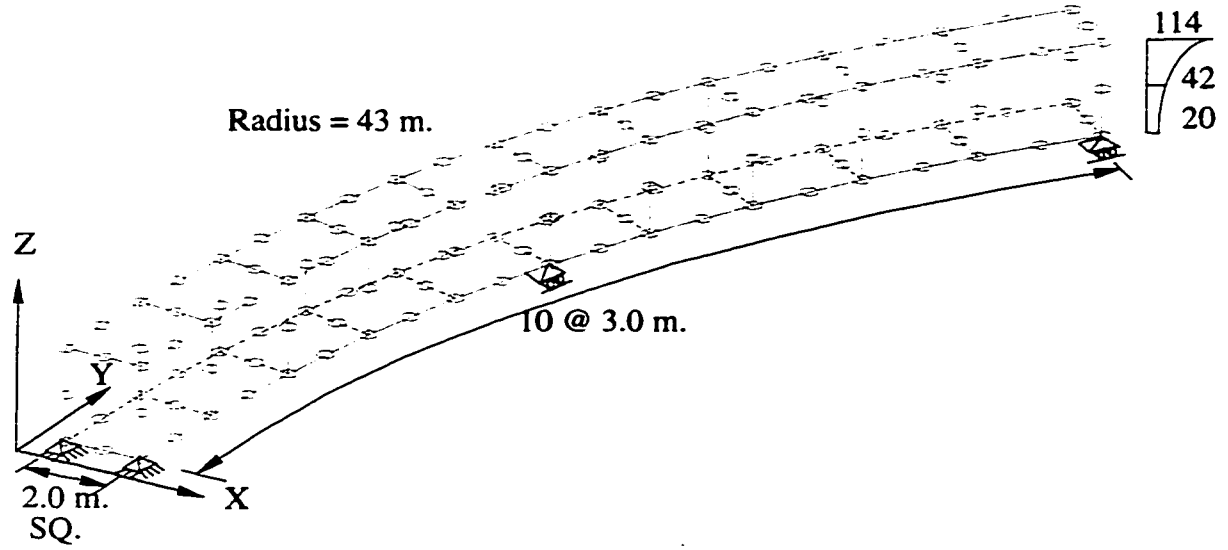

a) Curved beam subjected to nonlinear temperature distributions

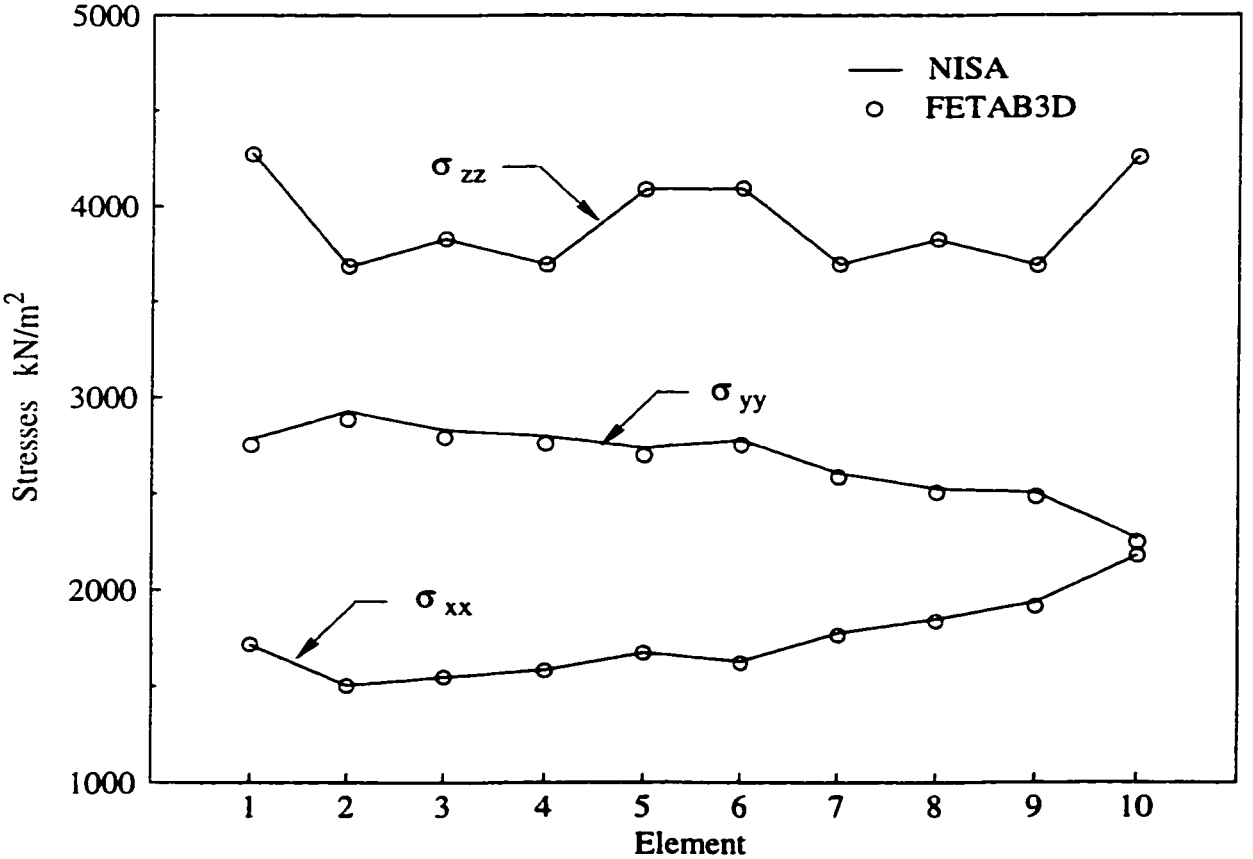

b) Stresses in global directions computed at central Gauss point of each element.

Figure 4.11 Comparison of thermal stresses obtained by NISA and FETAB3D in a two-span curved beam.

CHAPTER 5
APPLICATIONS

5.1 General

In curved bridges, the amount of solar radiation received by the bridge web surface differs from one section to another along the bridge length. This is due to the curvature of the bridge axis and hence the variation in the surface azimuth angle γ, (see Figure 5.1a). In this chapter, program *FETAB3D* is employed in a case study to analyze the three-dimensional temperature distribution in an existing curved concrete box girder bridge and to investigate the significance of the temperature variation along the bridge length. Furthermore, a parametric study is conducted in order to assess the importance of certain parameters on this temperature variations. In the following, the bridge configuration and material properties used in the study are described. The size of the finite element mesh used in the analysis is shown. Further verification of *FETAB3D* is made against field measurements taken by other researchers on an actual bridge located in Quebec. Results and conclusions of the case study as well as the parametric study are subsequently presented.

5.2 Bridge Specifications:

A four span curved concrete box girder bridge is chosen for the present investigation. Dimensions and geometry of the bridge are adopted, with some simplifications, from The Bow River Bridge located in Calgary, Alberta. These simplifications include, for example, the assumption of constant thicknesses of the top and bottom slabs and the webs forming the bridge cross-section. Such simplifications should not affect the results of the current study. A complete description of the bridge geometry and the data required for the analysis are given below:

- Dimensions and geometry:

  The bridge has a total length of 160 m with a mean radius of 115 m (at the lon-

gitudinal axis of the bridge). The bridge length is composed of four spans; each span evolves 20 degrees for a total of 80 degrees (i.e. $\psi = 80°$). The cross-section dimensions as well as a general isometric view are shown in Figure 5.1.

- Orientation of bridge axis:

  Since the bridge axis is curved, the bridge orientation and the surface azimuth angle, γ, vary from section to section along the bridge length. The orientation at any section is determined with respect to the global Y-axis which is chosen to coincide on the tangent to the bridge axis at the cross-section at the first end of the bridge. The orientation of the global Y-axis with respect to the North is used as a reference in order to determine the orientation of the bridge axis at any section. In this case study, the Y-axis is chosen parallel to the North direction (see Figure 5.1).

- Geographical and meteorological data:

  Location: Calgary, with latitude of 51.03° N and altitude of 1050 m above sea level. The longitude is 113.96° W, with standard meridian of 105° W.

  Day of the year: July 17= 198, considered as the hottest day of the year.

  The daily range of ambient air temperature is taken to be 20°C, with $T_{a,max}$ = 30° C, and $T_{a,min}$ = 10° C.

  The wind speed is assumed to be 1.0 m/s, with turbidity (haze) factor equal to 4.2, and the albedo of the surrounding is 0.18.

- Thermal and elastic material properties:

  The average values of the material properties used in the present investigation are adopted from Elbadry and Ghali (1983a), and are summarized in Table 5.1. The convection heat transfer coefficient h_c at various surfaces of the bridge is given in Table 5.2 and is based on the equation suggested by Kehlbeck 1975 (see Table 4.1).

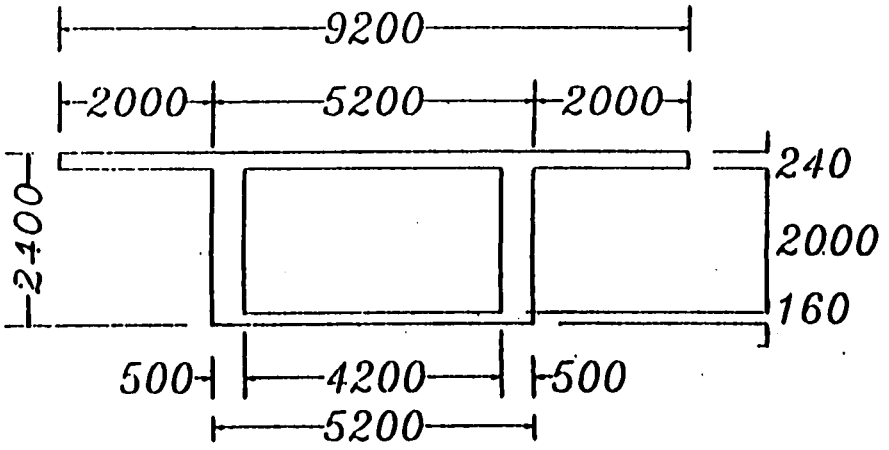

b) Cross section dimensions

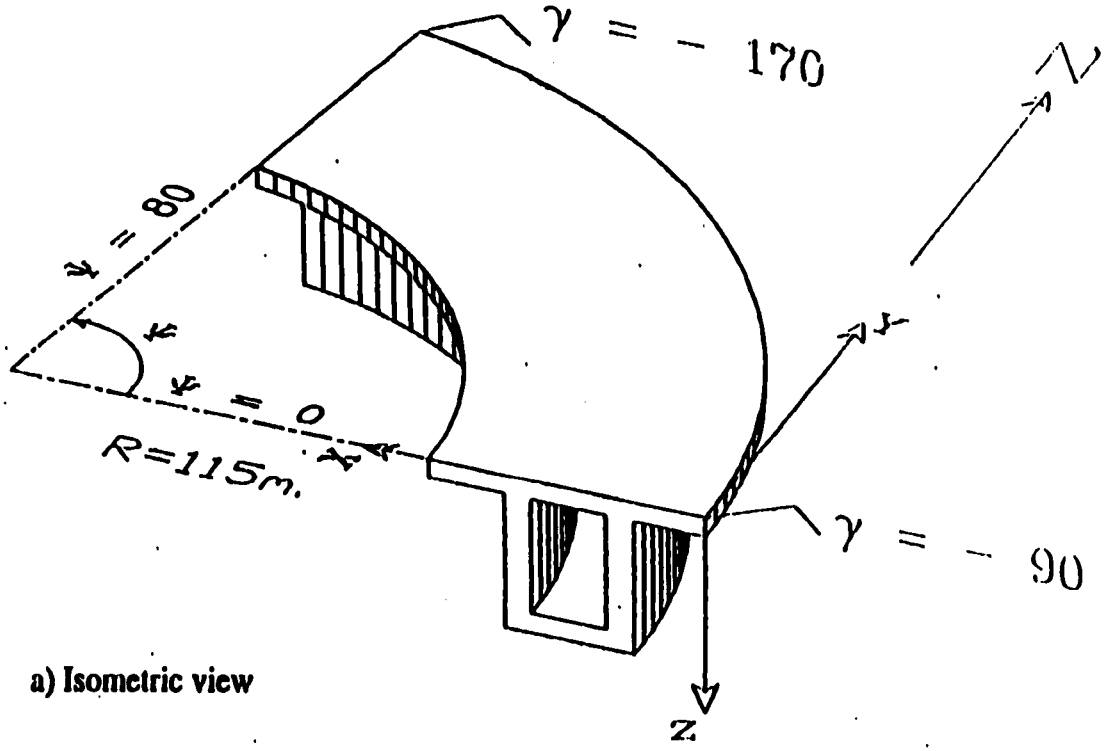

a) Isometric view

Figure 5.1 Orientation, geometry and cross-section dimensions of the bridge for case study.

Table 5.1: Thermal and Elastic Properties of Concrete

Material Property	Concrete
Solar absorption coefficient, *a*	0.5
Emissivity, *e*	0.88
Density, ρ, kg/m^3	2400.0
Specific heat, *c*, J/(kg. °C)	960.0
Coefficient of thermal expansion, α, °C^{-1}	8x10^{-6}
Thermal conductivity, *k*, W/(m. °C)	1.5
Modulus of elasticity, *E*, MPa	27386
Poission's ratio, ν	0.2

Table 5.2: Convection Coefficient h_c for Different Surfaces of the Bridge Geometry Calculated at Wind Speed of 1 m/s

Bridge Surface	Convection coefficient, h_c, W/(m^2. °C)
Top surface of concrete deck	8.5
Bottom surfaces of overhangs	6.0
Outer surfaces of the webs	7.5
Inside surface of the box girder	3.5*
Bottom surface of soffit slab	6.0

* This value is computed for zero wind speed.

Since the problem of predicting the temperature distribution of a bridge structure due to environmental conditions is always transient, the initial temperature at start of the analysis must be known for the recurrence Equation (3.38) to be solved. In the present analysis, the initial nodal temperature are assumed uniform throughout the bridge at a value equal to the ambient air temperature at the start of the analysis. The same cycle of environmental conditions over the day in question is repeated until more realistic initial temperature values are reached. In this study, a four-day analysis period was found sufficient to reach realistic initial temperatures at the start of the fourth day, and thus the results of temperature distribution are obtained from the fourth day. Figure 5.2 shows different vertical temperature distributions through the sunlit web of the bridge cross-section at the first end of the bridge (i.e. $\psi = 0.0$) for an analysis period of five days. As can be seen, the results at the fourth day of analysis are fairly close from steady state condition (i.e. fixed values of temperature under given loads at a given time).

In the analysis performed, the time increment was taken as 1.0 hour to maintain the stability and accuracy of the solution using the finite element method [Elbadry (1982)].

5.3 Mesh Size

In order to discretize the bridge described in the previous section into finite elements to study the distribution of temperature, one has to examine the influence of element size (i.e. the number of elements in the mesh) on the accuracy of the predicted temperatures.

To analyze the effect of element size on the results obtained, it was deemed simpler to study this effect at two different levels separately: the cross-sectional level and the bridge axis level.

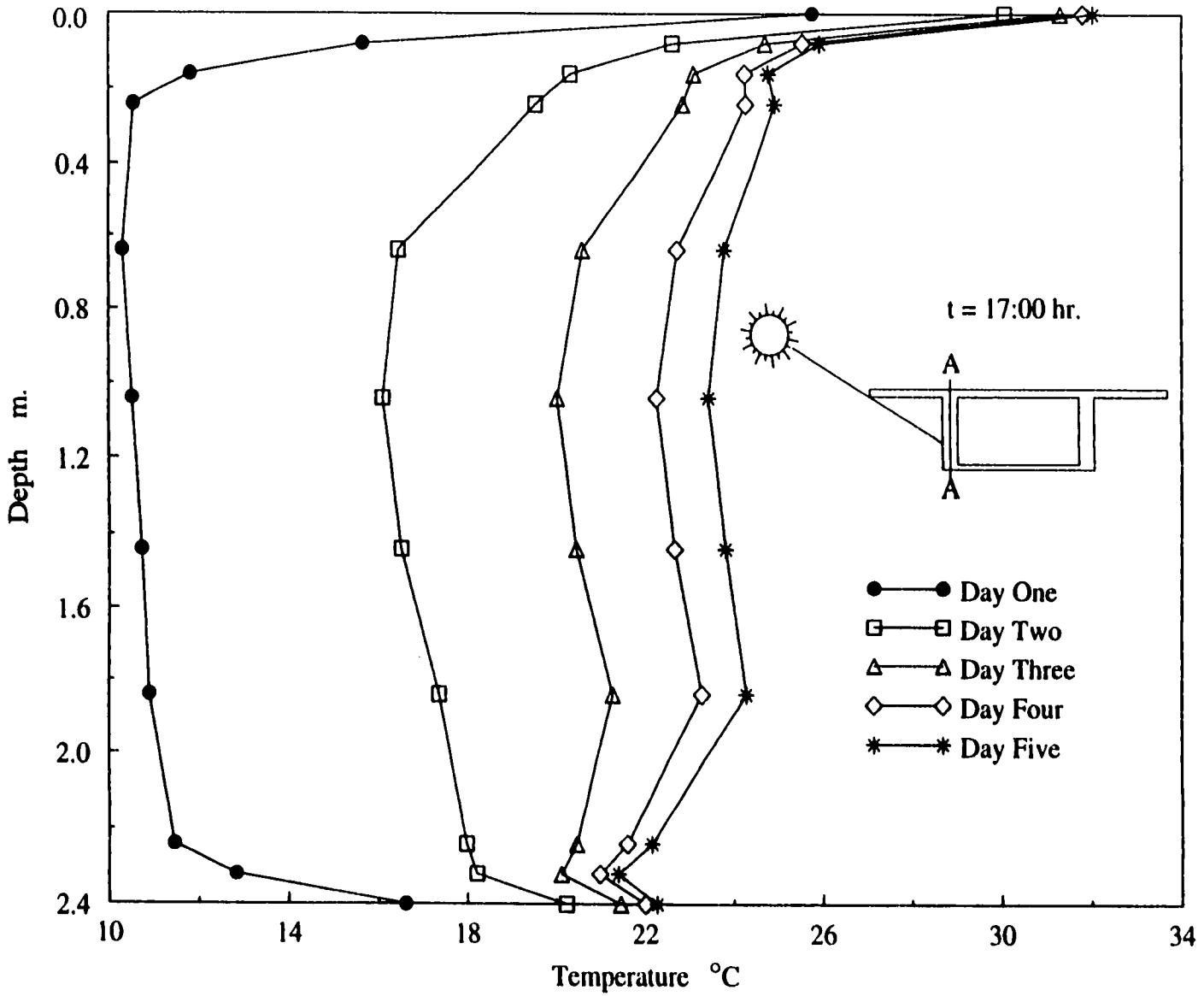

Figure 5.2 Comparison of vertical temperature distribution along the center line of the sunlit web for five consecutive days of same cycle of environmental conditions.

At the cross-sectional level, two finite element meshes (shown in Figure 5.3) are used to calculate the temperature distribution within the cross-section of the bridge. Mesh I (coarse mesh) consists of 1109 nodal points, 132 conduction elements, and 74 boundary elements, whereas Mesh II (fine mesh) is formed of 1703 nodal points, 204 conduction elements, and 110 boundary elements. In both meshes, each element has a length of 1 m in the longitudinal direction of the bridge. Figure 5.4 shows a comparison of the temperature distribution along the center line of the sunlit web for Meshes I and II, computed with a time increment $\Delta t = 1.0$ hour. The comparison shows that Mesh I is sufficiently accurate for the present investigation.

Based on the previous comparison, Mesh I is extended to evolve along the length of the bridge up to 8 degrees (i.e. $\psi = 8°$). This portion of the bridge is subsequently subdivided into either 1, 2, or 4 elements along the axis of the bridge. A comparison between the results obtained for the longitudinal variation of temperature at a point at depth 2.24 m on the surface of the sunlit web for the three different cases is shown in Figure 5.5. This comparison indicates that discretization along the bridge length can be accurately done using one element every eight degrees. Thus, the overall discretization of the bridge is composed of Mesh I at the cross-sectional level, and 10 segments along the longitudinal axis of the bridge, each of 8 degrees long. The whole mesh, therefore, consists of 6860 nodes, 1320 conduction elements, and 740 boundary elements.

5.4 Comparison with Field Measurements

In order to demonstrate the ability of *FETAB3D* to predict temperature variations in actual bridge structures due to environmental conditions, a comparison is made in this Section between temperature values calculated by the program and those obtained from field measurements by Massicotte et al. (1994) on the Grand-Mère box girder bridge

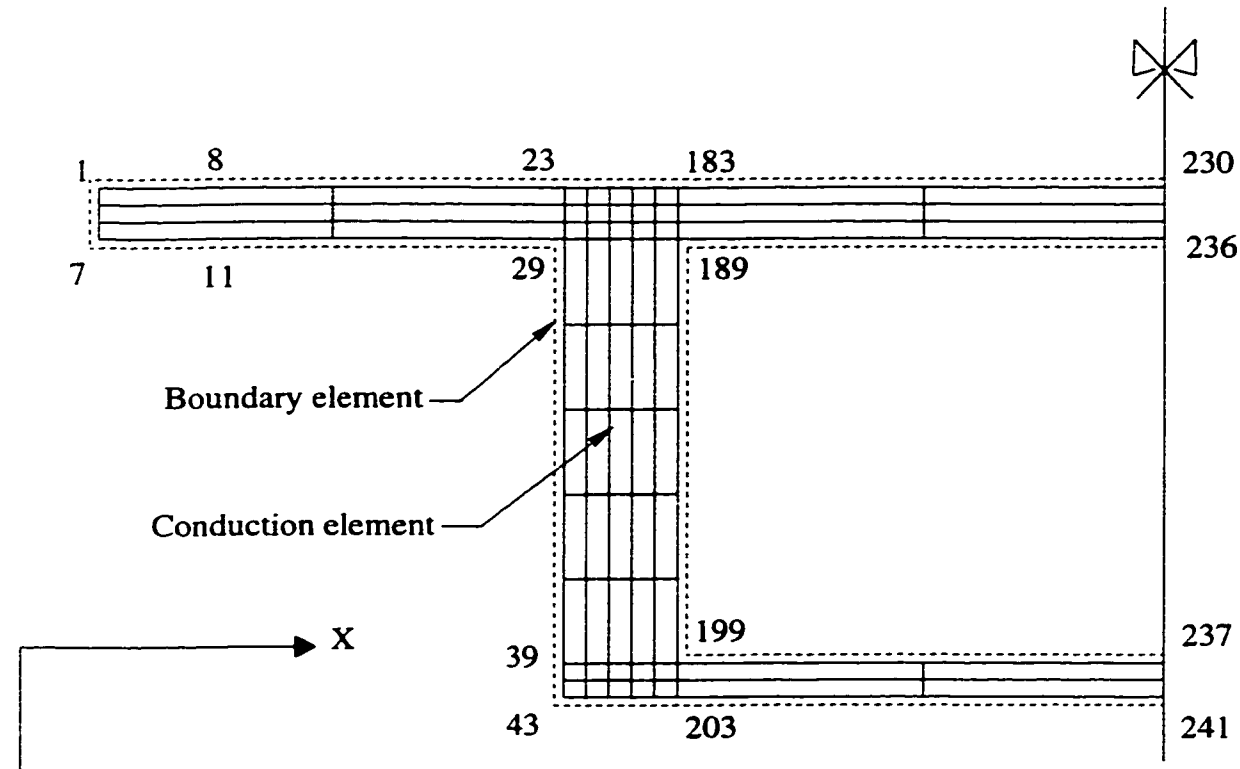

Mesh I (Coarse mesh)

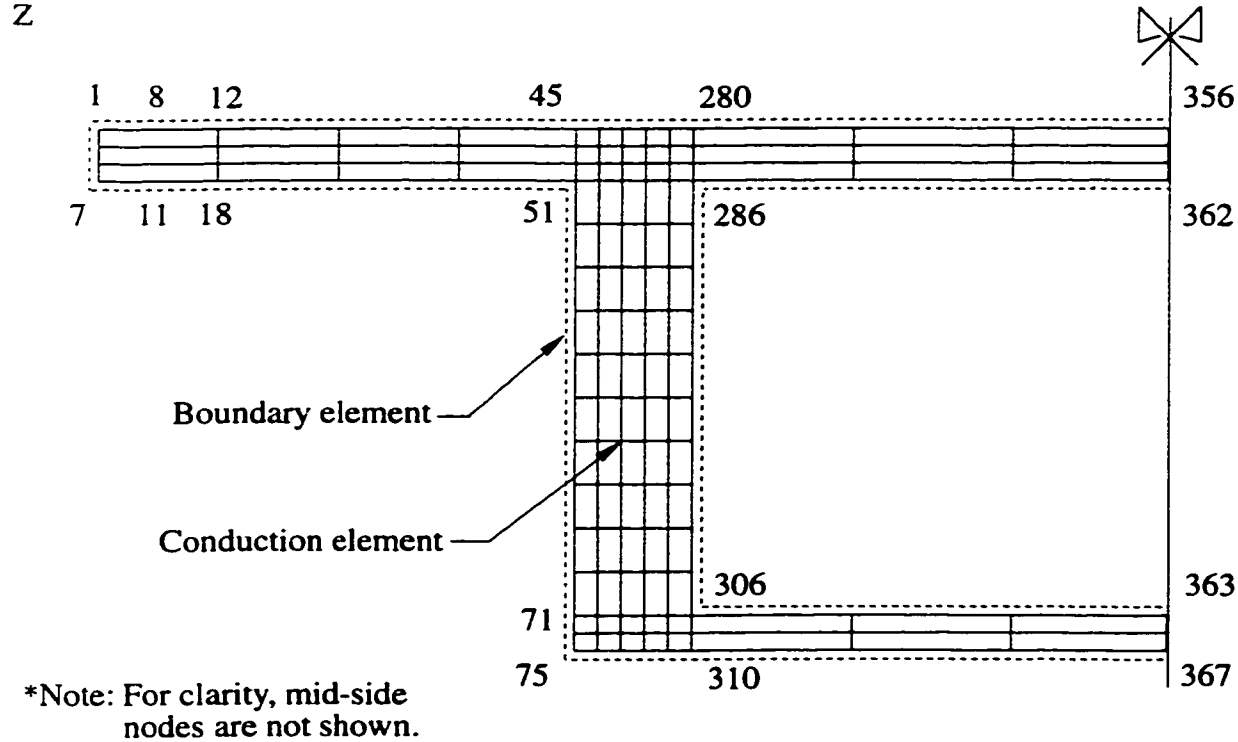

*Note: For clarity, mid-side nodes are not shown.

Mesh II (Fine mesh)

Figure 5.3 Coarse and fine meshes used in the analysis of mesh size at the cross-section level.

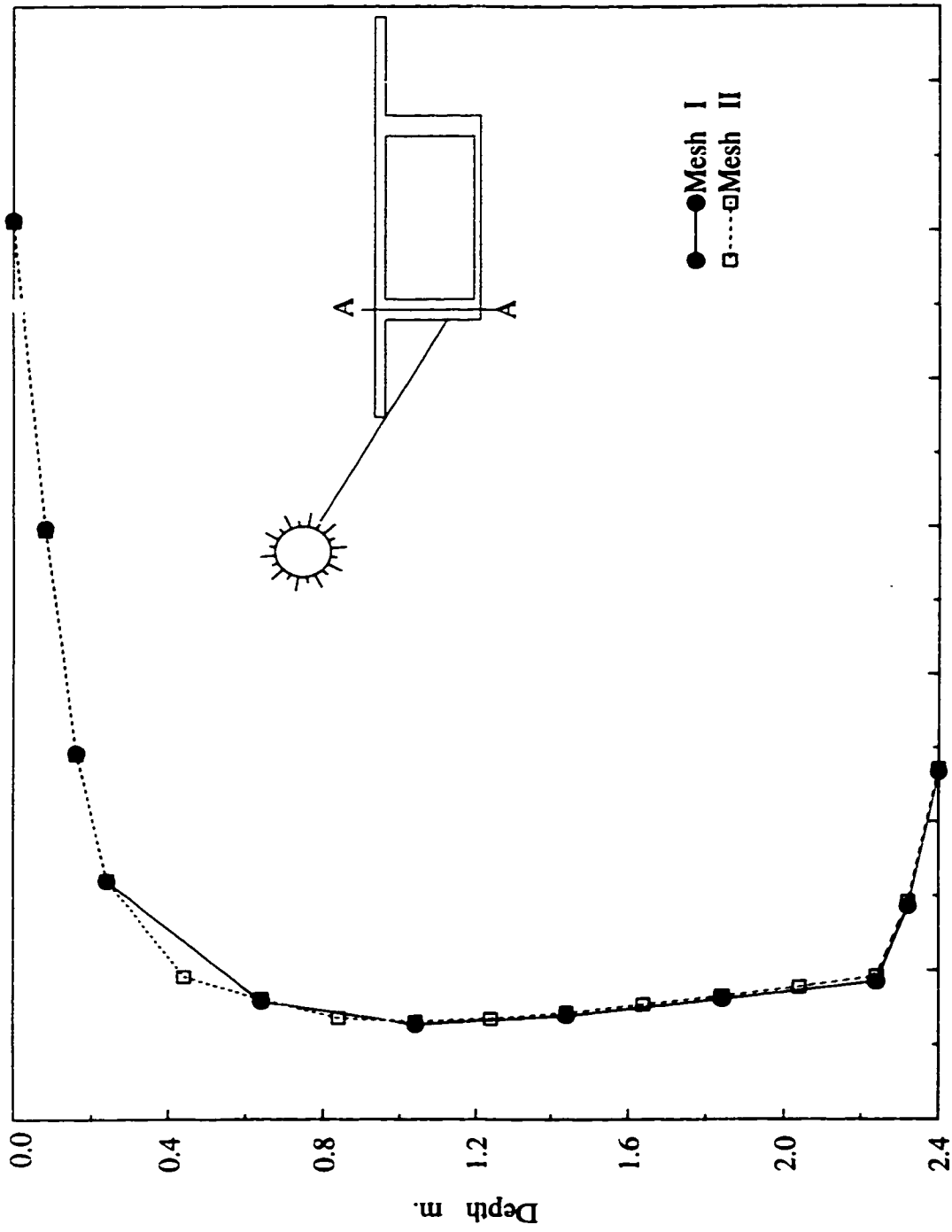

Figure 5.4 Comparison of temperature along the center line of the sunlit web (Section A-A) using Mesh I and Mesh II at 15:00 hr. of day four

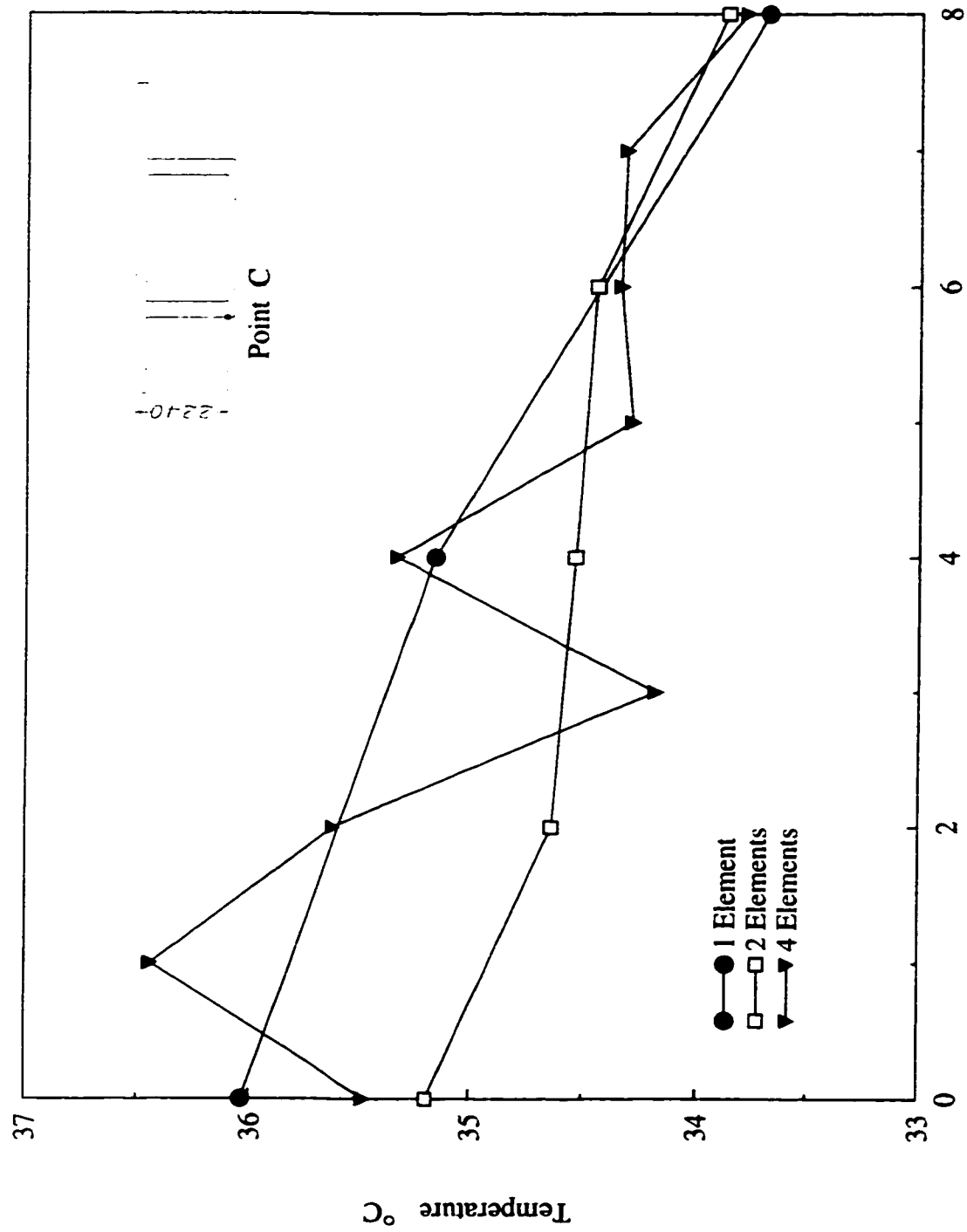

Figure 5.5 Comparison of longitudinal variation of temperature at point C on the surface of the sunlit web using 1, 2, and 4 elements along the bridge axis, at 17:00 hr. of day four

located in Quebec. The bridge is continuous over three spans with total length of 285 m. The central span is 180 m long and has a depth varying from 2.90 m at midspan to 9.75 m over the interior pier. Field measurements of temperature variations at certain points within the two cross-sections at midspan and over the pier were collected over a three-year period. Details on the bridge layout, the experimental program, the locations of thermocouples and the environmental conditions can be found in Massicotte et al. (1994).

Figure 5.6a shows the dimensions of the midspan cross-section and the location of thermocouples instrumented at the same section of the bridge. The comparison between the temperature values computed by *FETAB3D* and the measured values is made for measurements taken on May 24, 1992. The finite element mesh used in the analysis is shown in Figure 5.6b. As can be seen, some approximation in the geometry of the cross-section is made in the finite element discretization. This should not greatly affect the results. Thermal properties of concrete used in the analysis are the same as those given in Table 5.1 except that solar absorption coefficient, a, is taken as 0.6. Values of the convection heat transfer coefficient, h_c, for different surfaces of the box section are given in Table 5.2. Other data needed in the analysis are: day of the year = 144; latitude = 46° 37' 12" N; altitude = 350 m; orientation of bridge axis with respect to the North = N 65° E (γ = -25); turbidity factor, t_u = 3.5; albedo, ρ_d = 0.05; $T_{a,\,max}$ = 25° and $T_{a,\,min}$ = 5 °.

It should be mentioned here that the top surface of the bridge is covered by a layer of asphalt. This layer will cause a slight increase in the temperature values only at the surface and in the top slab without greatly affecting the temperature distribution over the cross-section depth [Elbadry (1982)]. In the analysis by *FETAB3D*, this asphaltic layer is ignored.

Figure 5.7 and 5.8 show a comparison between the temperature distribution as predicted

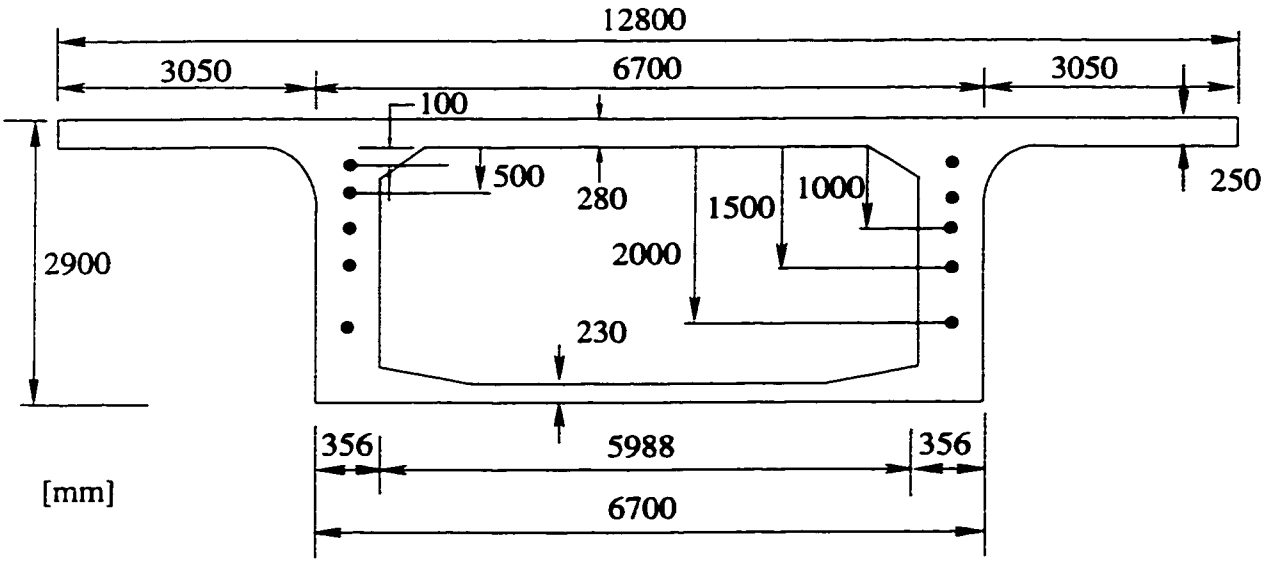

a) Cross-section dimensions and location of thermocouples

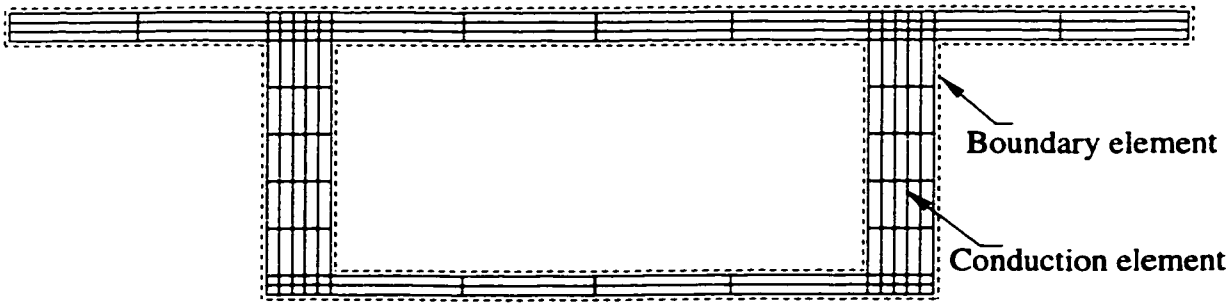

unit length in the other direction.

1109 Nodes
132 Conduction Elements
74 Boundary Elements

b) Finite element mesh

Figure 5.6 Cross-section dimensions and finite element idealization for the analysis of the Grand-Mère Bridge.

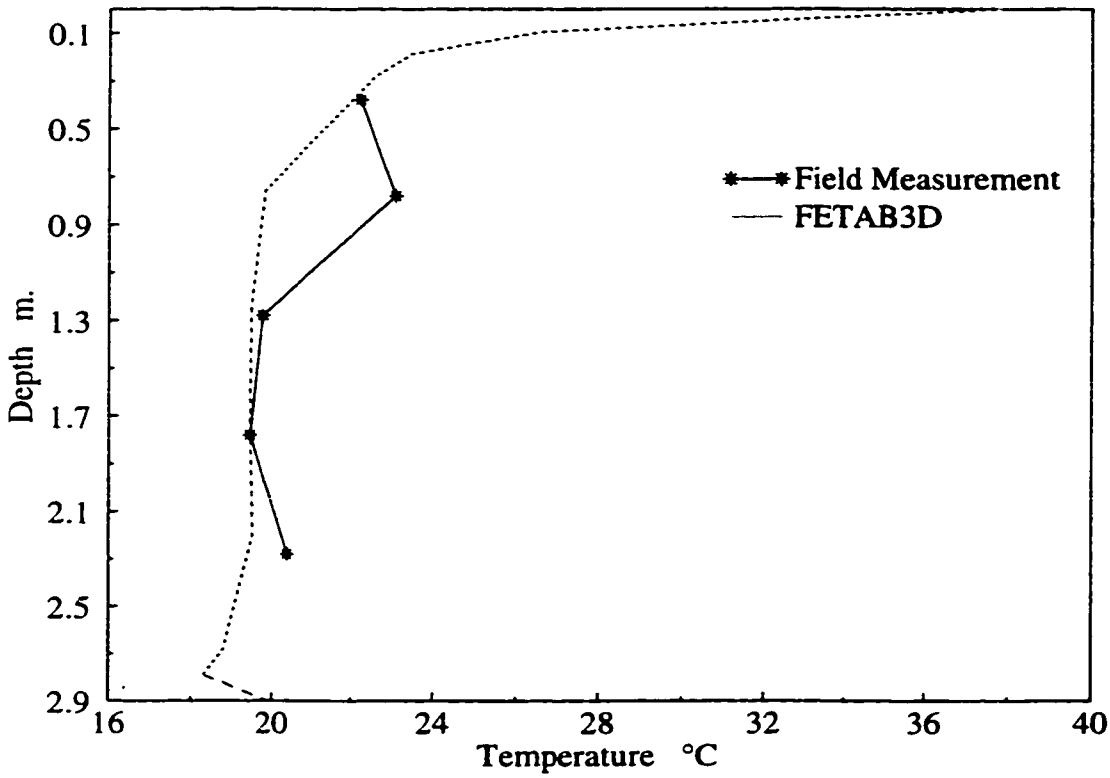

Figure 5.7 Experimental and analytical vertical temperature distribution along the South web, May 24, 1992. 10:00 hr.

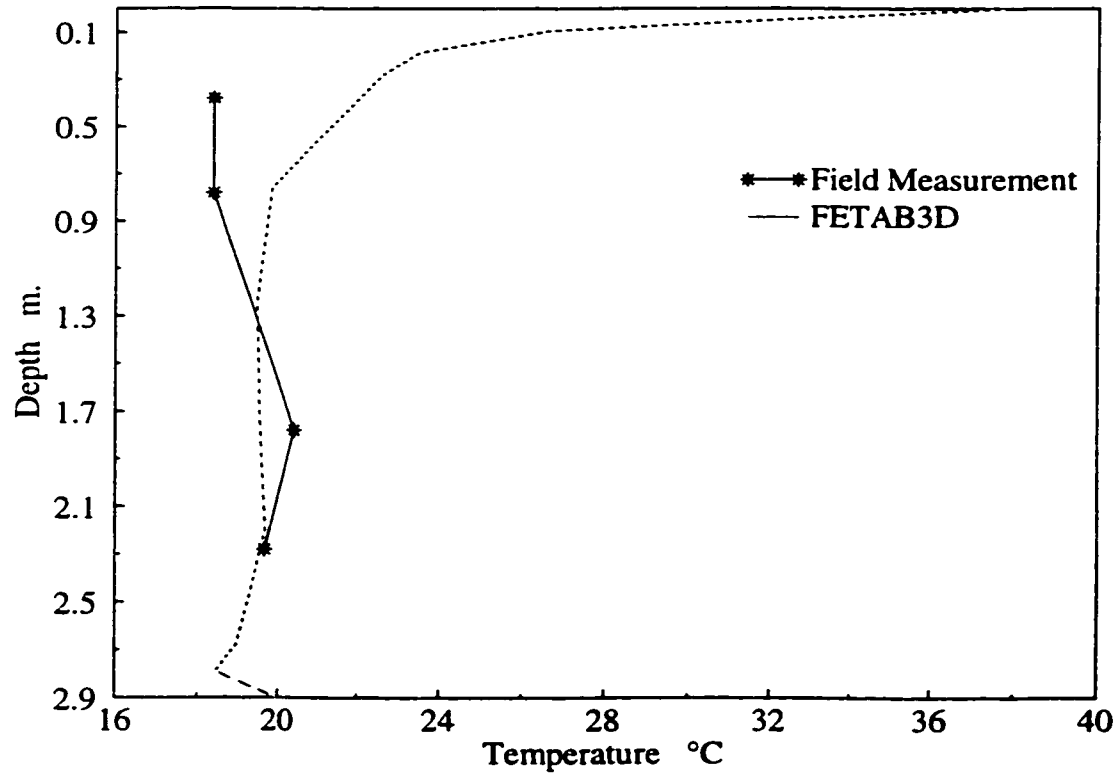

Figure 5.8 Experimental and analytical vertical temperature distribution along the North web, May 24, 1992. 10:00 hr.

by *FETAB3D* and the temperature values measured by the thermocouples located at the center line of the east and west webs, respectively. The predicted temperatures agree satisfactorily with the measured values.

5.5 Case Study

The data described in section 5.2 is employed to compute the temperature distribution within the bridge of Figure 5.1. Results of the analysis are shown in Figures 5.9 to 5.14. A variety of figures for the temperature distribution in different parts of the bridge can be shown. However, only the figures that are necessary to show the significance of the variation of temperature distribution along the bridge length at certain hours of the day are presented. The analysis starts at 4:00 a.m of the first day of a four-day analysis period and the results are presented only for the fourth day.

Figure 5.9 and Figure 5.10 describe the variation along the bridge length of temperatures calculated at points C and D for different hours of the day. Points C and D are located on the outer surface of the west and east webs, respectively, near the bottom slab. These points are chosen because they avoid the shade provided by the overhangs during most of the hours of the day. It was observed that points on the surface of the web near the top slab (shaded during most of the hours of the day) do not experience significant temperature variation along the bridge length.

Figures 5.11 to 5.14 show the vertical temperature distribution through the center line of the west and east web, respectively, for different angles ψ along the bridge length, at different hours of the day. The horizontal temperature variations at the mid height of the west and east webs are also shown in these figures.

Examination of the figures reveals the following:

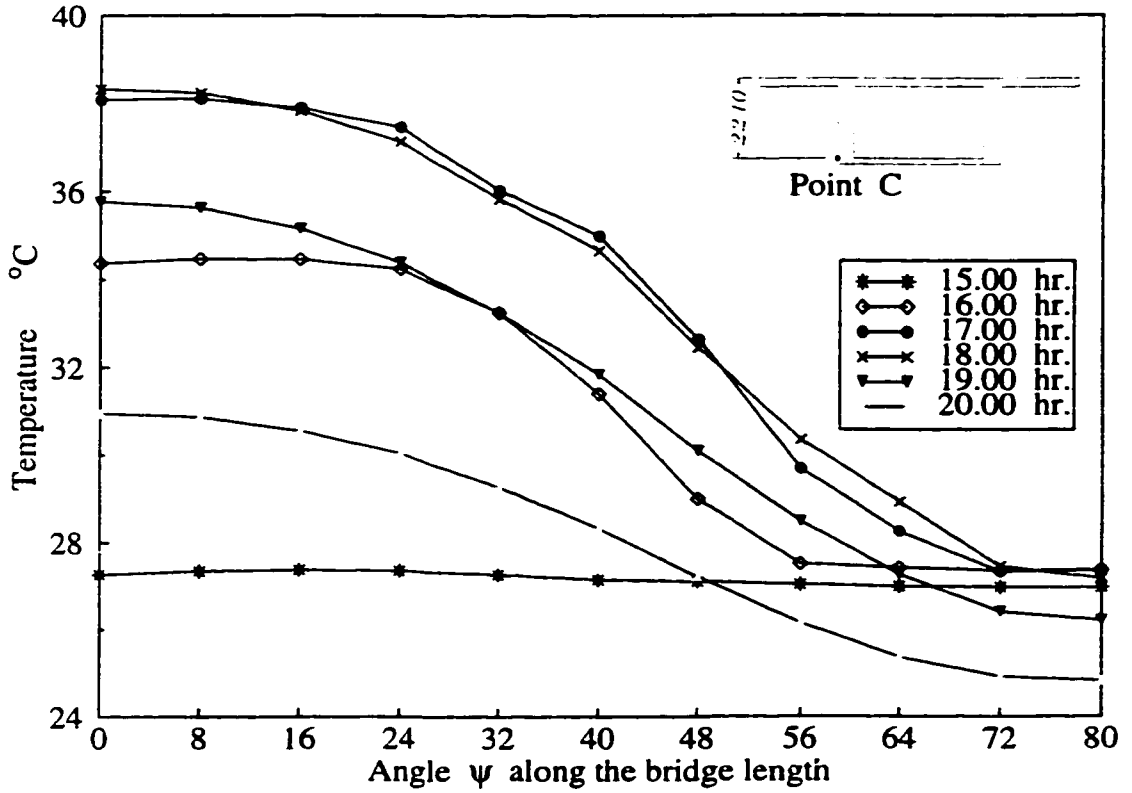

Figure 5.9 Longitudinal variation of temperature at point C on the west web surface, summer conditions

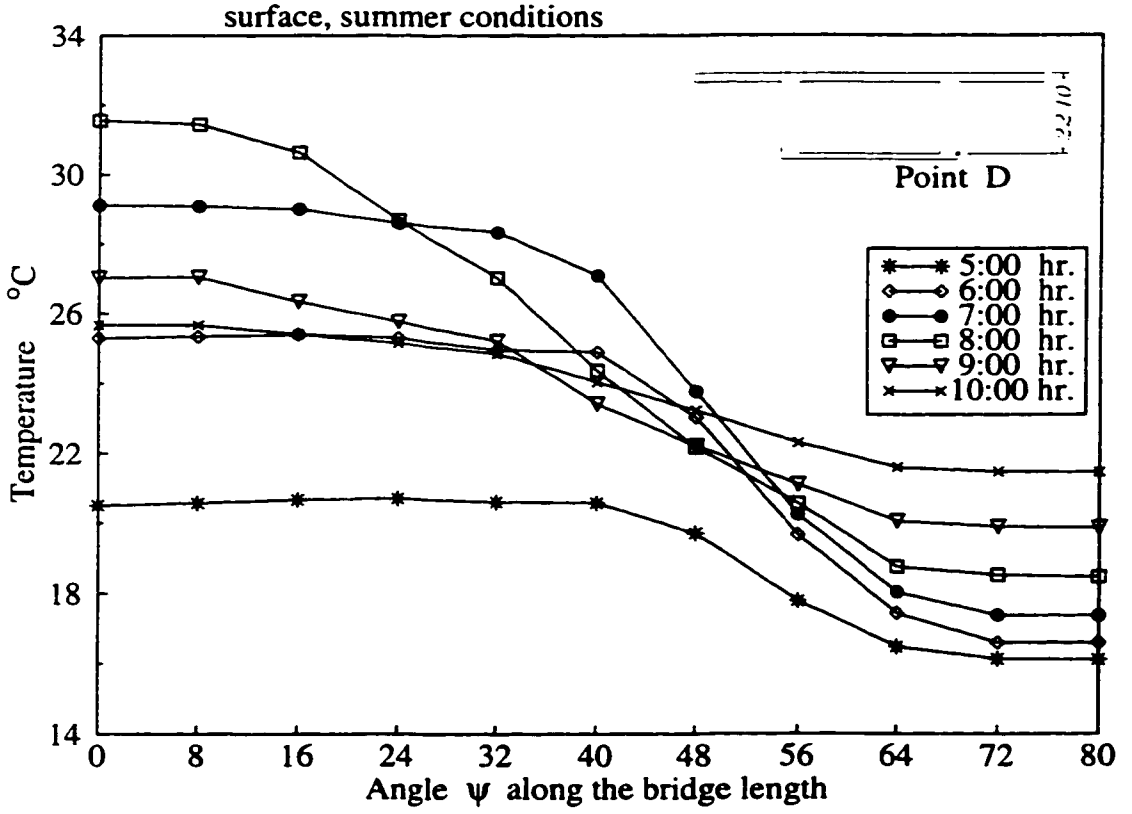

Figure 5.10 Longitudinal variation of temperature at point D on the east web surface, summer conditions

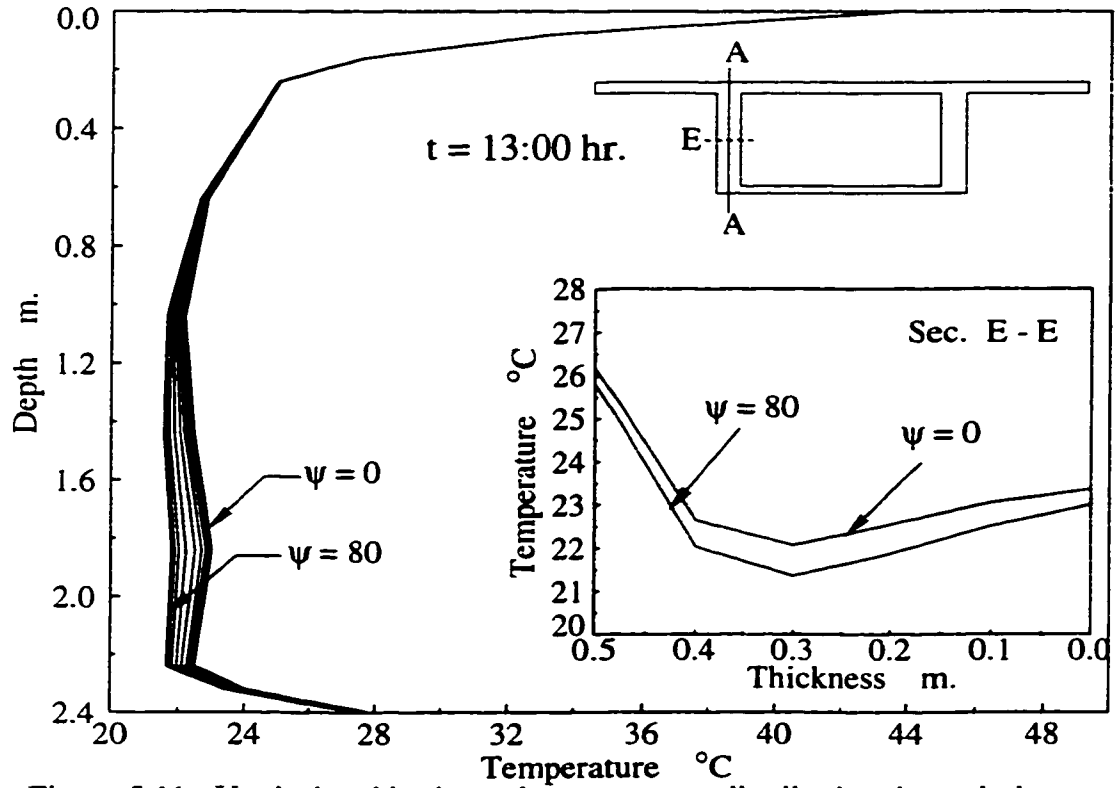

Figure 5.11 Vertical and horizontal temperature distribution through the west web for different angles, ψ, along the bridge length, summer conditions.

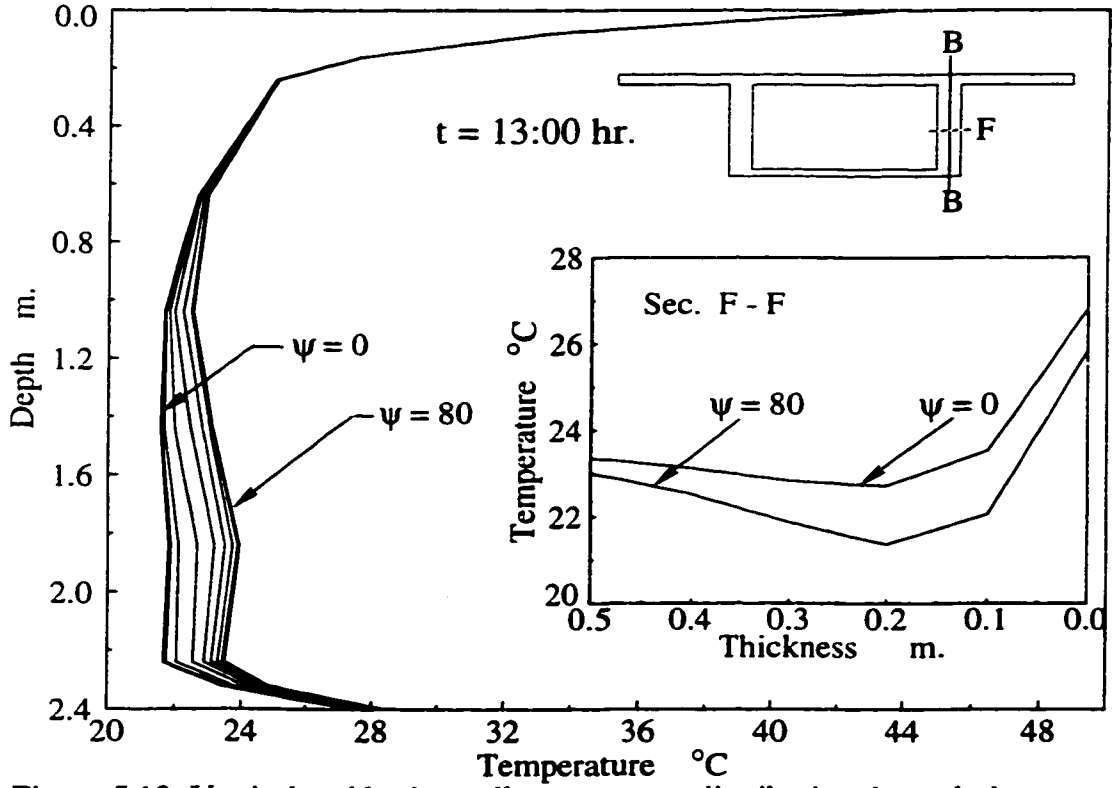

Figure 5.12 Vertical and horizontall temperature distribution through the east web for different angles, ψ, along the bridge length, summer conditions.

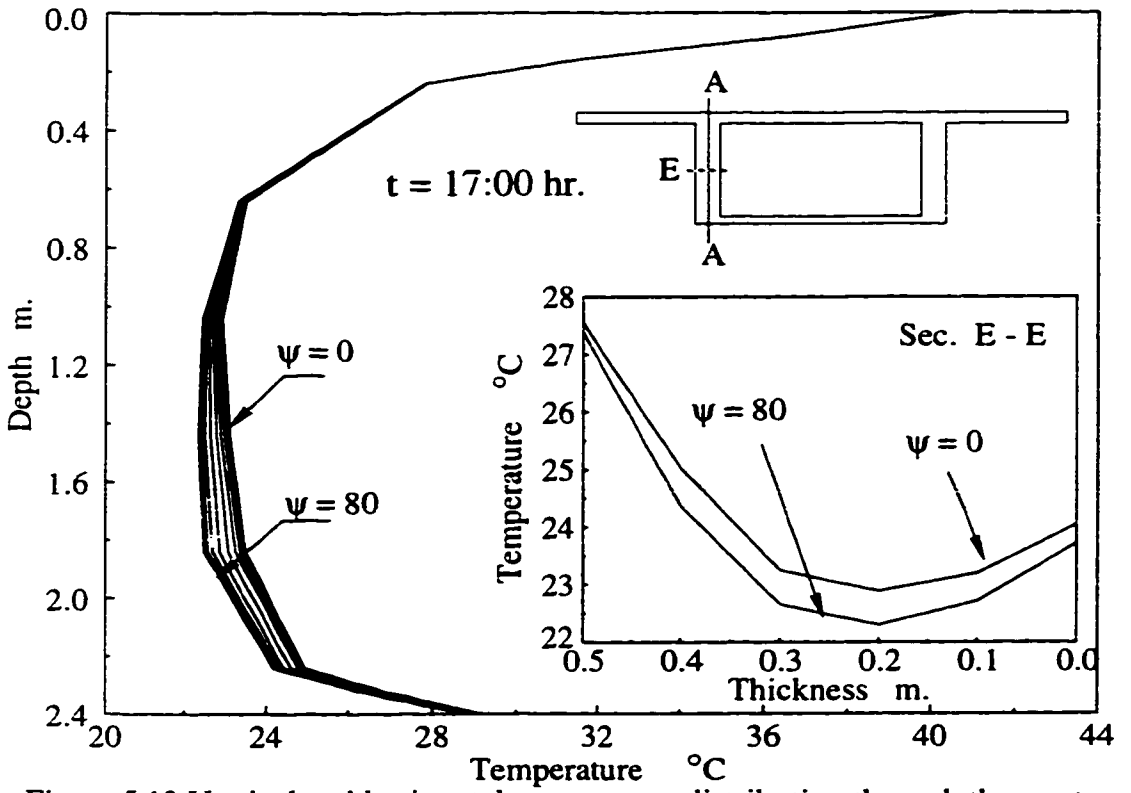

Figure 5.13 Vertical and horizontal temperature distribution through the west web for different angles, ψ, along the bridge length, summer conditions.

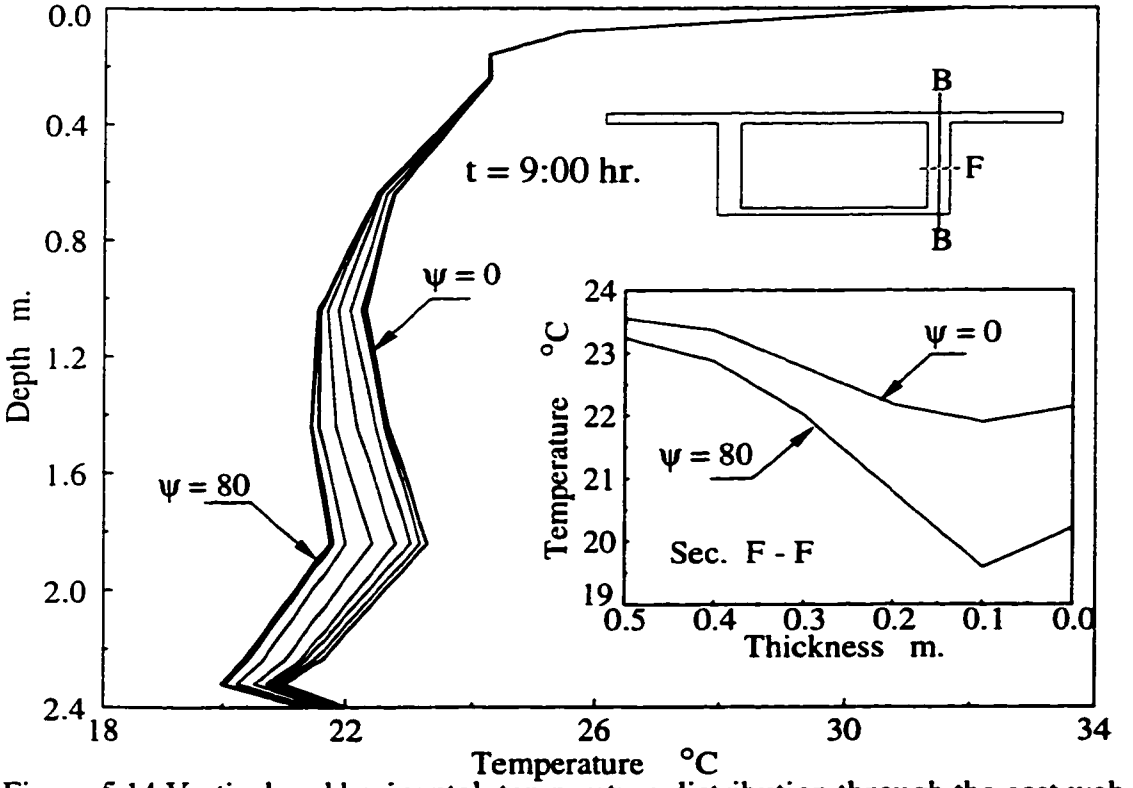

Figure 5.14 Vertical and horizontal temperature distribution through the east web for different angles, ψ, along the bridge length, summer conditions.

1- Significant temperature variations along the bridge length exist through the web of the box girder. This variation reaches maximum values at the outer surface of the web and can be as large as 13 °C between the two end sections of the bridge.

2 - The variation of vertical temperature through the center line of the web, along the bridge length, is less significant. The difference in temperature along the bridge length is approximately 8 percent.

3 - The temperature variation along the bridge length is dependant, as expected, on the time of the day and the orientation of the surface with respect to the sun [i.e. surface azimuth angle γ (see Equation 4.6)].

It should be noted that it is necessary to calculate the stresses induced in the bridge for different cases of temperature distribution in order to determine the critical temperature distribution developed in the bridge and the corresponding conditions that cause this distribution. The computer program *FETAB3D* described in chapter 4, computes the principal stresses for each element at Gauss sampling points. In the present study, a mesh composed of 6860 nodes was utilized to model the 80 degrees curved bridge in 10 segments, each of 8 degrees length (i.e. $\psi = 8^{\circ}$). This mesh was found sufficient to predict the temperature values with good accuracy (section 5.3). However, the selected mesh is not fine enough to compute the stresses induced in the bridge with reasonable accuracy. Figure 5.15 shows the stress distribution along the center line of the web of the cross-section computed for a simply supported curved beam having the cross-section of Figure 5.1b with 16 degrees at the center. The beam is divided into either two segments along the bridge axis (similar to the current mesh), or four segments each of 4 degrees long. Comparison of the results between the two meshes shows differences of up to 54%. Therefore, a finer mesh should be used to obtain more accurate results when calculating stress values. Utilizing a finer mesh implies adding many thousands of nodes and elements to the current

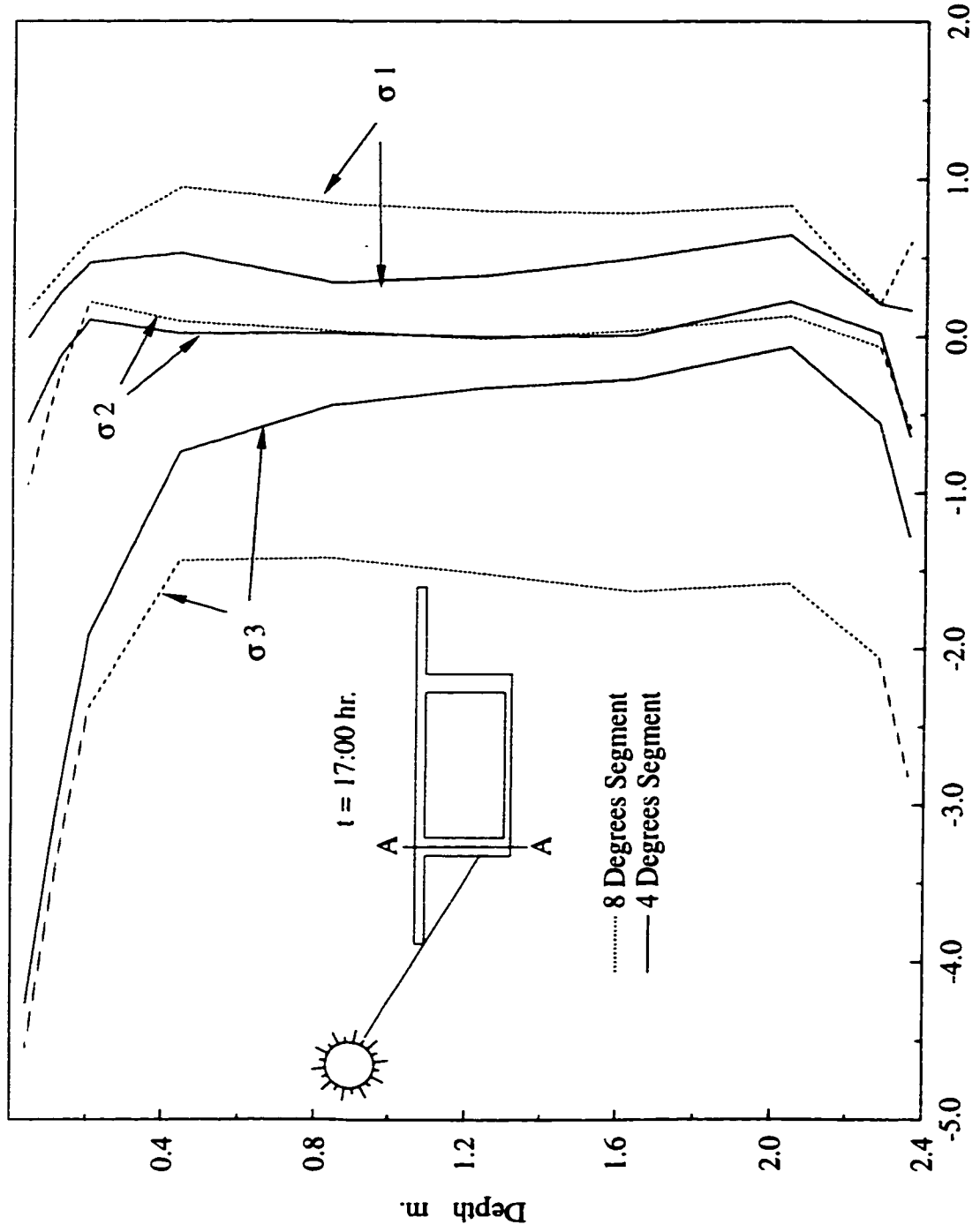

Figure 5.15 Comparison of stresses along the center line of the sunlit web (Section A-A) at $\psi = 8°$ using 4, and 8 degree segments along the bridge axis for a simply supported curved beam.

mesh. It is worth mentioning that the execution time of the program needed to obtain the nodal temperature at the fourth day of analysis using the current mesh is approximately 2900 minutes with 98 megabyte of hard disk space of the computer. For the above reasons, it was deemed necessary to limit the current study to temperature calculations only.

5.6 Parametric Study

Development of temperature variations and the corresponding stresses induced in bridge structures are influenced by several parameters; some of them are pertinent to the environmental conditions and others are related to the geometry of the bridge itself. Several researchers studied the effects of temperature variations only over the cross-section of concrete box girder bridges; among them: Kehlbeck (1975), Emerson (1979), Elbadry and Ghali (1983a), Mirambell and Aguado (1990), Branco and Mendes (1993). Their investigations dealt with the influence of the various parameters that affect the vertical and horizontal temperature distributions and the corresponding stresses induced in the cross-section.

In the present investigation, only three parameters that are believed to have significant effects on the variation of temperature along the axis of curved concrete box girder bridges are considered. These parameters are:

- season of the year;
- orientation of the bridge axis with respect to the North;
- overhanging length - web depth ratio (OWR).

In the following, the case study described in section 5.5 will be considered as a reference case for comparison. The above parameters are changed and analyzed separately before comparing with the reference case to determine their effect on the three dimensionality of temperature distribution within the bridge. Throughout the analysis, the material proper-

ties listed in Table 5.1 are held constant unless otherwise noted.

5.6.1 Season of the Year:

The solar energy reaching the surface of a bridge changes with the time of the year (i.e. from season to season) depending on the solar declination δ with respect to the axis of the earth. In this Subsection, thermal response of the bridge in Figure 5.1 is analyzed for certain days during different seasons: Fall, Winter, and Spring. Details of the climatological conditions for the different days considered in the analysis are given in Table 5.3. Figures 5.16 to 5.21, Figures 5.22 to 5.27, and Figures 5.28 to 5.33 depict the variation shown in Figures 5.9 to 5.14 but for Fall, Winter and Spring conditions, respectively. Comparison of these figures with the reference case (Summer condition) indicates the following:

1- The maximum temperature difference along the surface of the web occurs in the Spring, whereas, the minimum difference occurs under winter conditions. the maximum temperature difference between the two end sections of the bridge can reach up to 14 °C during the Spring, 8 °C in Winter, and 13 °C during the Fall, as compared to 13 °C in the Summer.

2 - The variation of vertical temperature distribution from one section to another along the bridge length is not pronounced during the different seasons, except in Winter, where a change of 5 °C (25 percent) can occur through the web along the bridge length (see Figure 5.27).

3 - The time of the day at which the difference in temperature is significant, varies from season to season. This is due the fact that the change in time at sunrise and sunset greatly influences the amount of the solar radiation received by the surface during a given hour.

4 - The increase in temperature along the web surface is different in direction from one season to another (Figures 5.9, 5.16, 5.22, and 5.28). The change in direc-

Table 5.3: Climatological conditions for certain days during different seasons

Variable	Fall	Winter	Spring	Summer	Reference
Date and Number of the day in the year, D	September 21 = 264	December 21 = 356	March 21 = 81	July 17=173	
Solar Declination, δ	0.0	-23.45	0.0	23.45	Equation (4.24)
Time at sunrise, t_{sr}, hour	6:00	8:15	6:00	3:50	Equation (4.25)
Time at sunset, t_{sr}, hour	18:00	15:45	18:00	20:10	Equation (4.26)
Turbidity factor, t_u	3.9	3.1	3.5	4.2	Figure 4.3
Maximum air temperature, $T_{a,max}$, °C	15	-10	+5	+30	
Minimum air temperature, $T_{a,min}$, °C	-5	-30	-15	+10	

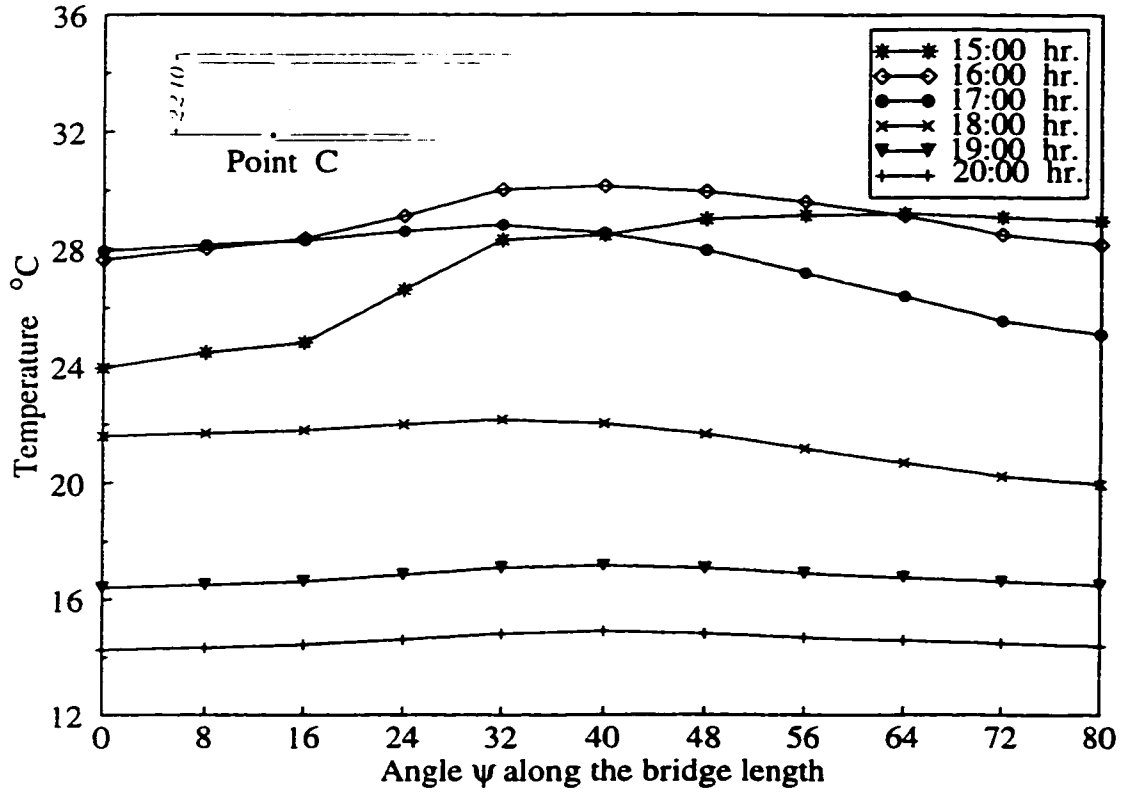

Figure 5.16 Longitudinal variation of temperature at point C on the west web surface, Fall conditions

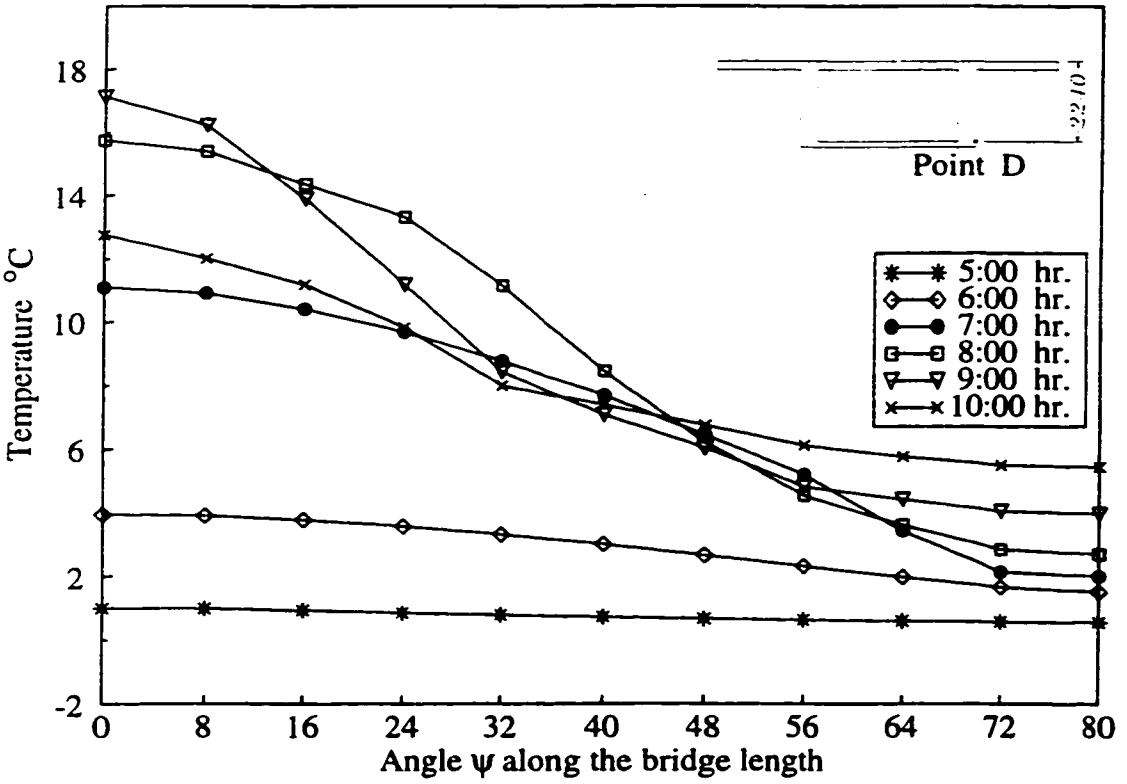

Figure 5.17 Longitudinal variation of temperature at point D on the east web surface, Fall conditions

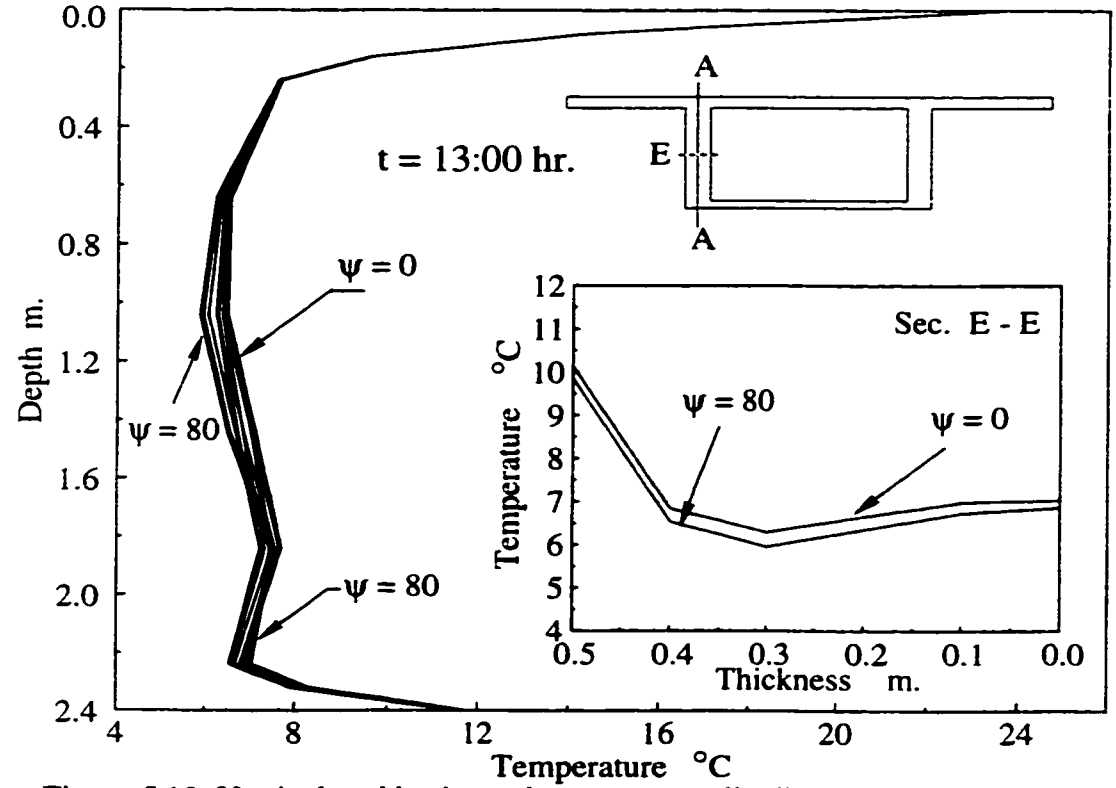

Figure 5.18 Vertical and horizontal temperature distribution through the west web for differentangles, ψ, along the bridge length,Fall conditions.

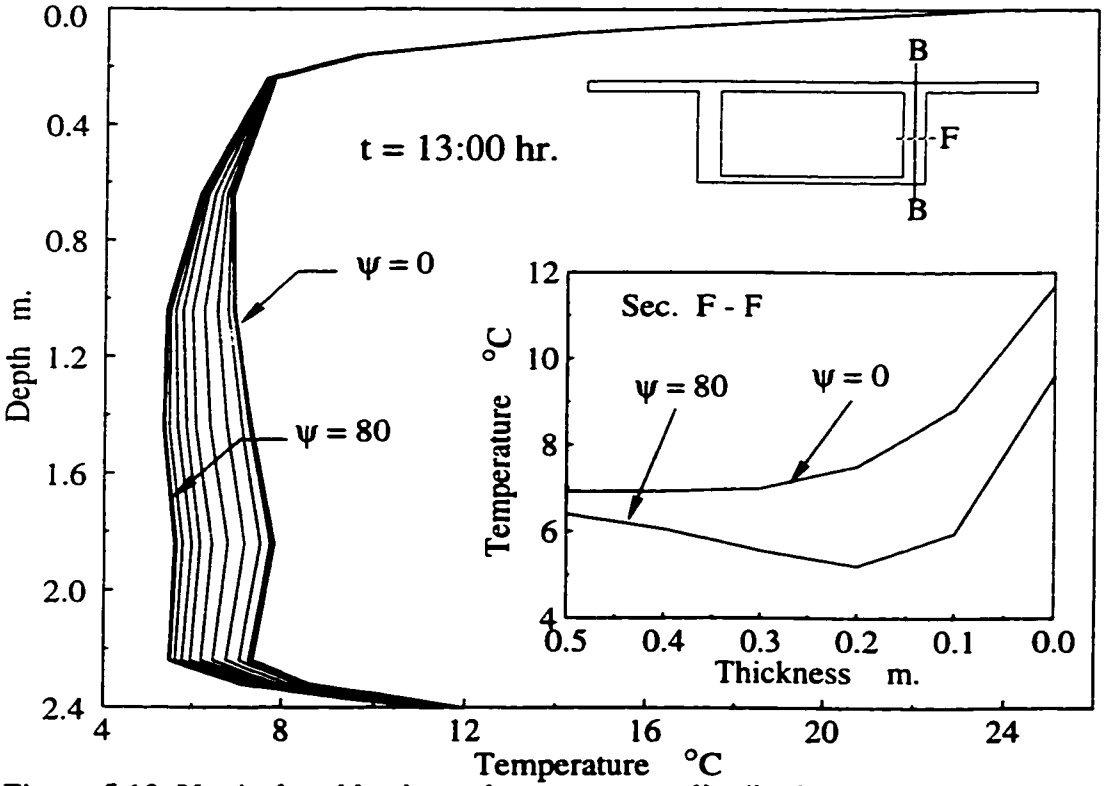

Figure 5.19 Vertical and horizontal temperature distribution through the east web for different angles, ψ, along the bridge length, Fall conditions.

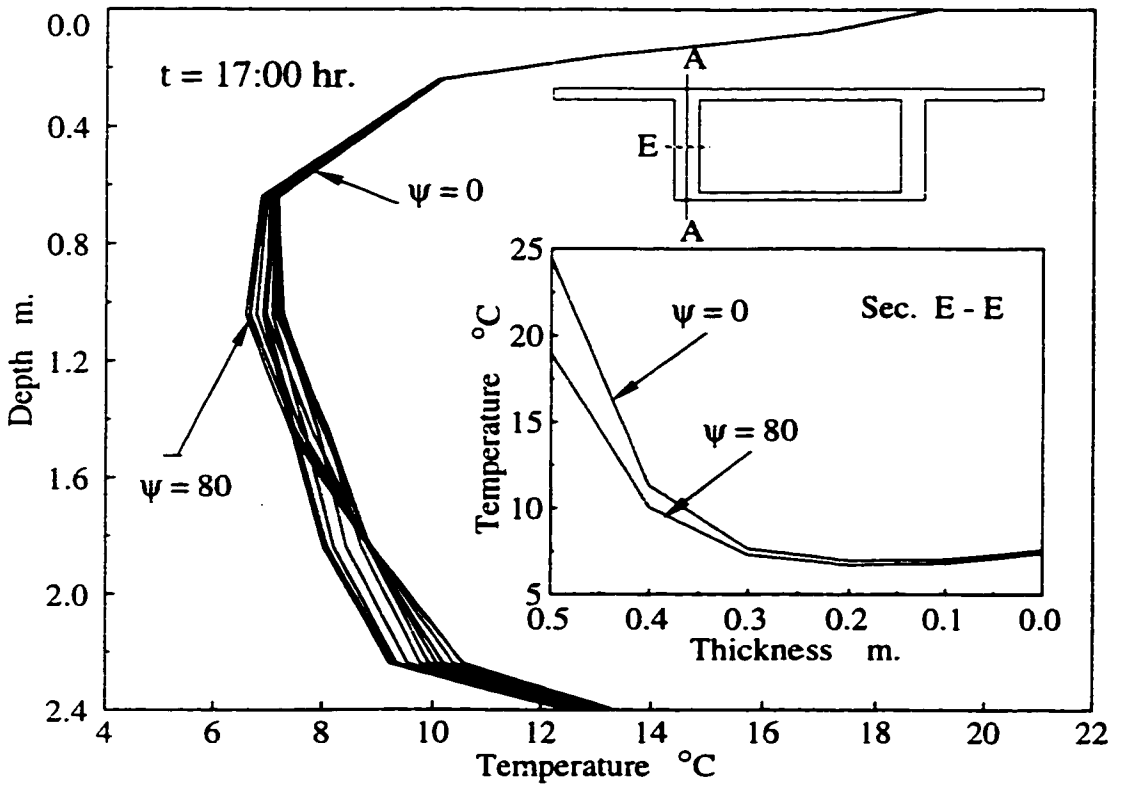

Figure 5.20 Vertical and horizontal temperature distribution through the west web for differentangles, ψ, along the bridge length, Fall conditions.

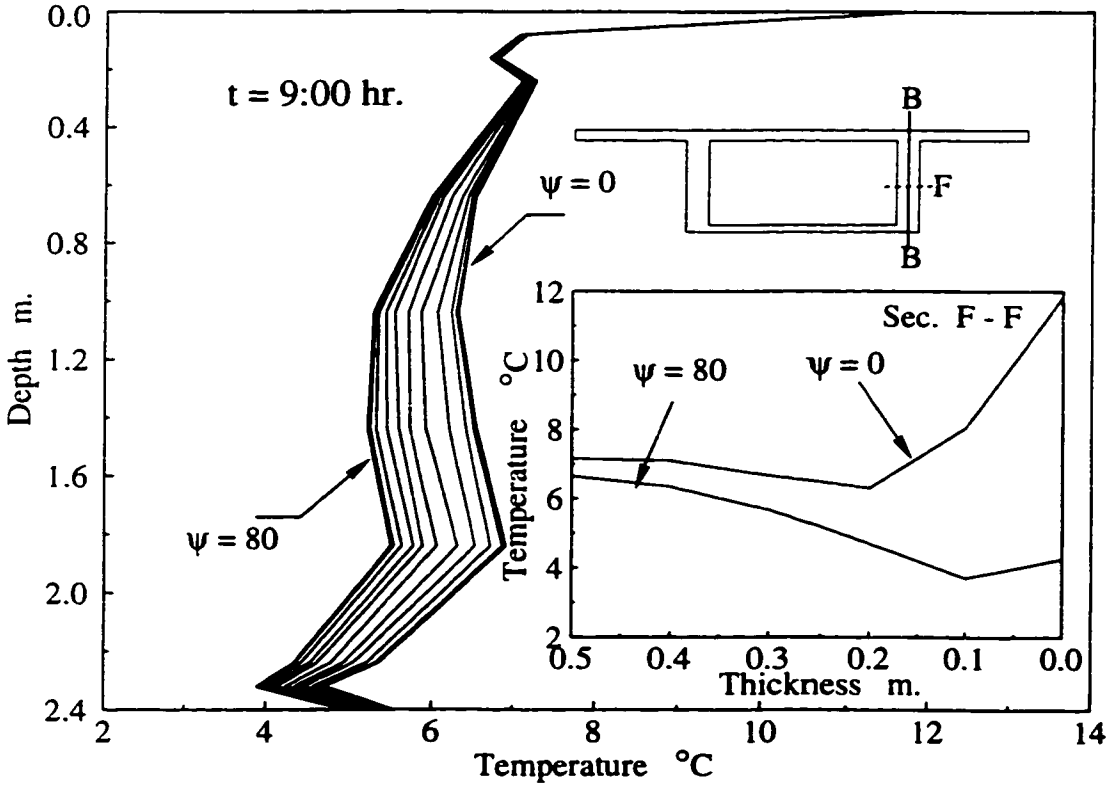

Figure 5.21 Vertical and horizontal temperature distribution through the east web for different angles, ψ, along the bridge length,Fall conditions.

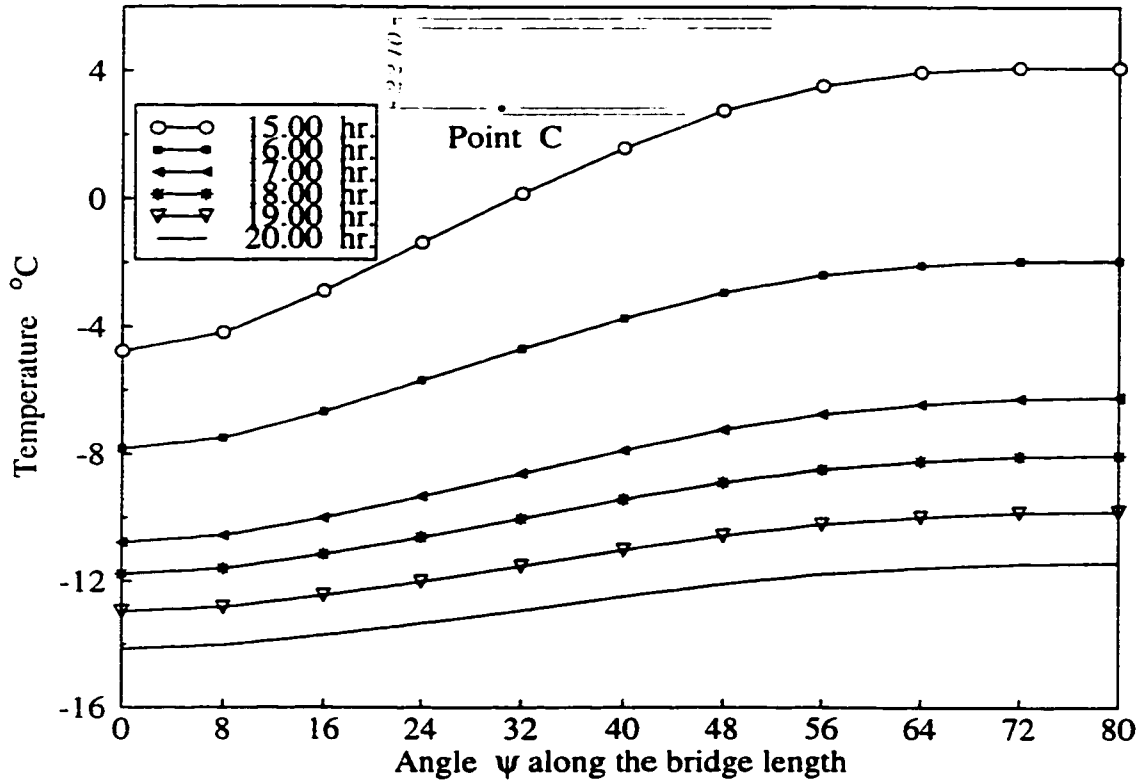

Figure 5.22 Longitudinal variation of temperature at point C on the west web surface, Winter conditions

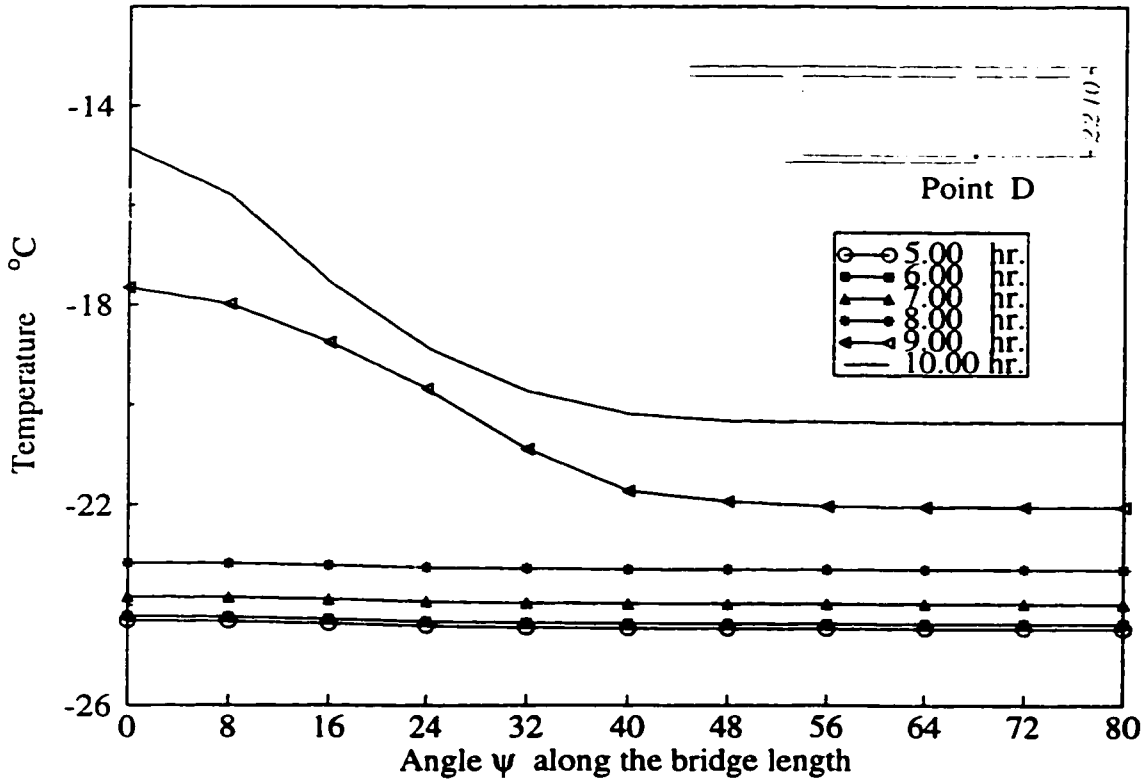

Figure 5.23 Longitudinal vartiation of temperature at point D on the east web surface, Winter conditions

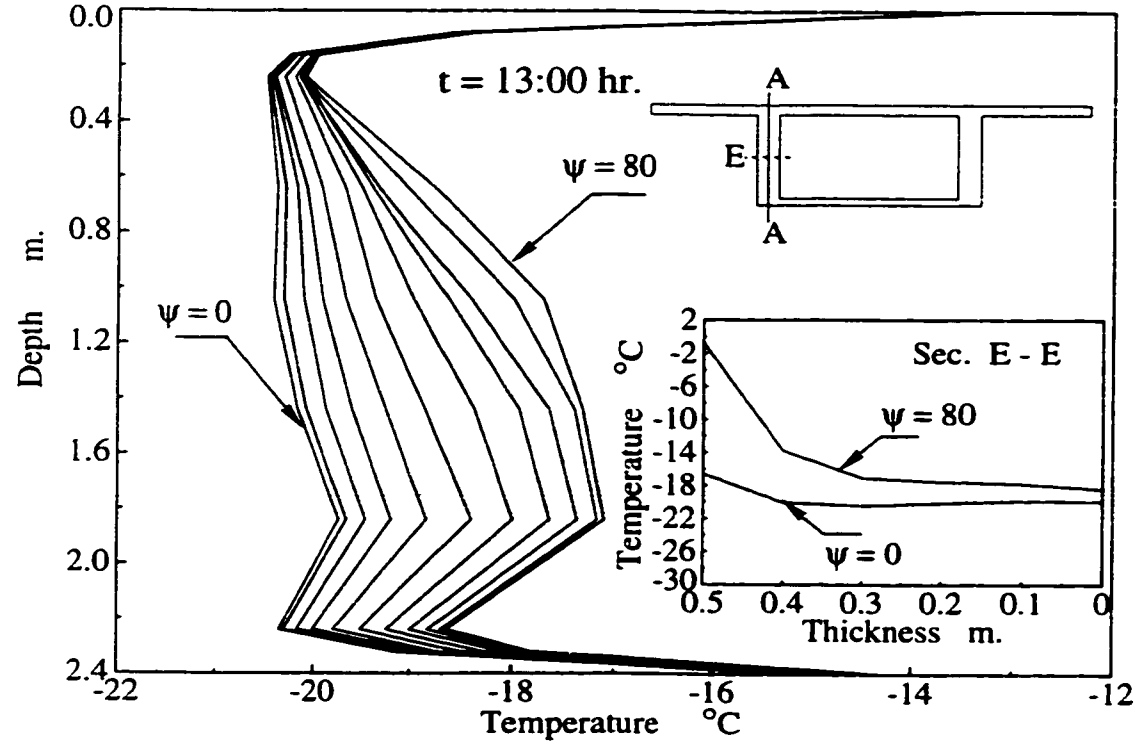

Figure 5.24 Vertical and horizontal temperature distribution through the west web for differentangles, ψ, along the bridge length, Winter conditions.

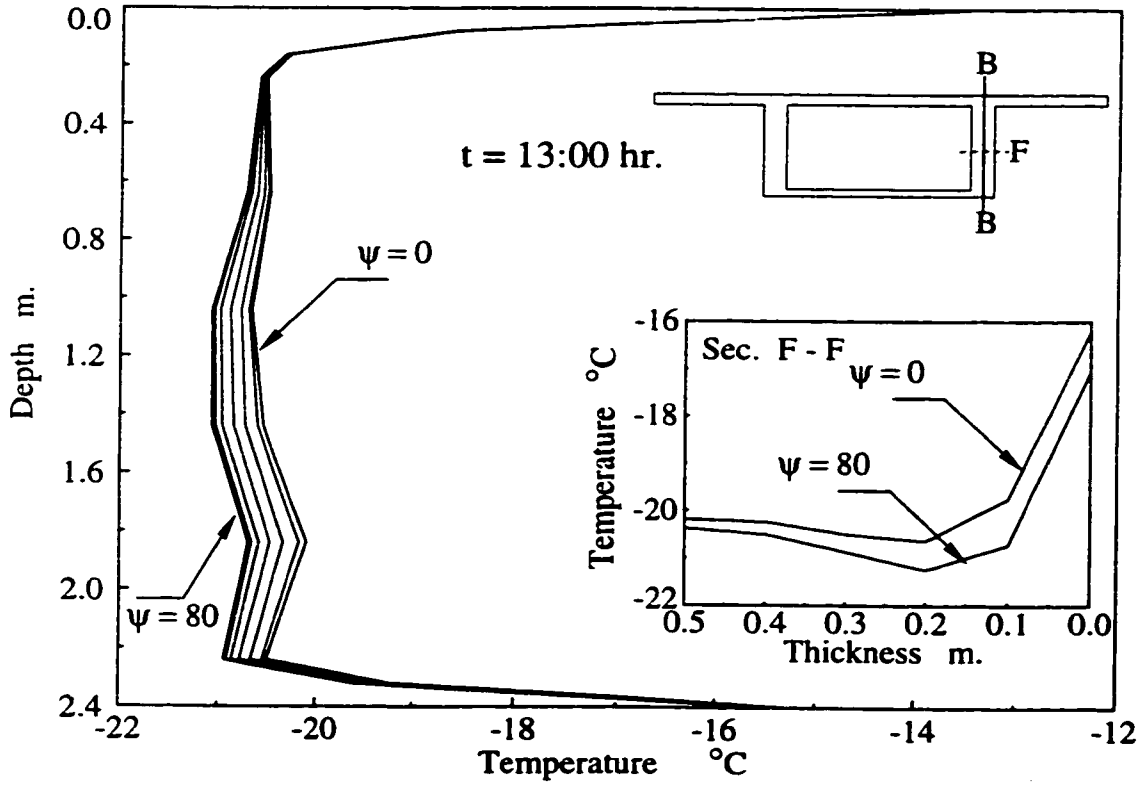

Figure 5.25 Vertical and horizpontal temperature distribution through the east web for different angles, ψ, along the bridge length, Winter conditions

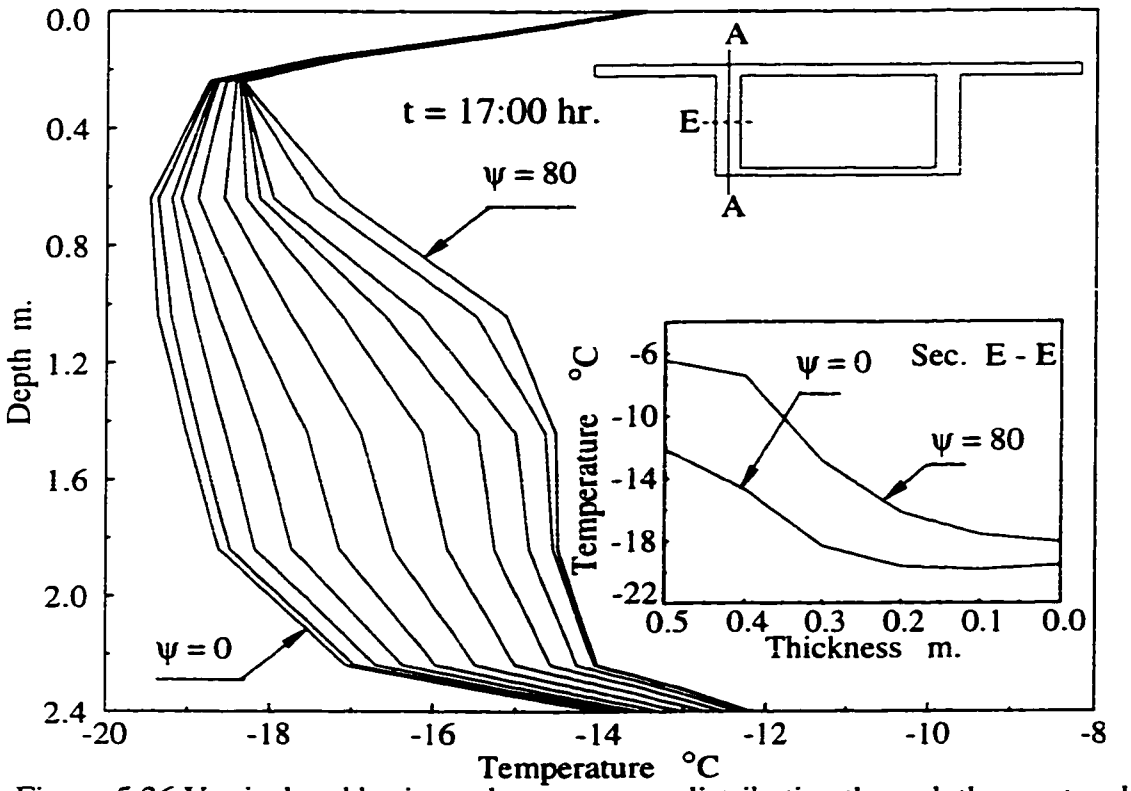

Figure 5.26 Vertical and horizontal temperature distribution through the west web for different angles, ψ, along the bridge length, Winter conditions

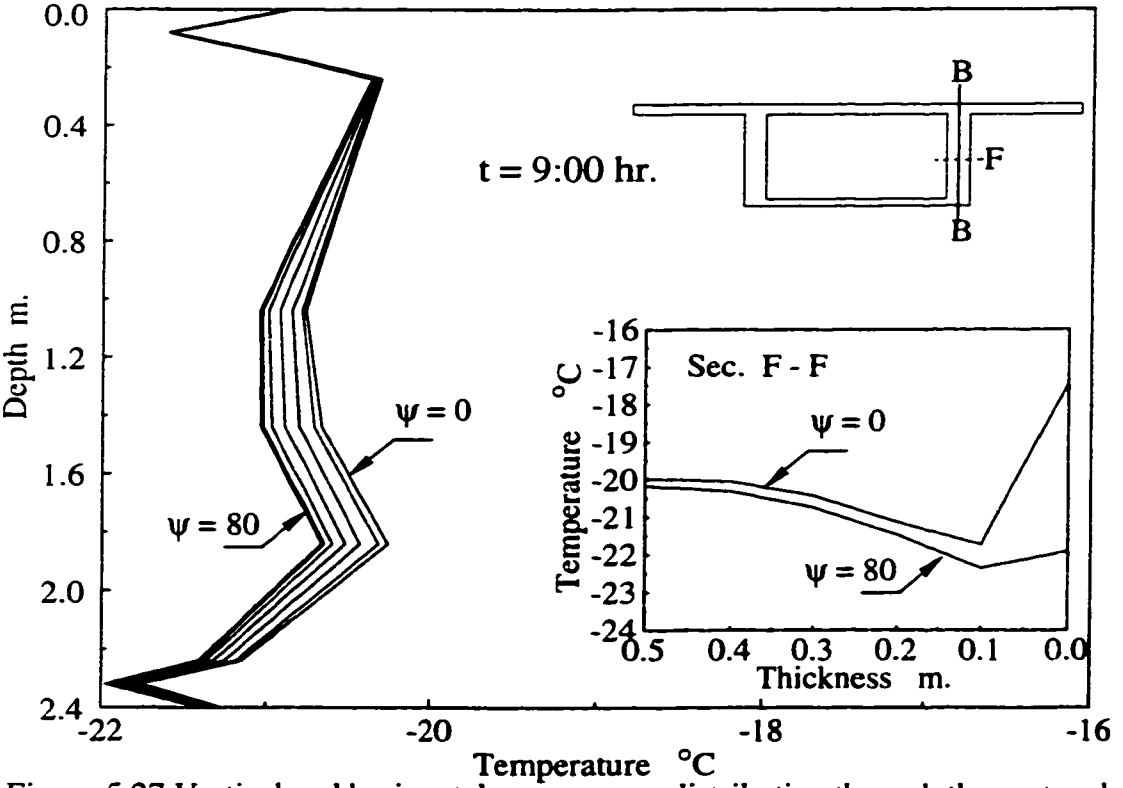

Figure 5.27 Vertical and horizontal temperature distribution through the east web for different angles, ψ, along the bridge length, Winter conditions

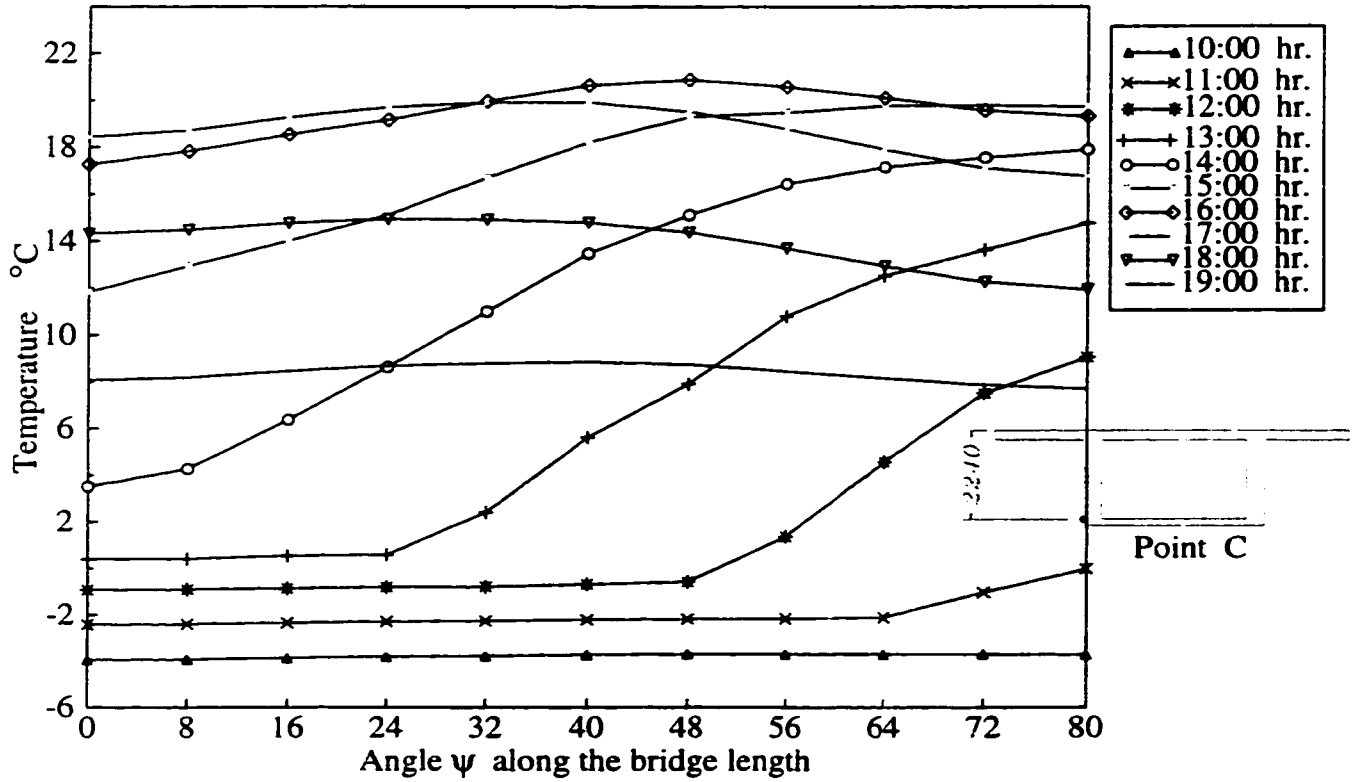

Figure 5.28 Longitudinal variation of temperature at point C on the west web surface, Spring conditions

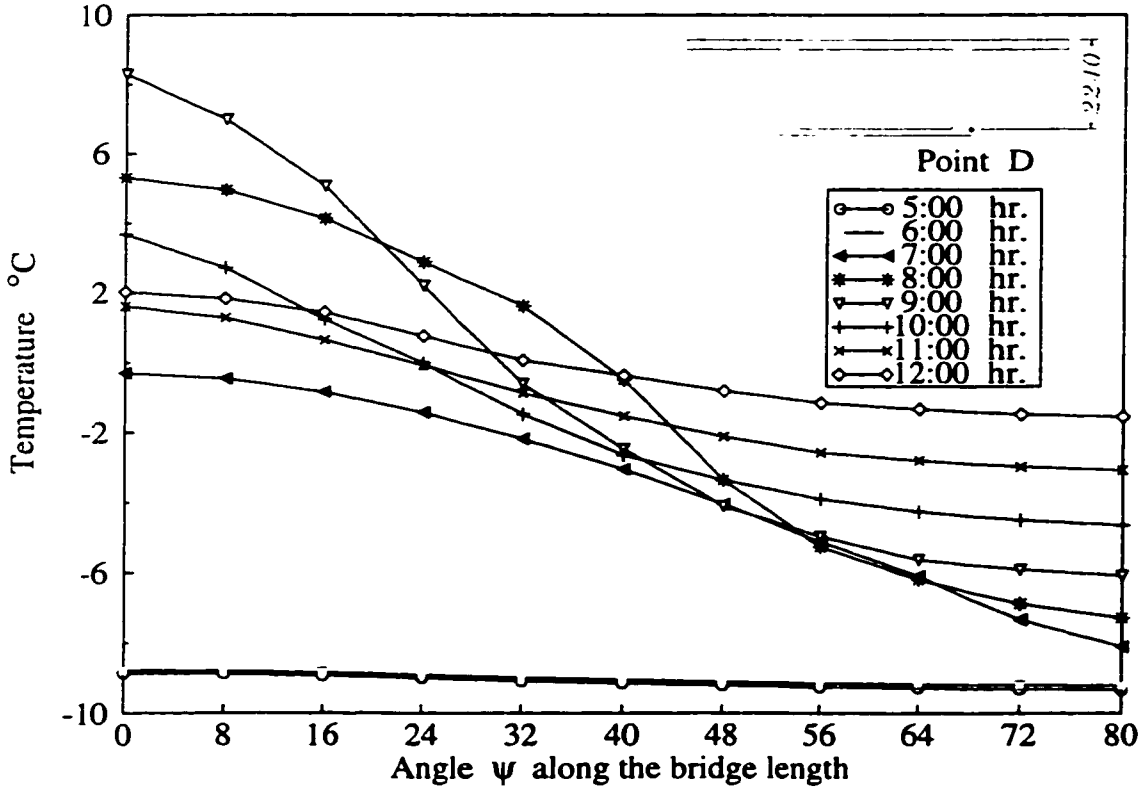

Figure 5.29 Longitudinal variation of temperature at point D on the east web surface, Spirng conditions

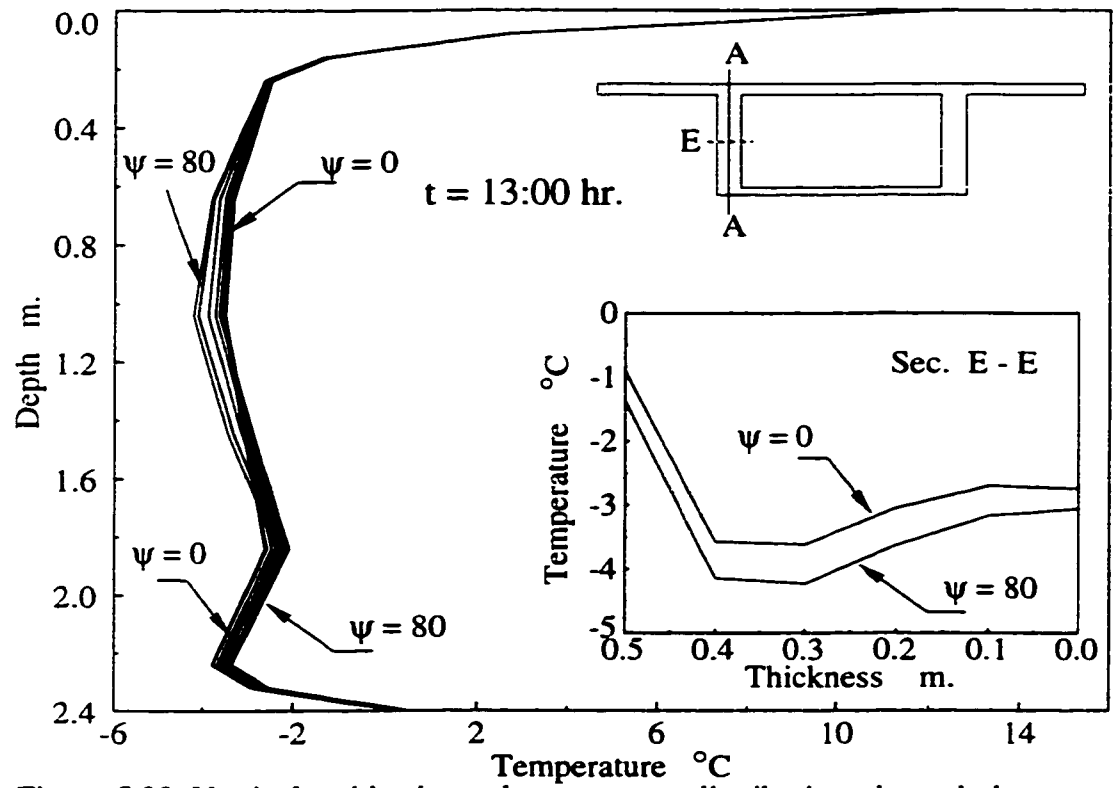

Figure 5.30 Vertical and horizontal temperature distribution through the west web for differentangles, ψ, along the bridge length, Spring conditions.

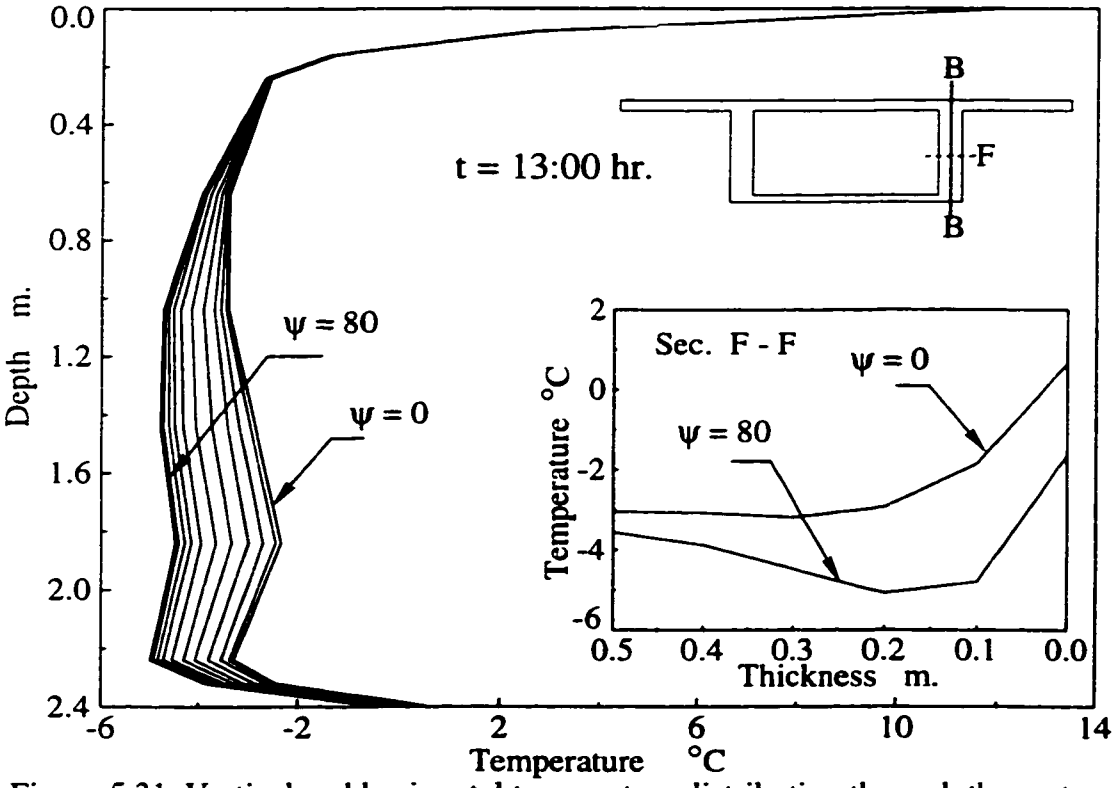

Figure 5.31 Vertical and horizontal temperature distribution through the east web for different angles, ψ, along the bridge length, Spring conditions

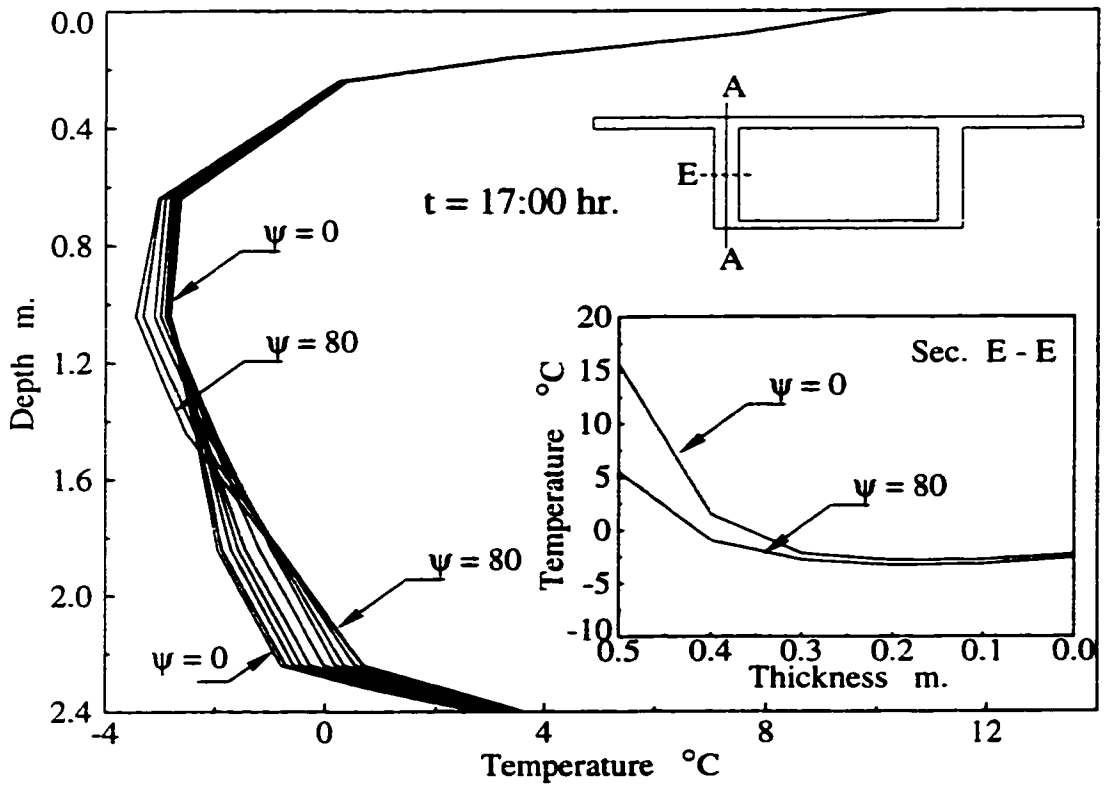

Figure 5.32 Vertical and horizontal temperature distribution through the west web for different angles, ψ, along the bridge length, Spring conditions

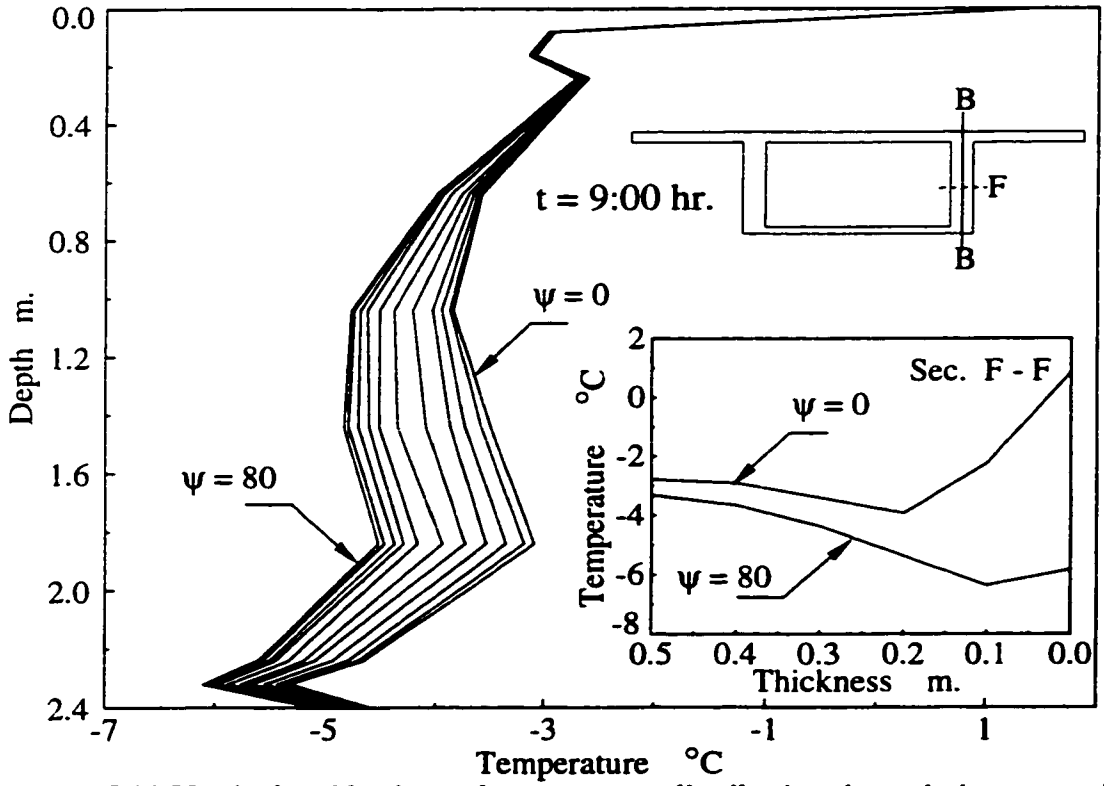

Figure 5.33 Vertical and horizontal temperature distribution through the east web for different angles, ψ, along the bridge length, Spring conditions

tion is due to the difference in solar declination δ for the different days in the year [see Equation (4.23)].

5.6.2 Orientation of the Bridge Axis with respect to the North

Temperature variations produced in a bridge structure are generally influenced by the orientation of the bridge surfaces relative to the sun. This orientation is commonly defined by the direction of the bridge axis relative to the North. For the curved bridge geometry employed herein, the bridge orientation is determined from the direction of the global Y-axis with respect to the North. Therefore, to examine the effect of the bridge orientation, the angle between the global Y-axis, and the North direction (i.e. deviation angle d, see Figure 5.34) is changed in steps of 45° anti-clockwise starting from $d = 0.0$ (Y-axis is parallel to North).

For each orientation, similar graphs to those of Figures 5.9 to 5.14 are plotted and shown in Figures 5.35 to 5.44

Comparison between the effect of different orientations shows that:

1 - The effect of bridge orientation on the temperature variations along the bridge length is very pronounced. A change of temperature can reach up to 44% along the web surface for some orientations, while other orientations cause small effects (see Figures 5.35 and 5.36).

2 - The maximum change in temperature at the outer surface of the bridge web reaches 13 °C. This variation occurs for the case of $d = 0$ (i.e. range of γ between -90 to -170 East, and +10 to +90 West). See Figure 5.1.

3 - Little difference is observed in the vertical and horizontal temperature distribution from one section to another along the bridge axis for various orientations. The maximum difference at the web center line is approximately 2 °C. It is

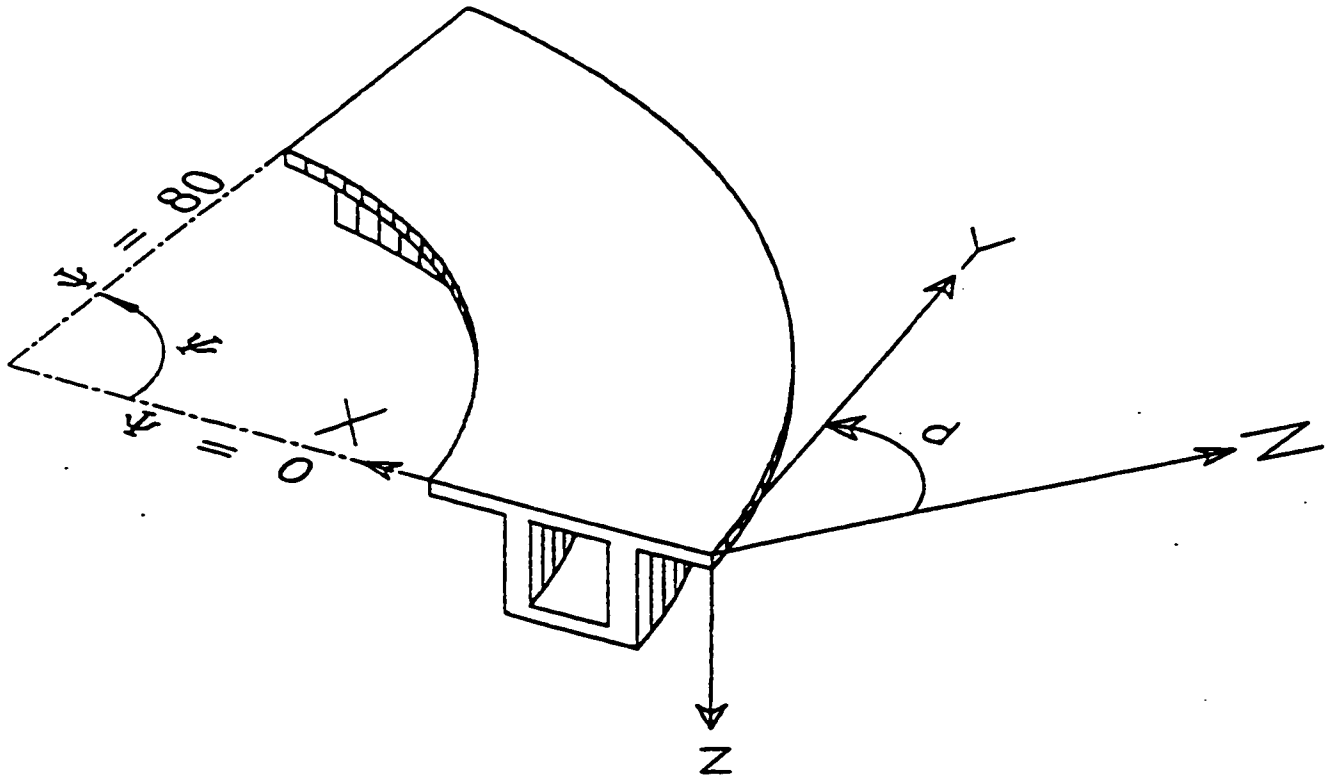

Figure 5.34 Isometeric view showing the different orientations of the bridge axis with respect to the North, and the deviation angle, *d*.

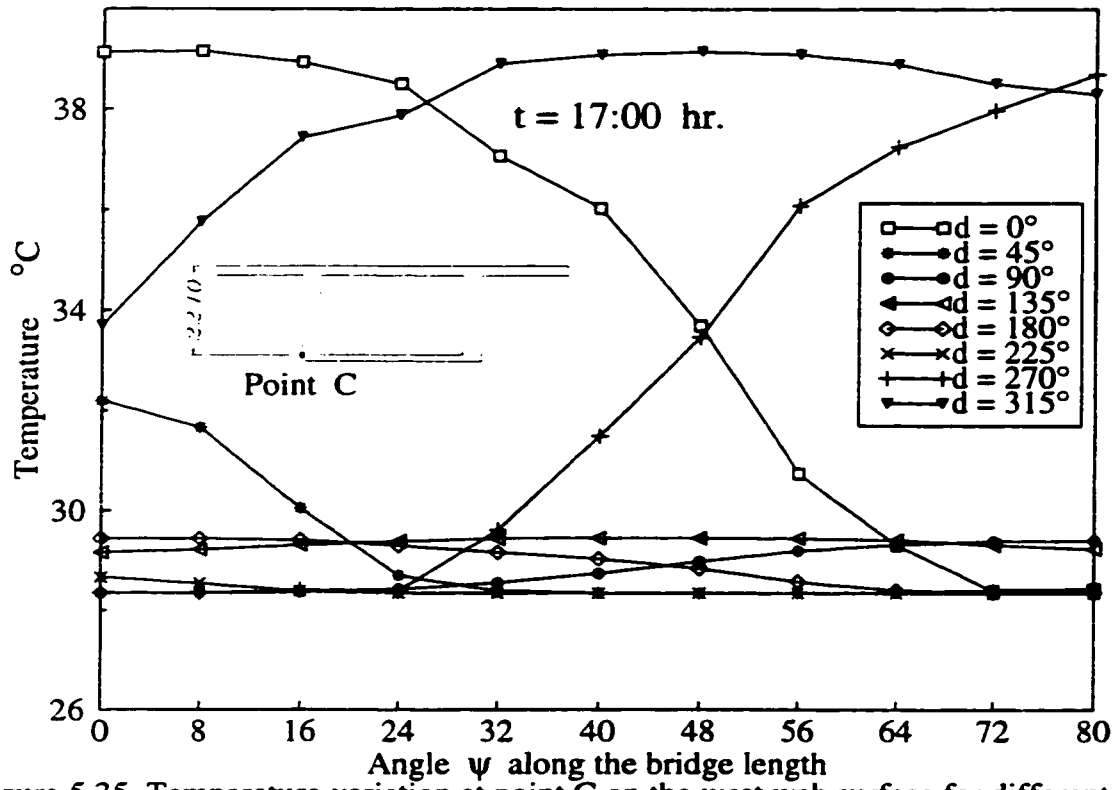

Figure 5.35 Temperature variation at point C on the west web surface for different orientations of the bridge axis towards North direction *d*, Summer conditions.

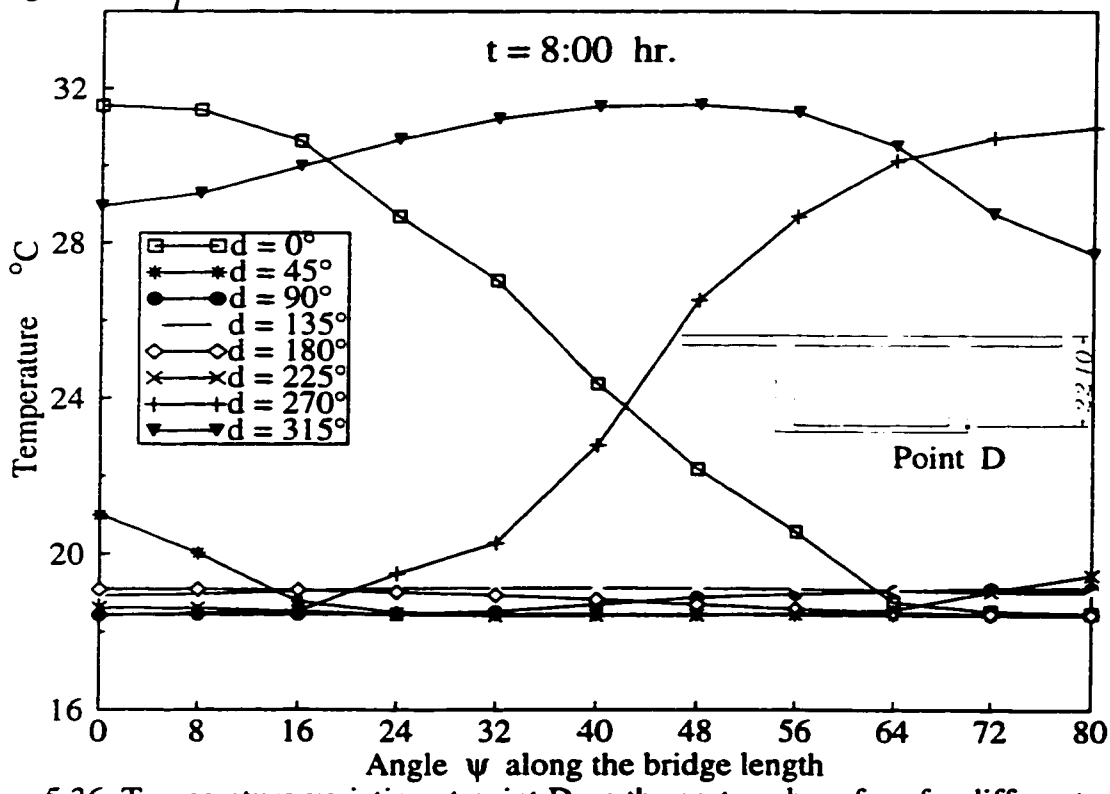

Figure 5.36 Temperature variation at point D on the east web surface for different orientations of the bridge axis towards North direction *d*, Summer conditions.

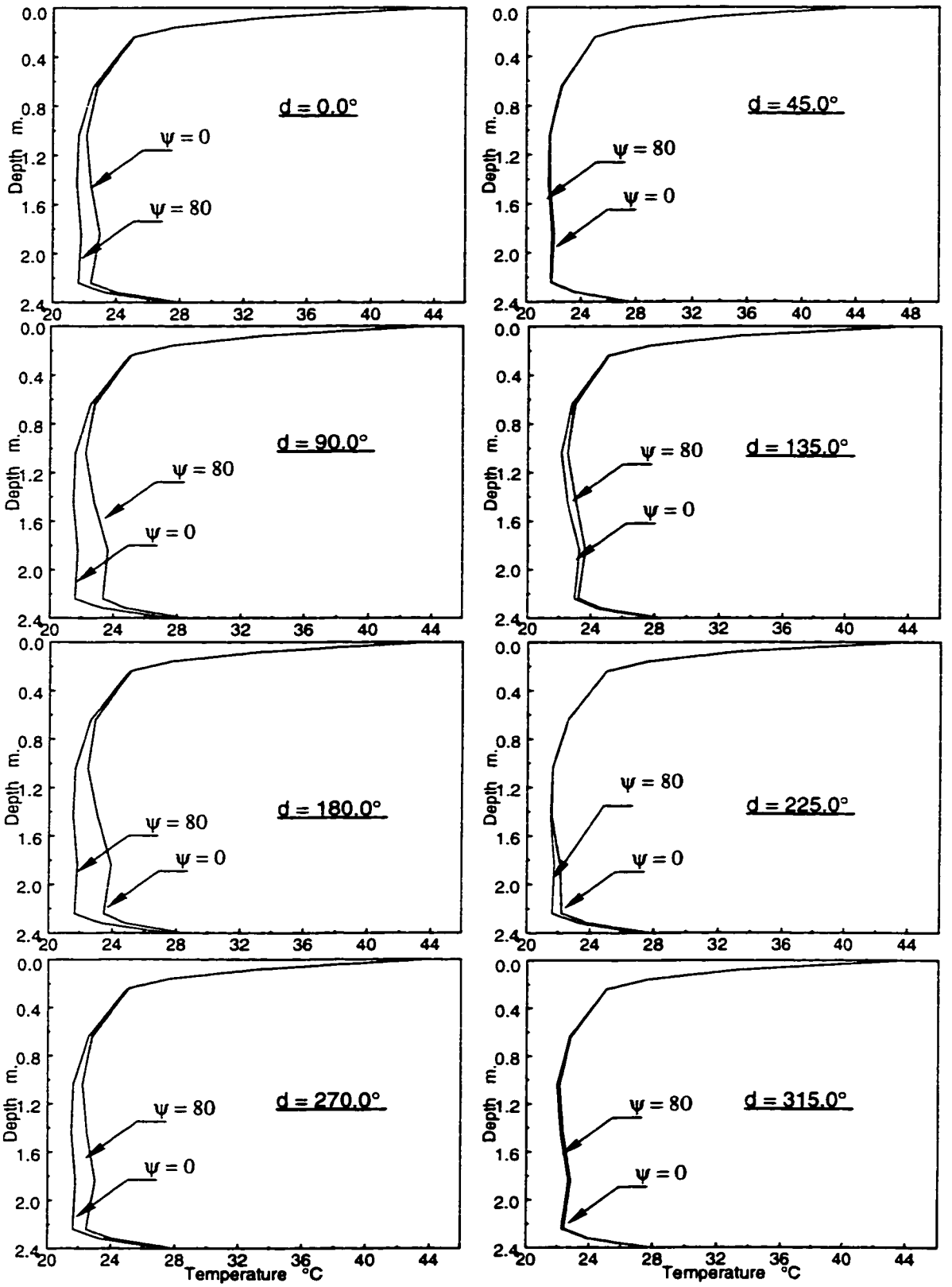

Figure 5.37 Vertical temperature distribution through the west web at the two end sections for different orientations *d*, Summer conditions. t = 13:00 hr.

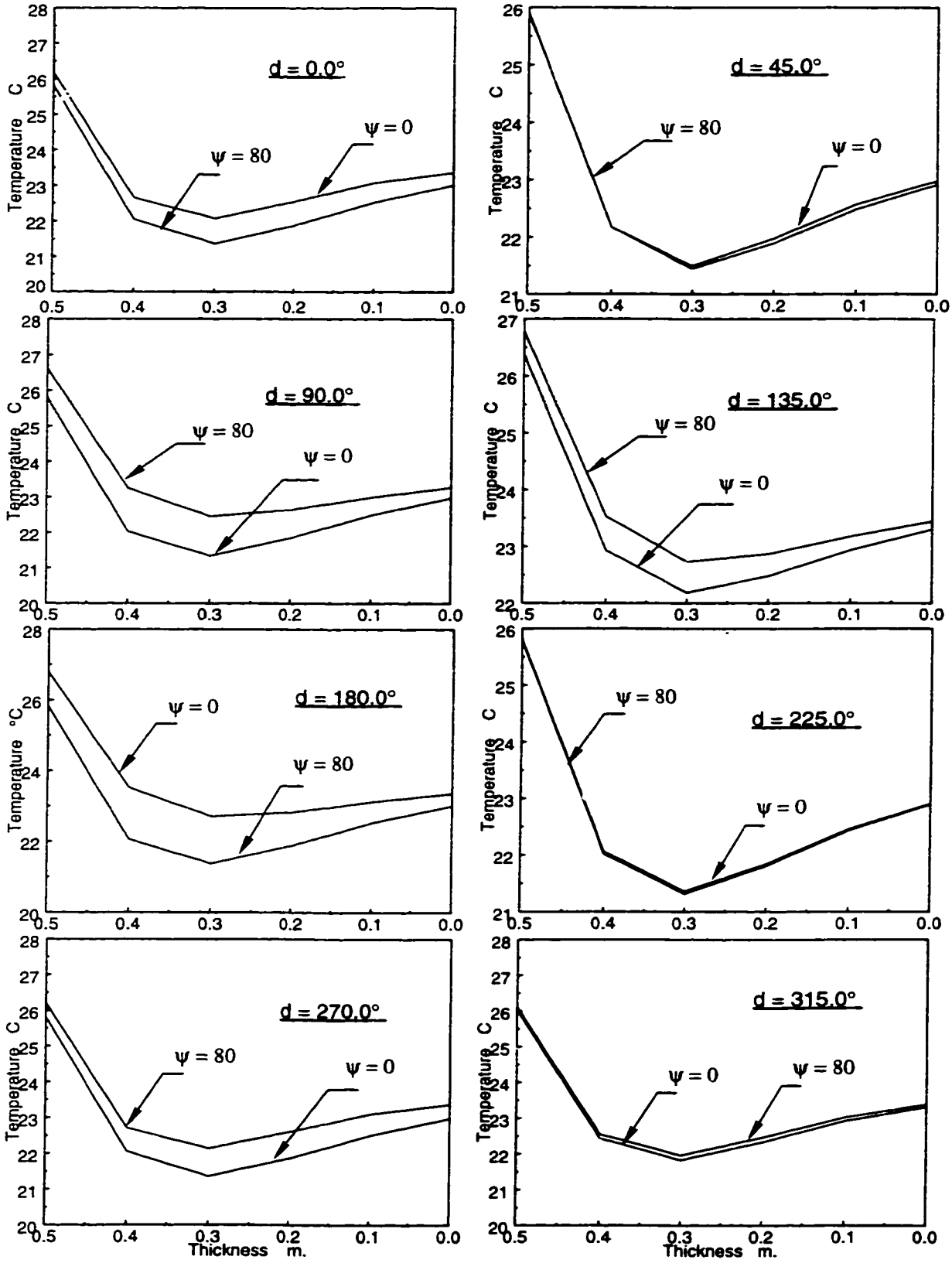

Figure 5.38 Horizontal temperature distribution at the mid height of the west web at the two end sections, for different orientations *d*, Summer conditions. t=13:00

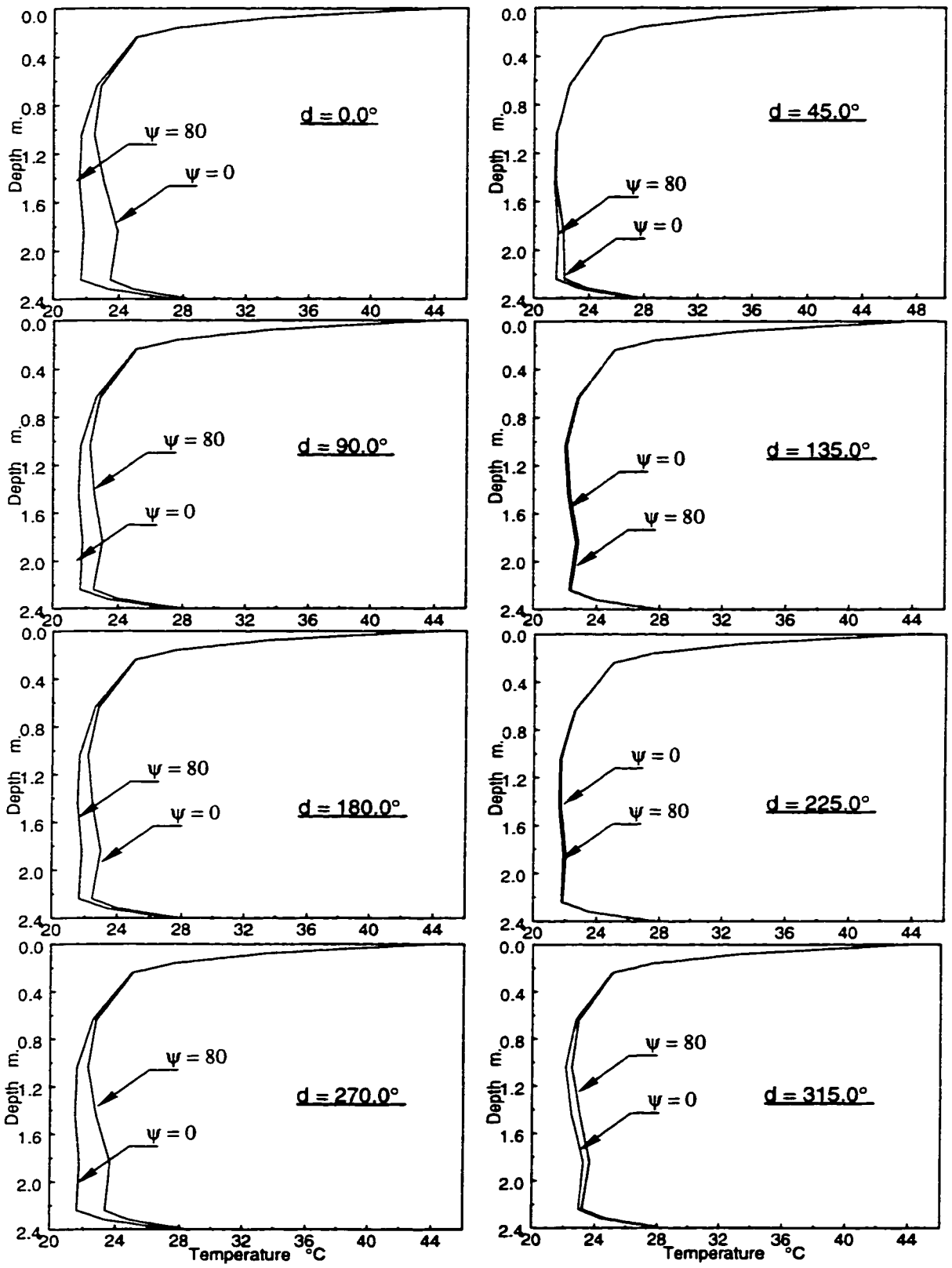

Figure 5.39 Vertical temperature distribution through the east web at the two end sections for different orientations *d*, Summer conditions. t = 13:00 hr.

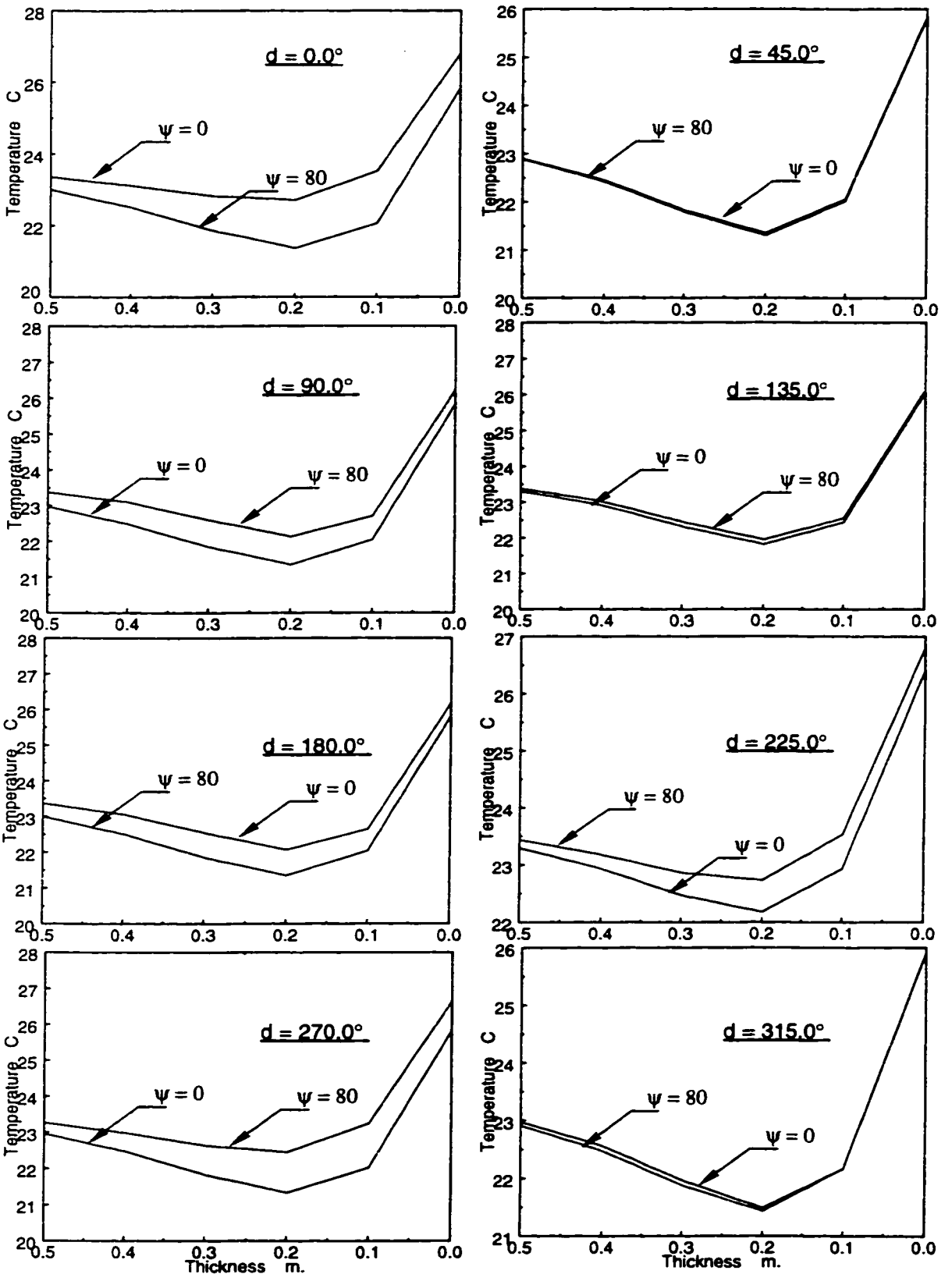

Figure 5.40 Horizontal temperature distribution at the mid height of the east web at the two end sections, for different orientations *d*, Summer conditions. t = 13:00

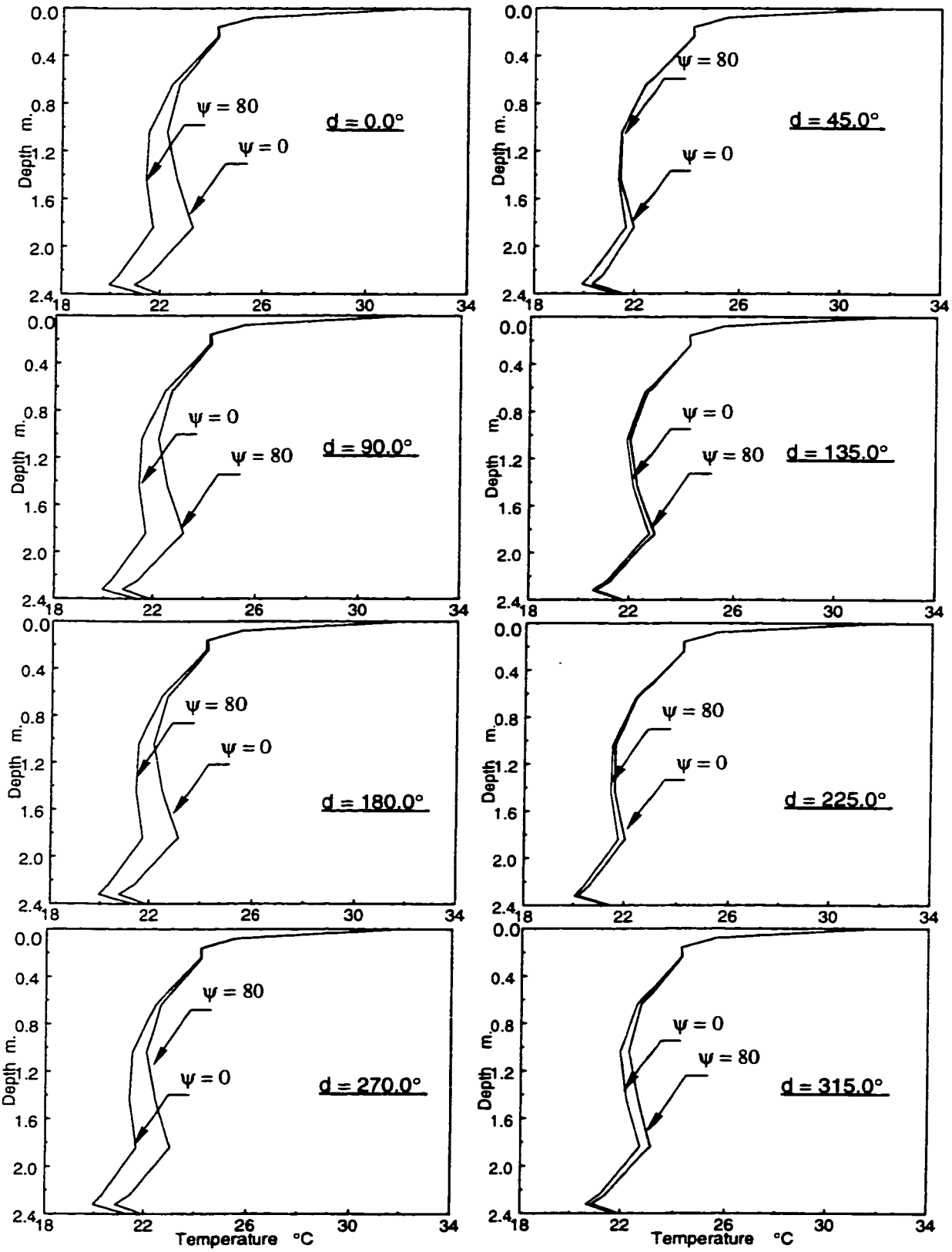

Figure 5.41 Vertical temperature distribution through the east web at the two end sections, for different orientations *d*, Summer conditions. t = 9:00 hr.

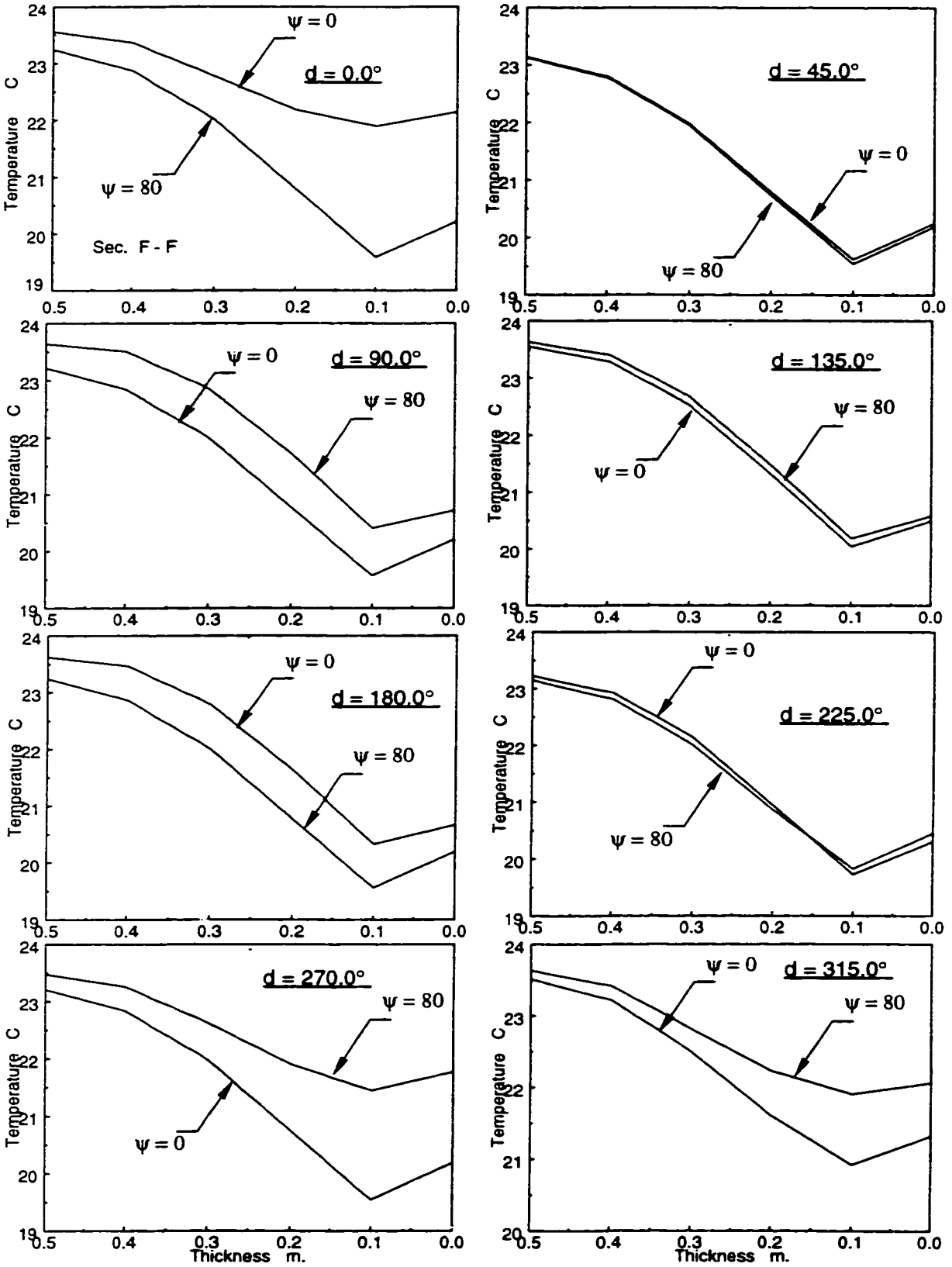

Figure 5.42 Horizontal temperature distribution at the mid height of the east web at the two end sections, for different orientations *d*, Summer conditions. t = 9:00

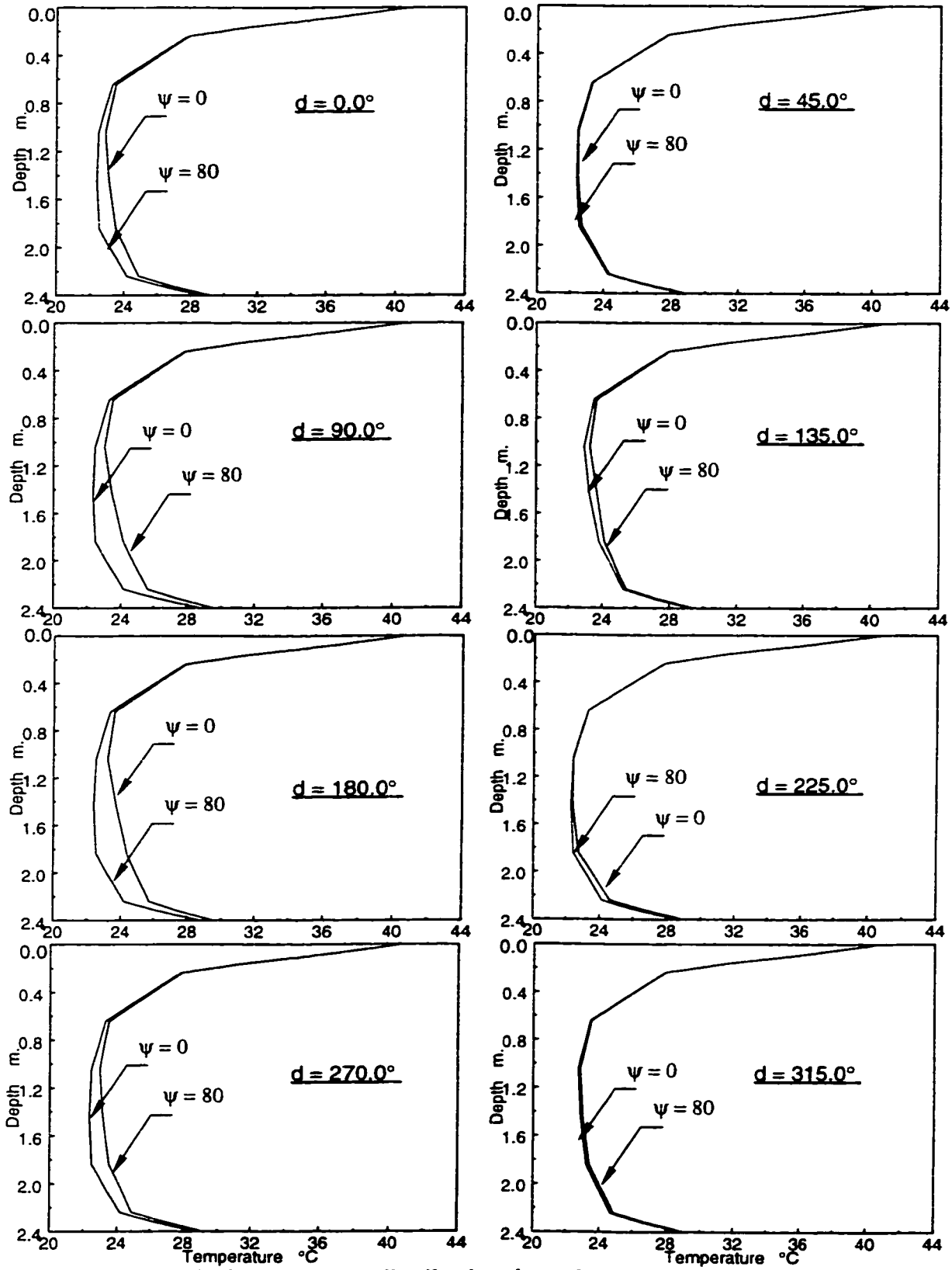

Figure 5.43 Vertical temperature distribution through the west web at the two end sections, for different orientations *d*, Summer conditions. t = 17:00 hr.

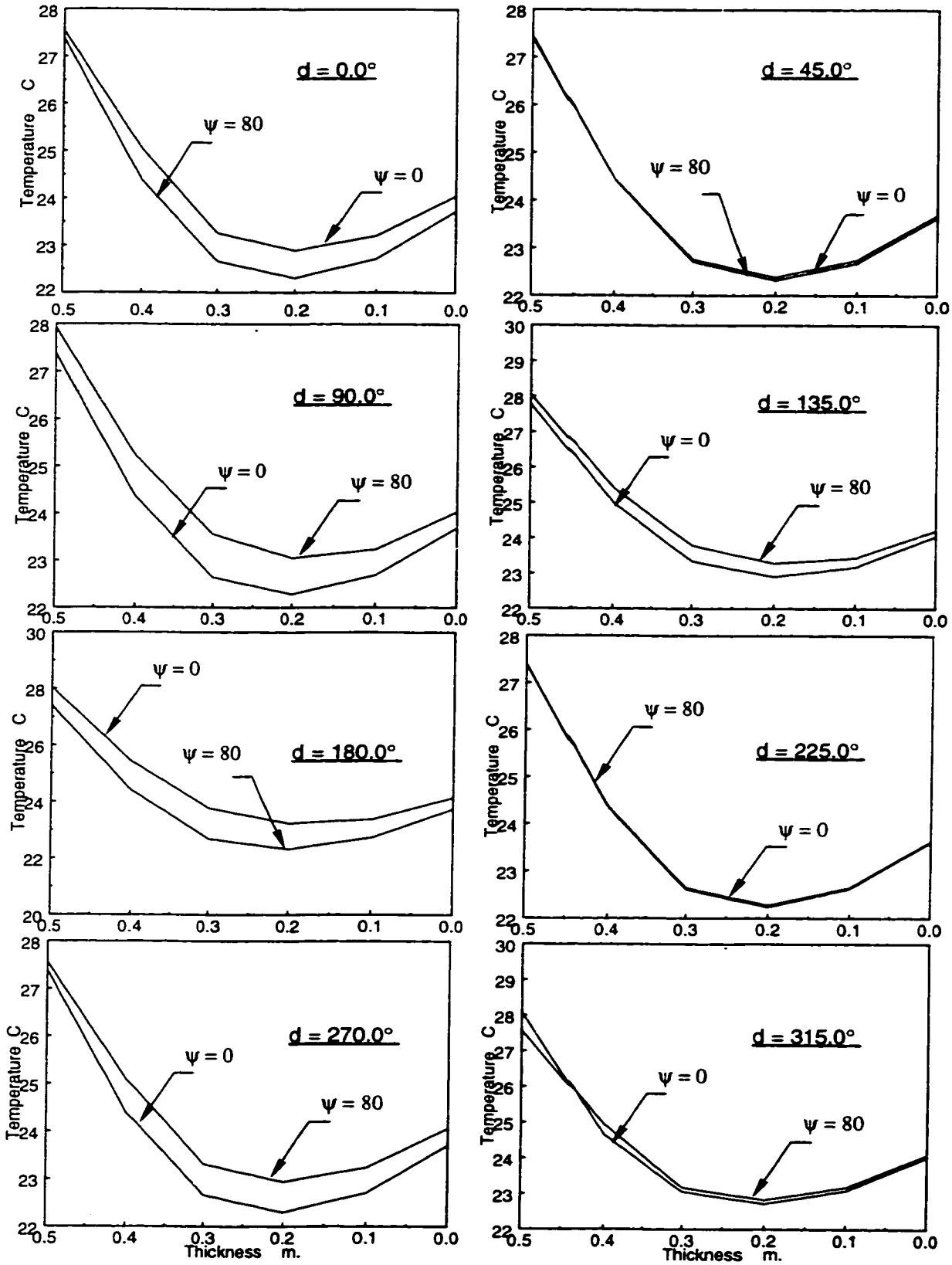

Figure 5.44 Horizontal temperature distribution at the mid height of the west web at the two end sections, for different orientations *d*, Summer conditions. t = 17:00

interesting to note that the orientation of the bridge that causes the largest variation in temperature along the vertical axis of the web, is not the same for the east and the west webs of the cross-section at the same hour of the day (Figures 5.37 and 5.39).

5.6.3 Overhanging Length - Web Depth Ratio (OWR)

In order to investigate the effect of the overhanging length of the top slab on the amount of solar radiation incident on the outer surface of the web and, hence, on the temperature variaiton along the bridge length, the bridge of Figure 5.1 is analyzed considering two other cross-sections having different overhanging lengths, (or in other words, different OWR) as shown in Figure 5.45.

Figures 5.46 to 5.51 and Figures 5.52 to Figure 5.57 depict the variation of temperature along the bridge length for the modified cross-sections having an overhang length of 2.5 m (OWR = 1.15), and 1.5 m (OWR = 0.70), respectively.

Comparison with the reference case, which has an overhang length of 2.0 m (OWR = 0.92), shows that:

1 - As expected, a decrease in the overhang length increases the variation of web surface temperature along the bridge length. This is because the height of the web shaded by the overhang decreases with the decrease of the overhanging length. Nevertheless, the increase in temperature variation due to different cases is small (from 27% for OWR = 1.15 to 30% for OWR = 0.70).

2 - Also, the time of the day at which the maximum variation occurs is different from one case to another, since the web shaded length is different at a given hour of the day for the different cases, based on the overhanging length.

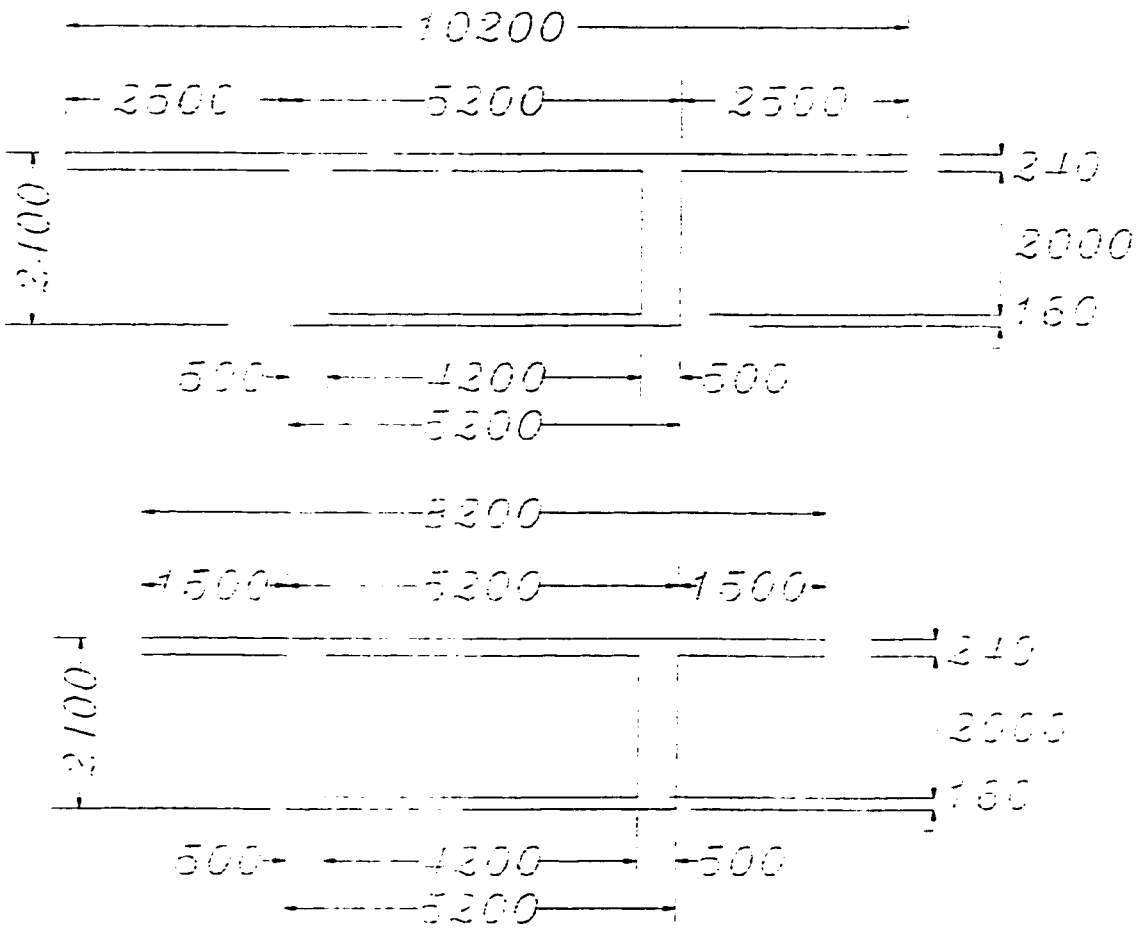

Figure 5.45 Dimensions of the two cross-sections with different overhanging length

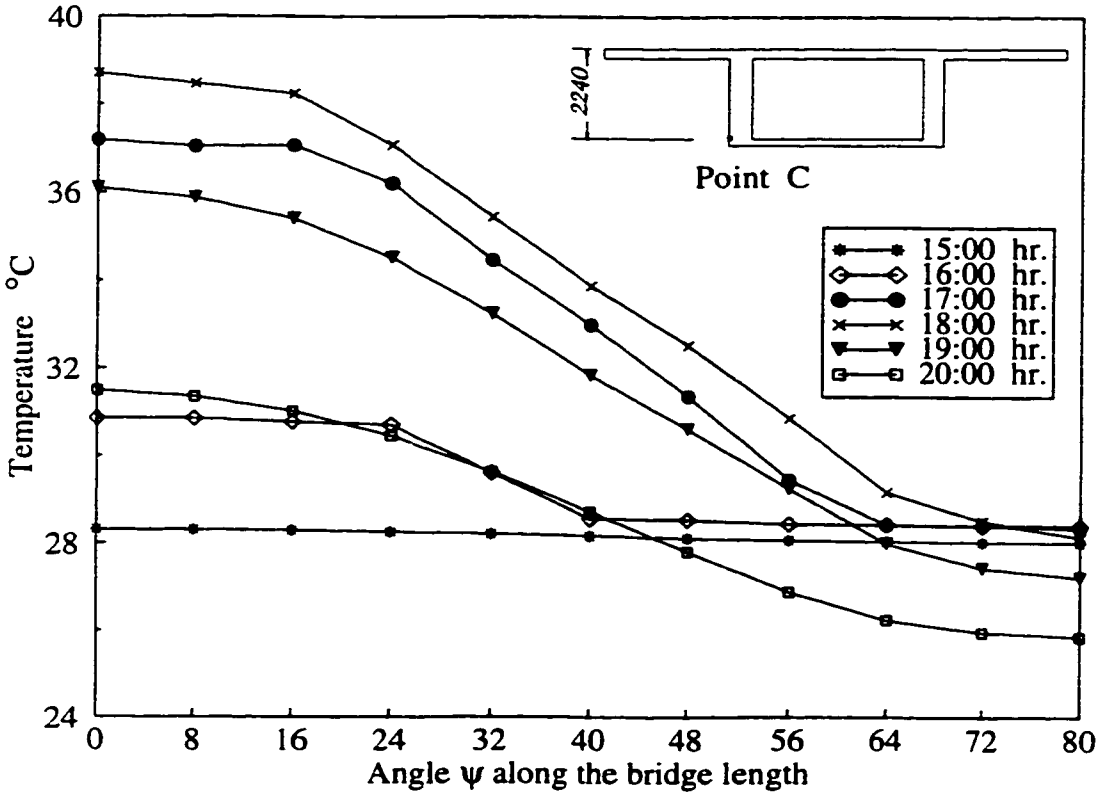

Figure 5.46 Longitudinal variation of temperature at point C on the west web surface, OWR = 1.15.

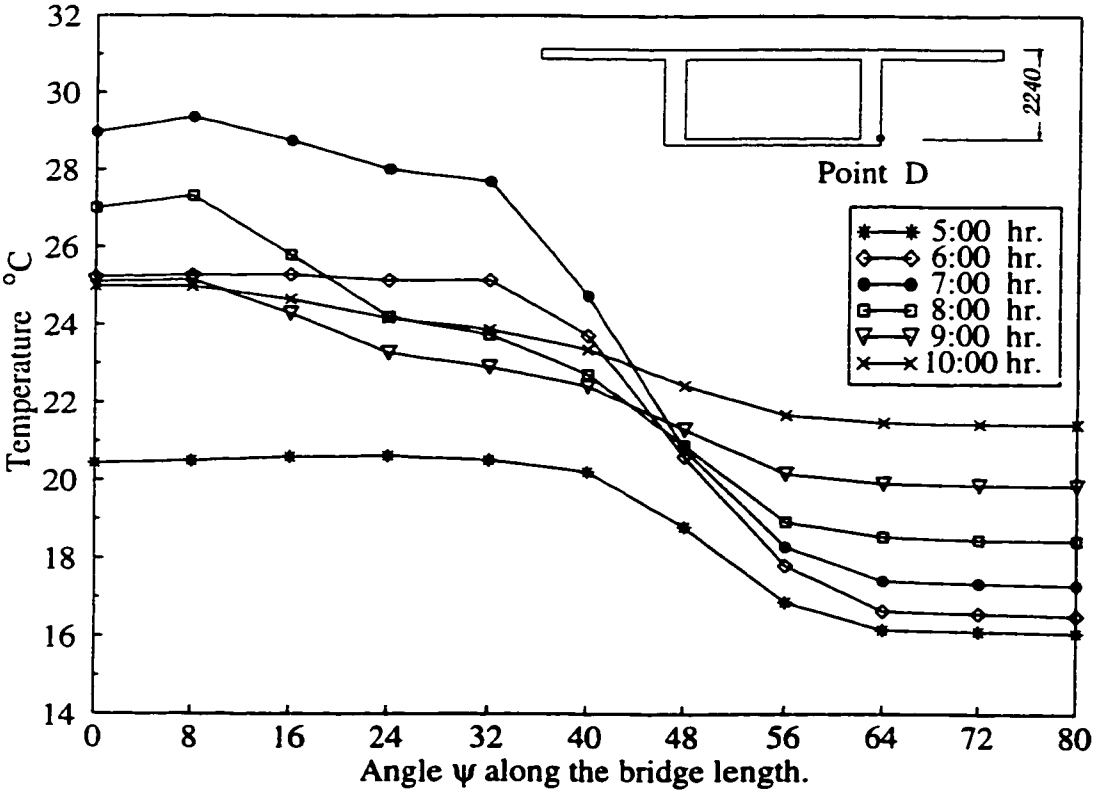

Figure 5.47 Longitudinal variation of temperature at point D on the east web surface, OWR = 1.15.

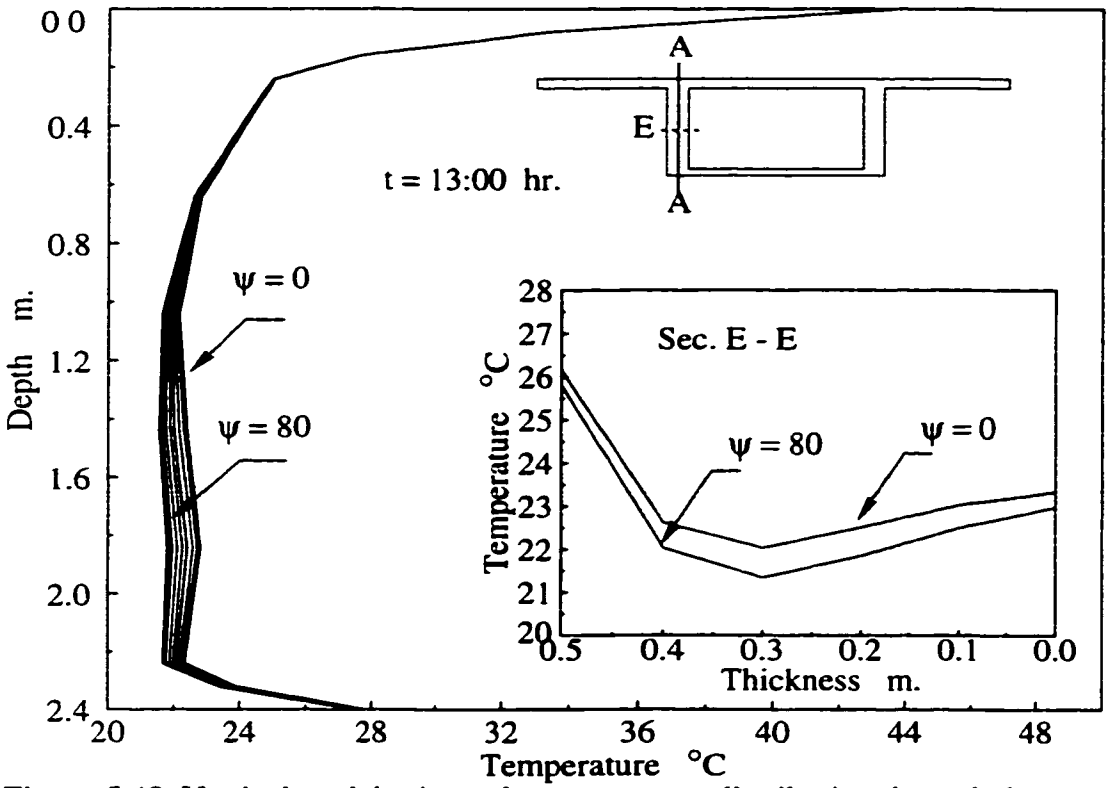

Figure 5.48 Vertical and horizontal temperature distribution through the west web for different angles ψ, along the bridge length, t = 13:00 hr., OWR = 1.15.

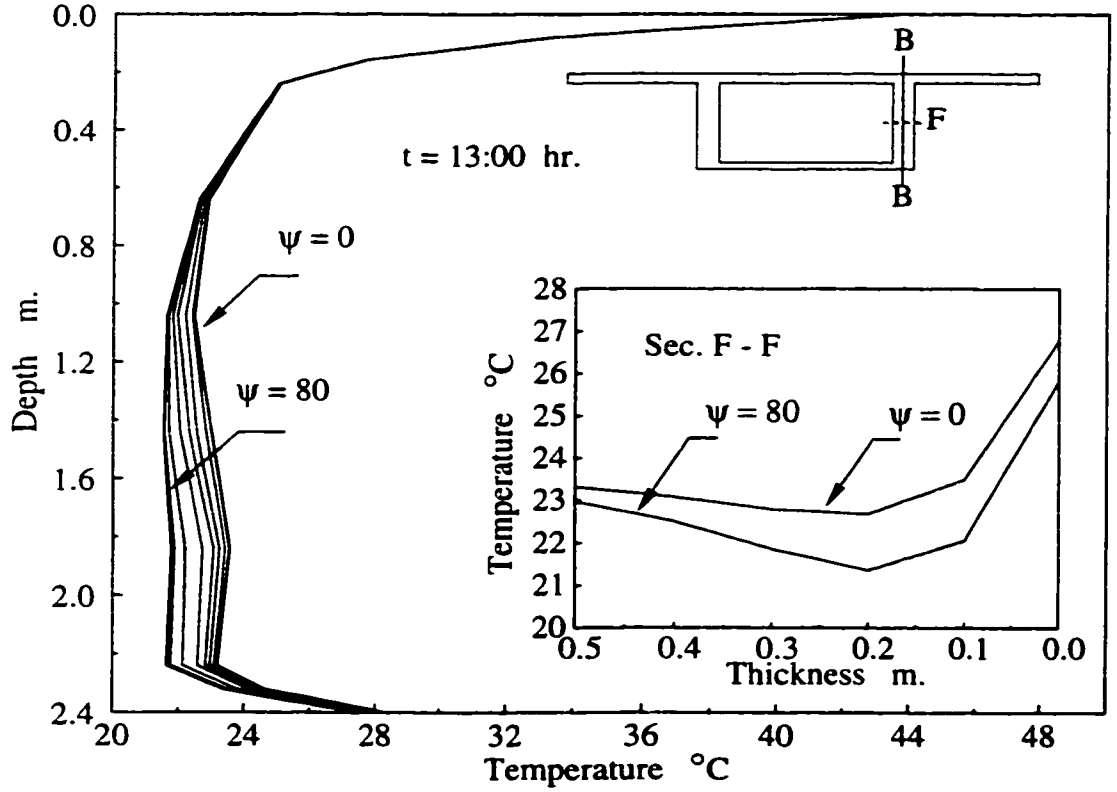

Figure 5.49 Vertical and horizontal temperature distribution through the east web for different angles ψ, along the bridge length, t = 13:00 hr, OWR = 1.15.

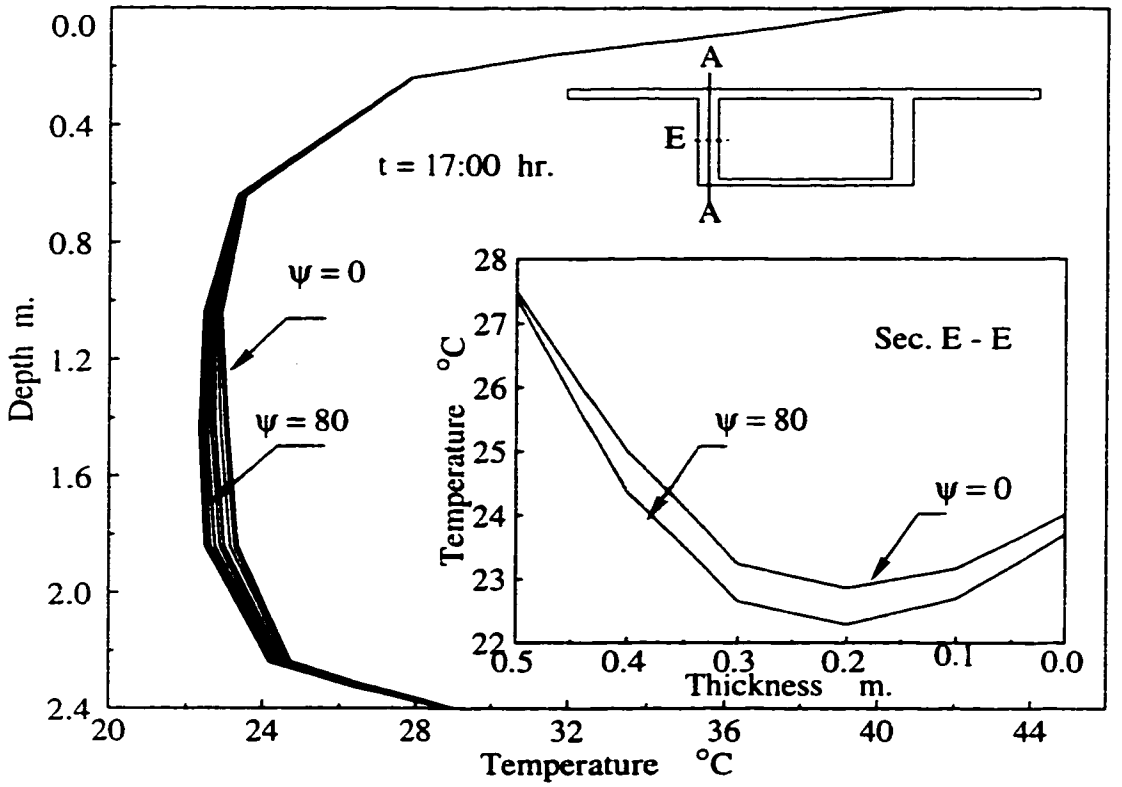

Figure 5.50 Vertical and horizontal temperature distribution through the west web for different angles ψ, along the bridge length, t = 17:00 hr.,OWR = 1.15.

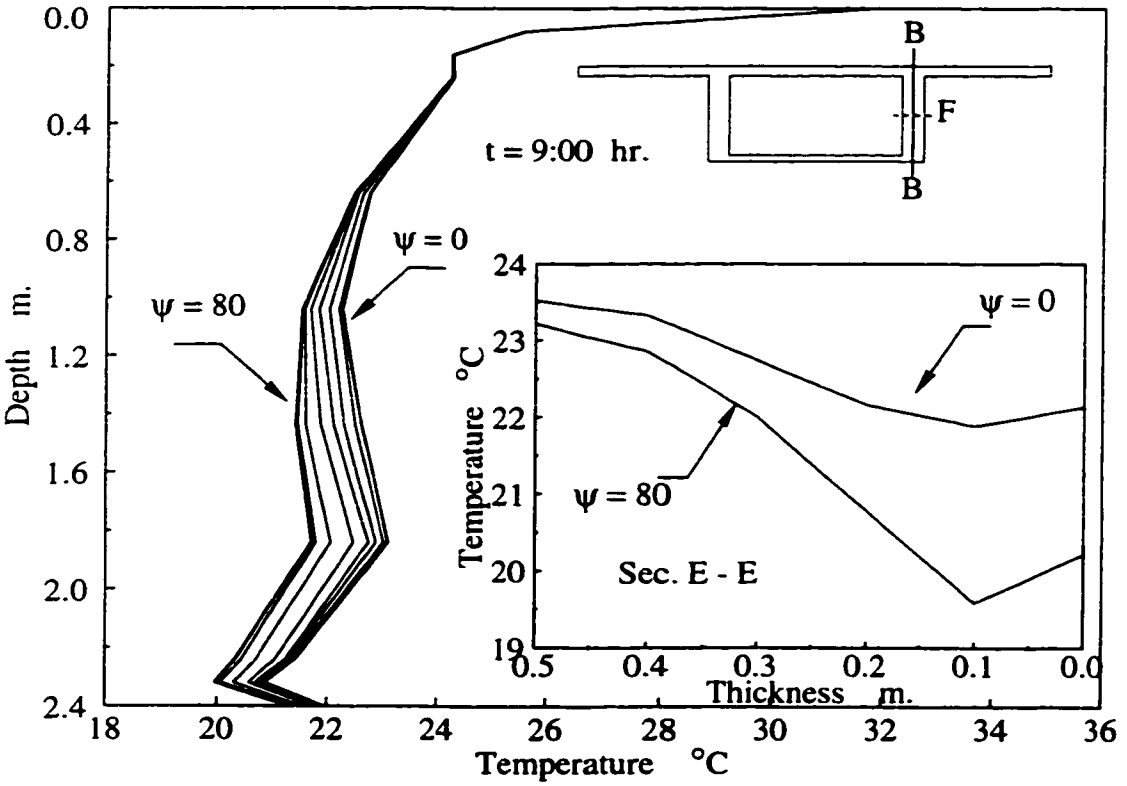

Figure 5.51 Vertical and horizontal temperature distribution through the east web for different angles ψ, along the bridge length, t = 9:00 hr., OWR = 1.15.

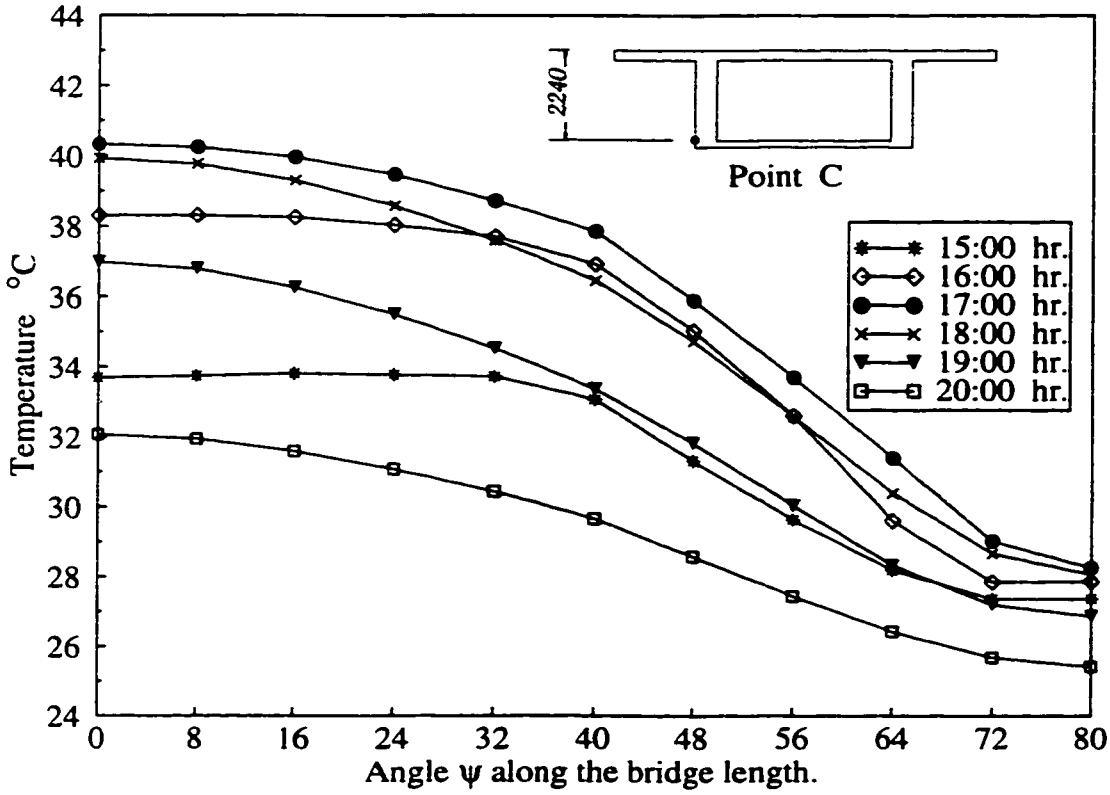

Figure 5.52 Longitudinal variation of temperature at point C on the west web surface, OWR = 0.70.

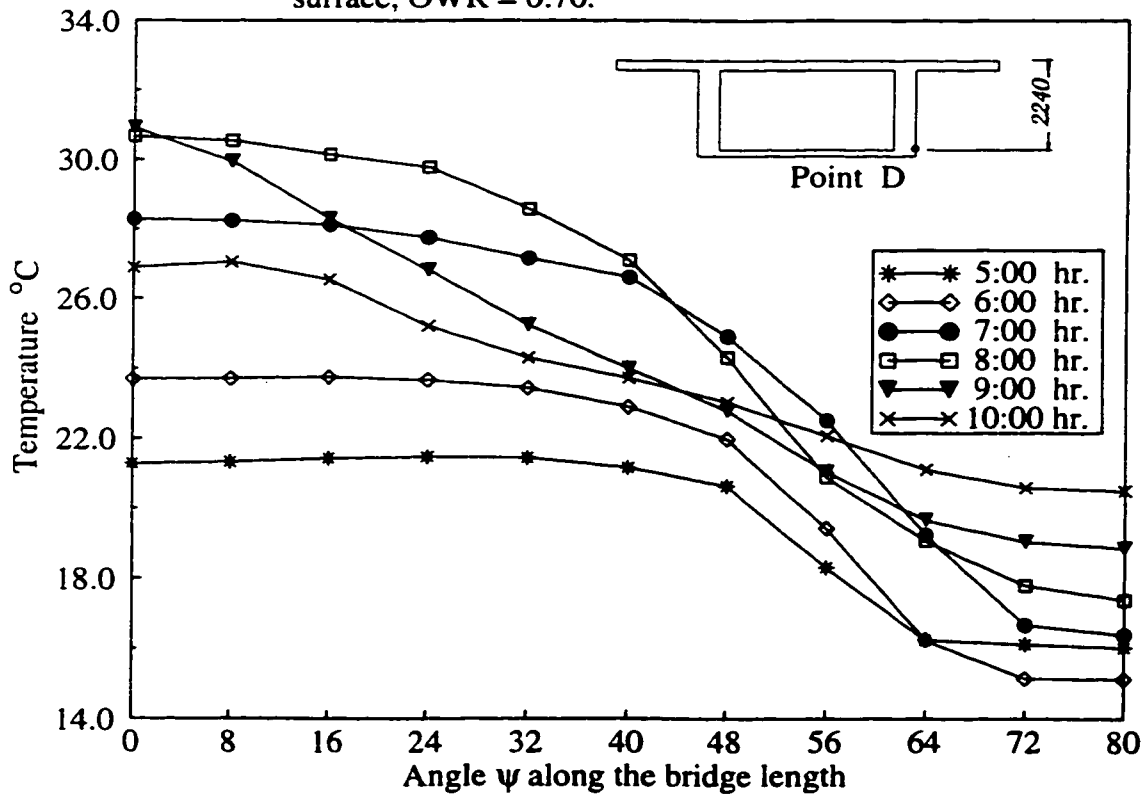

Figure 5.53 Longitudinal variation of temperature at point D on the east web surface, OWR = 0.70.

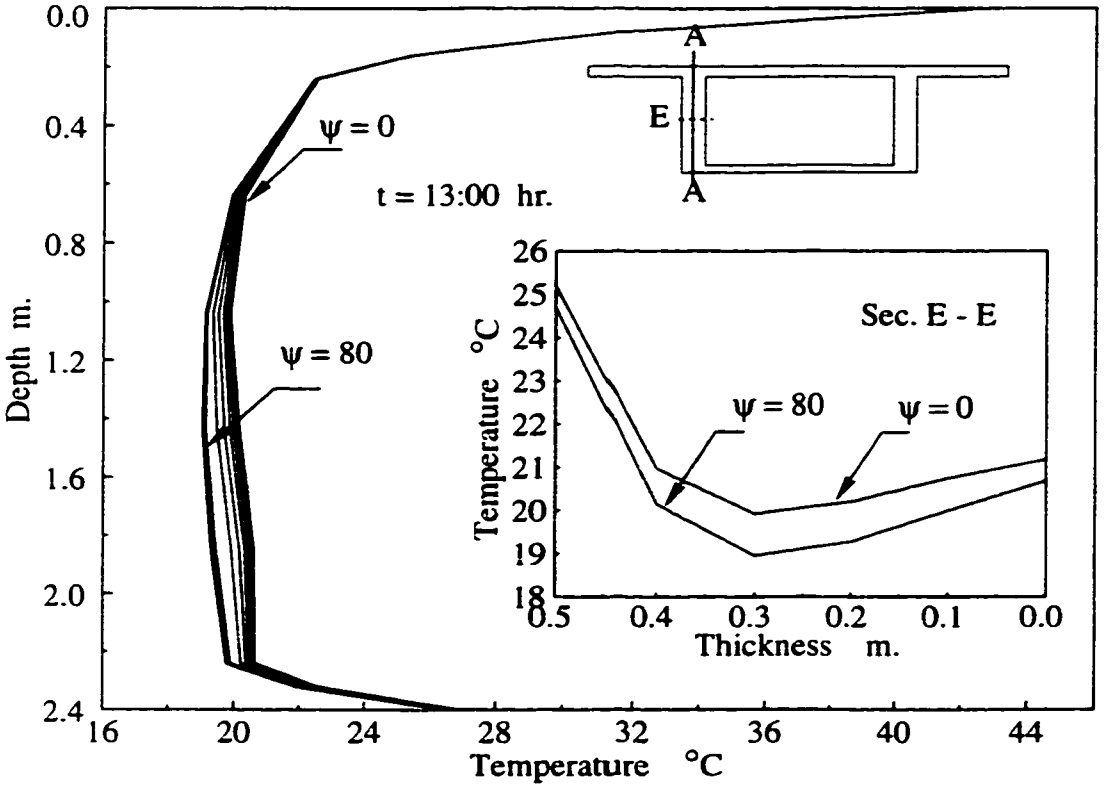

Figure 5.54 Vertical and horizontal temperature distribution through the west web for different angles ψ, along the bridge length,t = 13:00 hr, OWR = 0.70.

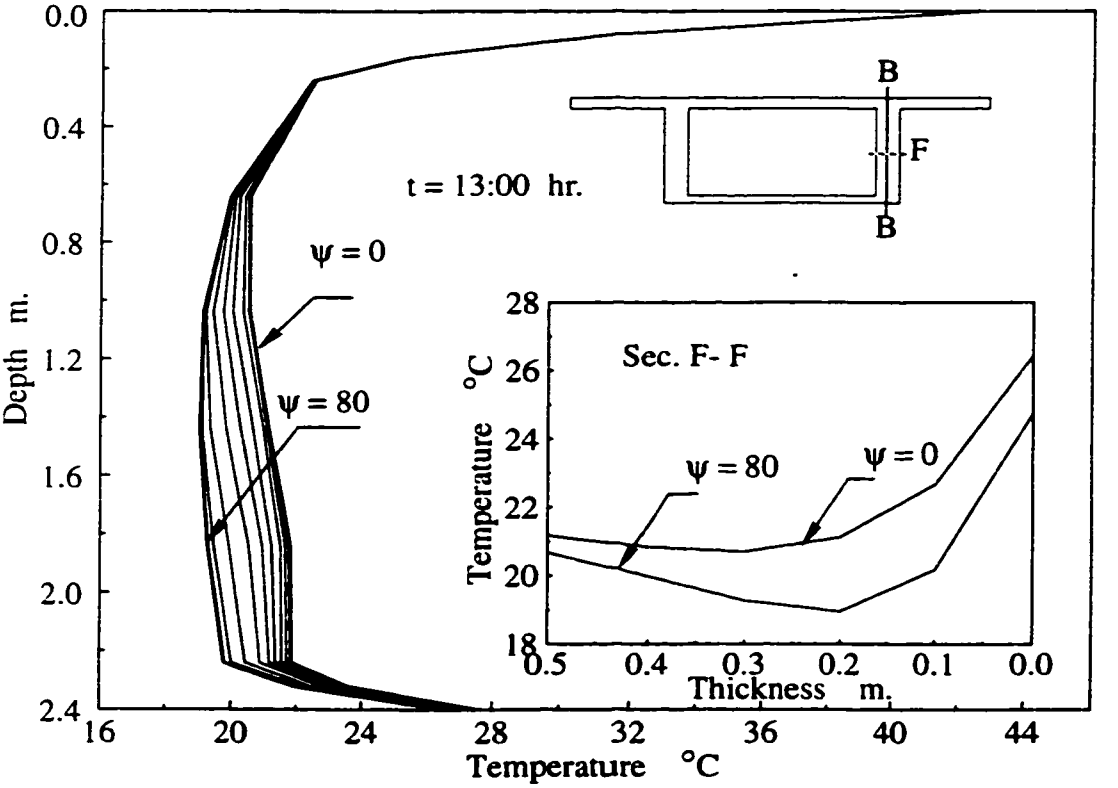

Figure 5.55 Vertical and horizontal temperature distribution through the east web for different angles ψ, along the bridge length, t = 13:00 hr.,OWR = 0.70.

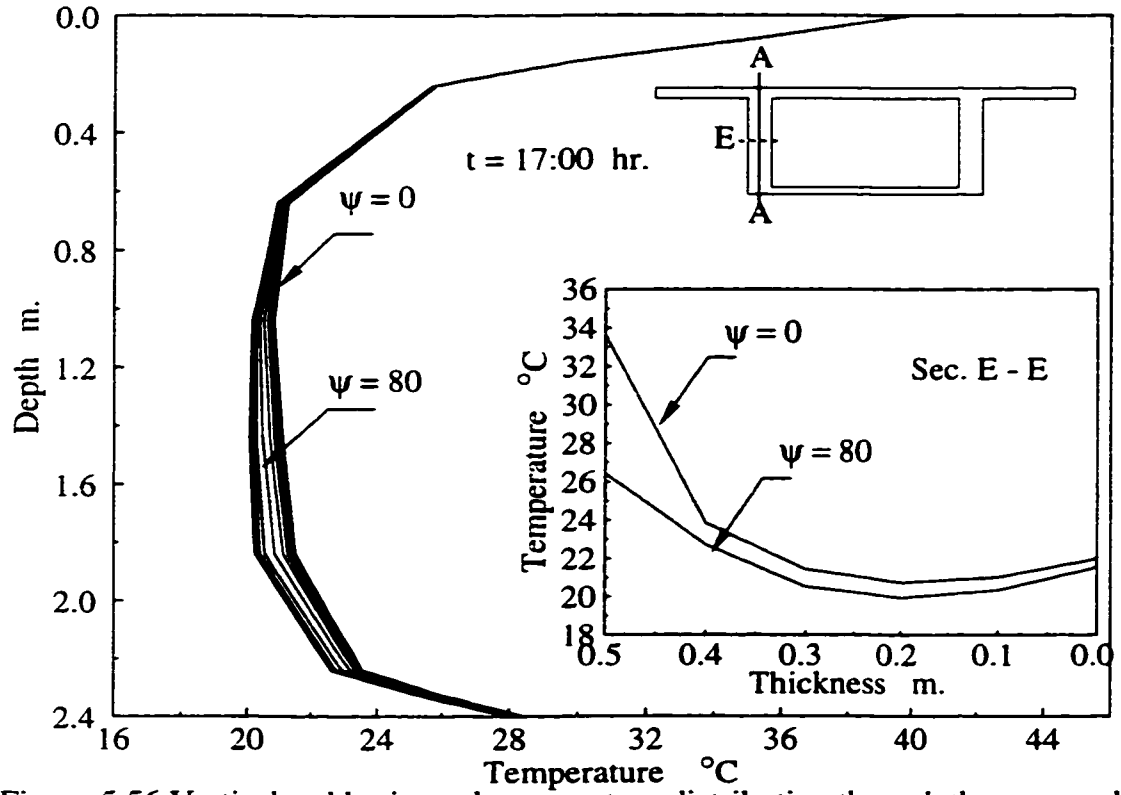

Figure 5.56 Vertical and horizontal temperature distribution through the west web for different angles ψ, along the bridge length, t = 17:00 hr., OWR = 0.70.

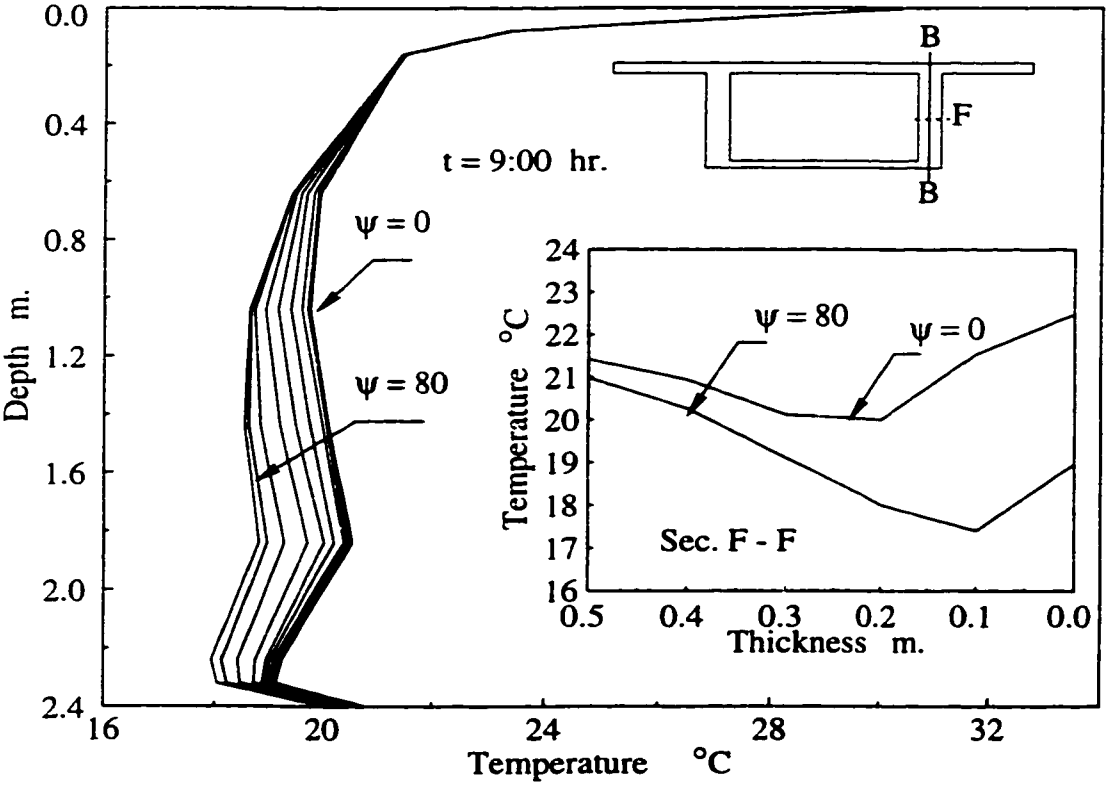

Figure 5.57 Vertical and horizontall temperature distribution through the east web for different angles ψ, along the bridge length, t = 9:00 hr , OWR = 0.70.

3 - The variation of horizontal temperature distribution through the mid height of the web along the bridge length is increased from approximately 8% for the case of OWR = 1.15 to approximately 13% for the case of OWR = 0.70 (see Figure 5.50 and 5.56). No noticeable change is observed in the vertical temperature distribution along the bridge length in all cases.

CHAPTER 6
SUMMARY, CONCLUSIONS AND RECOMMENDATIONS

6.1 Summary

A numerical model and a computer program based on the three-dimensional finite element method were developed to determine the transient temperature distribution and the corresponding stresses produced in box girder bridges of arbitrary plan and cross-section geometry due to the environmental conditions. A variational principle is used to solve the heat flow governing differential equation in the space variables. Two types of elements are used in the program: 20-node isoparametric solid element to model the heat conduction within the body; and a fictitious surface 8-node isoparametric element to simulate the interaction between the body and the environment. Time-varying environmental conditions of ambient air temperature and solar radiation are modelled mathematically by equations with variable coefficients which are input to the computer program. The solution of the first order differential equations that govern the variation of temperature with time is accomplished by using a time stepping technique employing Galerkin's weighted residual method. The resulting temperature distribution at a given time is used to compute the induced stresses in the body by employing 20-node solid elements.

Verification problems are conducted to examine the program developed. Comparison with exact solutions, other well-known finite element programs, as well as field measurements are provided to check the ability of the program to model the heat flow and the induced stresses due to different types of boundary conditions.

The computer program is employed in a case study to examine the significance of temper-

ature variations developed along the length of curved concrete box girder bridge located in Calgary, Canada. The influence of the season of the year, the orientation of the bridge axis with respect to the North, and the overhanging length-web depth ratio on the temperature distribution developed along the bridge axis are investigated.

6.2 Conclusions

Application of the described model and the computer program on a curved concrete box girder bridge leads to the following conclusions:

1 - The study showed significant temperature variations along the axis of concrete bridge structures curved in plan, in addition to the well-known temperature variations within the cross-section. Therefore, three-dimensional analysis is necessary to predict the temperature distribution within bridges of this type.

2 - Although the study was conducted for a curved concrete box girder bridge of one cell, the necessity of three-dimensional temperature analysis is deemed necessary for other types of curved bridges (i.e. multi-cell and composite bridges). This conclusion is based on the fact that variation of temperature along the axis of the curved bridges is caused by the change of the solar radiation received by the surface of the webs of the box girder. This variation of solar radiation results from the difference of the surface azimuth angle, γ, from one section to another along the bridge length.

3 - The study reveals that using a coarse mesh of up to 8 degrees along the bridge length (i.e. $\psi = 8$), would be sufficient to predict the temperature variation with good accuracy. However, a finer mesh is required to find the stresses induced in the bridge structure to a reasonable accuracy.

4 - Analysis of the given bridge geometry for the temperature prediction indicates that, among the different parameters studied in the current investigation, the following was found.

a) The variation of temperature along the bridge length basically occurs in the layers close to the surface of the web and decreases towards the box. However, this variation is not pronounced during all hours of the day. Only certain locations at certain times along the bridge geometry would have such variation. The largest variation at the surface occurs in the Spring season, and can be as large as 14 °C.

b) The variation of temperature distribution through the vertical axis of the web from one section to another along the bridge length is less significant in most times of the year, except in Winter conditions, where it can reach a difference of 5 °C (25%).

c) The orientation of the bridge axis with respect to the North is of great importance to the development of temperature variations along the bridge length. When most of the bridge web surface is facing more or less the East - West direction, large of temperature occurs. However, other orientations of the web surface of a curved bridge produce less, or negligible, variations in temperature. The largest temperature variations occur when the surface azimuth angle, γ, varies between -90 to -170 East and +10 to +90 West.

d) The effect of the overhanging length to web depth ratio does produce a slight difference in the temperature distribution along the bridge length. Forty percent difference in the overhanging length to web depth ratio can produce a difference of 3 percent in the longitudinal temperature variation at the outer surface of the bridge web.

6.3 Recommendations

The present research is the first step towards a three-dimensional thermal analysis of curved concrete box girder bridges. Results obtained for temperature values showed significant variations along the bridge length. Further investigations are required to determine the magnitude of the resulting stresses induced in the bridge for structural design purposes. Also, the calculation of thermal stresses due to the various influencing parameters will assist in determining the critical temperature distribution that develops over a bridge structure. In the stress calculation, special attention should be given to the mesh size.

For more information pertaining to the thermal behavior of curved concrete box girder bridges, the following studies are deemed necessary:

1 - More parameters regarding the temperature variations within curved bridges should be studied to quantify the influence of such parameters on the temperature distribution. Superstructure depth, curvature of the bridge geometry, and thickness of the web, are suggested to be included and examined in future parametric studies.

2 - Stresses caused by creep, shrinkage, and heat of hydration should be studied in conjunction with environmentally induced stresses in concrete bridges. This combination of stresses may severely affect the serviceability of the bridge structures.

Further enhancement can be made in the computer program developed to extend its capabilities and to make it more efficient.

3 - A library of elements can be added to the program. The library will increase the capability of the program to model different applications with much ease

4 - Preprocessing and Postprocessing capability can be incorporated into the program to facilitate the mesh generation and thermal contour plotting.

REFERENCES

"ADINA-T", a finite element program for Automated Dynamic Incremental Nonlinear Analysis of Temperatures. ADINA R & D Inc., Watertown, MA., USA (1992).

Afedes, "Le Rayonnement Solairem au Sol et ses Mesures.", Association Française pour l'étude et le développement des applications de l'énergie solaire, Énergies Nouvelles, No 1, Paris (1974).

Barber, E. S., "Calculation of Maximum Pavement Temperatures from Weather Reports." Highway Research Board Bulletin (1957).

Bathe, K. J., "Finite Element Procedures in Engineering Analysis.", Prentice Hall Inc., New Jersey (1982).

Branco, F., and Mendes, P., "Thermal Actions for Concrete Bridge Design.", Journal of the Structural Engineering, Proceedings of the ASCE, Vol. 119, No. 8, pp. 2313-2331 (August 1993).

Carslaw, H. S., and Jaeger, J. C., "Conduction of Heat in Solids.", 2nd ed., Clarendon Press, Oxford, England (1959).

Chandrupatla, T. R., and Belegundu, A. D., "Introduction to Finite Elements in Engineering.", Prentice Hall Inc., New Jersey (1991).

Clark, H., "Evaluation of Thermal Stresses in a Concrete Box Girder Bridge.", Ph.D. University of Washington, 261 p. (1989).

Cook, R. D., "Concepts and Applications of Finite Element Analysis.", 2nd. Edition, John Wiley & Sons, New York (1981).

Dilger, W. H., Ghali, A., Chan, M., Cheung, M. S., and Maes, M., "Temperature Stresses in Composite Box Girder Bridges.", Journal of the Structural Engineering, Proceedings of the ASCE, Vol. 109, No. 6, pp. 1460-1478 (June 1983).

Dilger, W. H., and Ghali, A., "Temperature-Induced Stresses in Composite Box-Girder Bridges.", Research Report Submitted to the Department of Supplies and Services, Ottawa (October 1980).

Duffie, J. A., and Beckman, W. A., "Solar Engineering of Thermal Processes.", 2nd edition, John Wiley & Sons, New York (1991).

El-Alam, P., and Massicotte, B., "Gradients Thermiques de Conception Pour le Pont de Grand-Mère.", Rapport No. EPM/GCS-1994-01, Département de Génie Civil, Section Structures, École Polytechnique, Montréal, Canada (1994).

Elbadry, M. M., "Thermal Response of Concrete Box Girders Bridges.", M.Sc. Thesis, Department of Civil Engineering, The University of Calgary, Calgary, Alberta (1982).

Elbadry, M. M., and Ghali, A., "User's Manual and Computer Program FETAB: Finite Element Thermal Analysis of Bridges.", Research Report No. CE82-10, Department of Civil Engineering, The University of Calgary, Calgary, Alberta (1982).

Elbadry, M. M., and Ghali, A., "Temperature Variations in Concrete Bridges.", Journal of Structural Engineering, Proceedings of the ASCE, Vol. 109, No. 10, pp. 2355-2374 (1983a).

Elbadry, M. M., and Ghali, A., "Nonlinear Temperature Distribution and its Effects on Bridges.", IABSE Periodica, No. P66/83, pp. 169-191 (1983b).

Emerson, M., "Bridge Temperature for Setting Bearings and Expansions Joints." TRRL Supplementary Report, No. 479, Department of the Environment, Department of Transport, Crowthorne, Berkshire, England (1979).

Emerson, M., "The Calculation of the Distribution of Temperature in Bridges." TRRL Laboratory Report 561, Department of the Environment, Crowthorne, Berkshire, England (1973).

Fu, H., Ng, S., and Cheung, M., "Thermal Behavior of Composite Bridges.", Journal of Structural Engineering, Proceedings of the ASCE, Vol. 116, No. 12, pp. 3302-3323 (1990).

Ghali, A., and Neville, A.M., "Structural Analysis - A Unified Classical and Matrix Approach", Chapman and Hall, London - New York (1989).

Ghali, A., Favre, R., "Concrete Structures; Stresses and Deformations.", Chapman and Hall, London - New York (1986).

Ha, K. H., "CMAP, User's Manual.", Version 4.7 for IBM-PC and Compatibles, Concordia University (June 1993).

Hirst, M. J. S., and Dilger, W. H., "Prediction of Bridge Temperatures.", IABSE Periodica, No. P-138/89, pp. 109-120 (1989).

Hulsey, J. L., "Environmental Effects on Composite Girder Bridge Structures.", Ph. D. Thesis, Department of Civil Engineering, University of Missouri-Rolla, Rolla, Missouri (1976).

Hunt, B., and Cooke, N., "Thermal Calculations for Bridge Design.", Journal of Structural Engineering, Proceedings of the ASCE, Vol. 101, No. ST9, pp. 1763-1781 (1975).

Ibrahim, A. M. M., Elbadry, M. M., and El-Ariss, B., "User's Maunal and Computer Program FETAB3D: Three-Dimensional Finite Element Thermal Analysis of Bridges.", Research Report, Department of Civil Engineering, Concordia University, Sept. 1995 (in preperation).

Imbsen, R. A., Vandershaf, D. E., Schamber, R. A., and Nutt, R. V., "Thermal Effects in Concrete Bridge Superstructures.", National Cooperative Highway Research Program, Report 276, National Research Council, Washington (1985).

Incropera, F. P., and DeWitt, D. P., "Fundamentals of Heat Transfer.", John Wiley &Sons, New York (1981).

Iqbal, M., "Introduction to Solar Radiation.", Academic Press, Toronto (1983).

Kehlbeck, F., "Einfluss der Sonnenstrahlung bei Brückenbauwrken.", Technishe Unversität Hannover, Werner - Verlag, Düsseldorf (1975).

Kreith, F., and Kreider, J.F., "Principles of Solar Engineering.", 3rd Edition, McGraw-Hill, New York (1978).

Lanigan, A. G., "The Temperature Response of Concrete Box-Girder Bridges.", Ph.D. Thesis, Report No. 94, School of Engineering, University of Auckland, Auckland, New Zealand (1973).

Leonhardt, F., "Crack Control in Concrete Structures", IABSE Surveys, No. S-4/77, International Association for Bridge and Structural Engineering, Zurich (1977).

Leonhardt, F., Kolbe, G., and Peter, J., "Temperaturunterschiede gefahrden Spannbetonbrucke." Beton-und Stahlbetonbau, Vol. 60, No. 7, Berlin (July 1965).

Liu, B. Y. H. and Jordan R. C., "The Interrelationship and Characteristic Distribution of Direct, Diffuse and Total Solar Radiation.", Solar Energy Journal, Vol. 4, No. 3 (1960).

Maes, M. A., "Effects of Environmental and Material Characteristics on the Behavior of Concrete Structures", M.Sc. Thesis, Department of Civil Engineering, The University of Calgary, Calgary, Alberta (1980).

Maher, D. R. H., "The effect of Differential Temperature on Continuous Prestresses Concrete Bridges." Civil Engineering Transaction, Institute of Engineers of Australia, Vol. CE12, Part 1, Paper 1795 (April 1970).

Massicotte, B., Picard, A., Gaumond, Y., and Ouellet, C., "Strengthening of a Long Span Prestressed Segmental Box Girder Bridge.", PCI Journal, Vol. 39, No. 3, pp. 52-65 (1994).

Mirambell, E., and Aguado, A., "Temperature and Stress Distribution in Concrete Box Girder Bridges", Proceedings of the ASCE, Vol. 116, No. 9 (1990).

Molesini, P., and Massicotte, B., "Étude du Comportement Thermique du Pont de Grand-Mère.", Rapport No. EPM/GCS-1993-10, Département de Génie Civil, Section Structures, École Polytechnique, Montréal , Canada (1993).

Mondkar, P. D., and Powell, G. H., "Large Capacity Equation Solver for Structural Analysis.", Computers & Structures, Vol. 4, pp. 699-728 (1974).

Narouka, M. Hirai, I., and Yamaguti, T., "Measurement of the Temperature of the Interior of the Reinforced Concrete Slab of the Shigita Bridge and Presumtion of Thermal Stress." Symposium of the Stress Measurements for Bridge and Structures, Japanese Society for the Promotion of Science, Proc., Tokyo, Japan (1955).

"NISA-II", a finite element program for Numerically Integrated elements for System Analysis. Engineering Mechanics Research Corporation, Troy, Michigan, USA (1991).

Priestley, M. J. N., "Design Thermal Gradients for Concrete Bridges." New Zealand Engineering, Vol. 31, Part 9 (July. 1976).

Priestley, M. J. N., "Temperature Gradients in Bridges-Some Design Consideration." New Zealand Engineering, Vol. 27, Part 7 (Sept. 1972).

Radolli, M., and Green, R., "Thermal Stresses in Concrete Bridge Superstructures under Summer Conditions." Transportation Research Record 547, Transportation Research Board (1975).

Reynolds, J., and Emanuel, J. H., "Thermal Stresses and Movements in Bridges.", Journal of the Structural Engineering, Proceedings of the ASCE, Vol. 100, No. ST1, pp. 63-78 (Jan. 1974).

Saetta, A., Scotta, R., and Vitaliani R., "Stress Analysis of Concrete Structures Subjected to Variable Thermal Loads.", Journal of Structural Engineering, Proceedings of the ASCE, Vol. 121, No. 3, pp. 446-457 (1995).

Segerlind, L. J., "Applied Finite Element Analysis.", 2nd. Edition, John Wiley & Sons, New York (1984).

Sherwood, B. I., and Ray, D. J., "Thermal Radiation from the Atmosphere.", Journal of Geophysical Research, Vol. 74, No. 23, pp. 5397-5403 (1969).

Ugural, A. C., and Fenster, S. K., "Advanced Strenght and Applied Elasticity, The SI Version.", 1st Edition, Elsevier, New York (1981).

Waldron, P., Ramezankhani, M., and Woodman, N., "Differential Temperature Effects in Concrete Box Girder Bridges.", Proceedings of the 3rd International Conference on Developments in Short and Medium Span Bridge Engineering '90, Toronto, Canada (1990).

Wilson, E. L., Bathe, K. J., and Doherty, W. P., "Direct Solution of Large Systems of Linear Equations.", Computers & Structures, Vol. 4, pp. 363-372 (1974).

Zichner, T., "Thermal Effects on Concrete Bridges.", C.E.B., Enlarged Meeting-Commission 2, Pavia, pp. 292-313 (1981).

Zienkiewicz, O. C., and Taylor, R. L., "The Finite Element Method.", Vol 1-2, McGraw Hill Book Co., Inc., New York, N.Y (1991).

Zuk, W., "Thermal Behavior of Composite Bridges-Insulated and Uninsulated." Highway Research Record (1965).